APPLICATION OF ITERATIVE TECHNIQUES FOR ELECTROMAGNETIC WAVE SCATTERING FROM DIELECTRIC RANDOM ROUGH SURFACES

A THESIS

SUBMITTED TO THE DEPARTMENT OF ELECTRICAL AND

ELECTRONICS ENGINEERING

AND THE INSTITUTE OF ENGINEERING AND SCIENCE

OF BILKENT UNIVERSITY

IN PARTIAL FULFILLMENT OF THE REQUIREMENTS

FOR THE DEGREE OF

MASTER OF SCIENCE

By

Kıvanç İnan

July, 2005

I certify that I have read this thesis and that in my opinion it is fully adequate, in scope and in quality, as a thesis for the degree of Master of Science.

Asst. Prof. Vakur B. Ertürk (Advisor)

I certify that I have read this thesis and that in my opinion it is fully adequate, in scope and in quality, as a thesis for the degree of Master of Science.

Prof. Dr. Ayhan Altıntaş

I certify that I have read this thesis and that in my opinion it is fully adequate, in scope and in quality, as a thesis for the degree of Master of Science.

Assoc. Prof. Sencer Koç

I certify that I have read this thesis and that in my opinion it is fully adequate, in scope and in quality, as a thesis for the degree of Master of Science.

Prof. Dr. Mustafa Kuzuoğlu

I certify that I have read this thesis and that in my opinion it is fully adequate, in scope and in quality, as a thesis for the degree of Master of Science.

Asst. Prof. Defne Aktaş

Approved for the Institute of Engineering and Science:

Prof. Dr. Mehmet B. Baray
Director of the Institute

ABSTRACT

APPLICATION OF ITERATIVE TECHNIQUES FOR ELECTROMAGNETIC WAVE SCATTERING FROM DIELECTRIC RANDOM ROUGH SURFACES

Kıvanç İnan
M.S. in Electrical and Electronics Engineering
Supervisor: Asst. Prof. Vakur B. Ertürk
July, 2005

Mobile radio planning requires accurate prediction of electromagnetic field strengths over large terrain profiles. However the conventional method of moments (MoM) becomes unsuitable for electrically large rough dielectric surfaces, because of the $O(N^3)$ computational cost due to the large number of surface unknowns N. Iterative Methods are beneficial methods for faster electromagnetic problem solutions. By using such methods, very accurate results can be achieved, causing a computational cost of $O(N^2)$. In this work, among the stationary iterative methods; Forward-Backward Method (FBM), and among the nonstationary iterative ones; Conjugate Gradient Squared (CGS), BiConjugate Gradient Stabilized (Bi-CGSTAB) and Quasi Minimal Residual (QMR) Methods are presented to investigate the electromagnetic wave scattering from dielectric random rough surfaces. These techniques are compared to each other over various kinds of surface models that reflect the real terrains to find out the best solution methodologies. Furthermore, efficiency of the methods are assessed by comparing the obtained scattering results, normalized radar cross sections (NRCS) of the surfaces considered, with the numerically exact ones computed by employing the MoM.

Keywords: Random Rough Surface Scattering, Method of Moments (MoM), Forward-Backward Method (FBM), Conjugate Gradient Squared Method (CGS), BiConjugate Gradient Stabilized Method (Bi-CGSTAB), Quasi Minimal Residual Method (QMR), Normalized Radar Cross Section (NRCS).

ÖZET

DİELEKTRİK RASGELE DALGALI YÜZEYLERDEN ELEKTROMANYETİK DALGA SAÇILMASINDA İTERATİF YÖNTEMLERİN UYGULAMALARI

Kıvanç İnan
Elektrik ve Elektronik Mühendisliği, Yüksek Lisans
Tez Yöneticisi: Asst. Prof. Vakur B. Ertürk
Temmuz, 2005

Mobil radyo planlaması geniş yüzey yapılarında elektromanyetik alan kuvvetinin doğru tahminini sağlamaktadır. Ancak klasik moment yöntemi, (MoM), yüzey bilinmeyenleri çok fazla olduğu zaman, çözümleme yükünün $O(N^3)$ olmasından dolayı çok dalgalı ve elektriksel olarak geniş yüzeylerde uygun olmamaktadır. İteratif yaklaşımlar, elektromanyetik problemlerin daha hızlı çözümlemeleri hususunda oldukça etkilidir. Bu yöntemler kullanılarak, çözüm yükü $O(N^2)$ olan çok doğru sonuçlar elde edilebilir. Bu tezde, sabit iteratif yöntemlerden İleri-Geri Metodu ve sabit olmayan iteratif yöntemlerden Kısmen Minimum Kalan, Bi-Eşlenik Gradyan Stabil ve Eşlenik Gradyan Kareli yöntemlerinin dielektrik rasgele dalgalı yüzeylerdeki elektromanyetik dalga saçılmaları uygulamalarına yer verilmiştir. Ayrıca bu çözümleme teknikleri, en iyi çözümleme metodolojilerini ifade etmek için gerçek yüzeyleri yansıtan birçok profil için karşılaştırılmıştır. Bunlarla birlikte bu tezde kullanılan iteratif yöntemlerin başarısı ve doğruluğu, yöntemler vasıtasıyla elde edilen normalize edilmiş radar kesit alanlarının, numerik olarak kesin sonuç olan MoM'un uygulanmasıyla bulunan normalize edilmiş radar kesit alanlarıyla karşılaştırılarak değerlendirilmiştir.

Anahtar sözcükler: Rasgele Dalgalı Yüzey Saçılması, Moment Yöntemi, İleri-Geri Yöntemi, Kısmen Minimum Kalan Yöntemi, Bi-Eşlenik Gradyan Stabil Yöntemi, Eşlenik Gradyan Kareli Yöntemi, Normalize Edilmiş Radar Kesit Alanı.

Acknowledgement

I would like to express my sincere gratitude to Dr. Vakur B. Ertürk for his supervision, guidance, suggestions, instruction and encouragement through the development of this thesis.

I would like to thank to Dr. Ayhan Altıntaş, Dr. Sencer Koç, Dr. Mustafa Kuzuoğlu and Dr. Defne Aktaş for reading the manuscript and commenting on the thesis.

I would like to thank to Dr. Antonio Iodice for his suggestions and guidance who has answered with patience all of my questions about his published articles.

Finally, I would like to express my appreciation to my parents, and my brother for their endless love and continuous support throughout my life.

Contents

List of Figures

List of Tables

To My Family ...

Chapter 1

Introduction

Electromagnetic wave scattering is an active, interdisciplinary area of research with a plenty of theoretical and practical applications in fields ranging from atomic physics to medical imaging to geoscience, optics, acoustics, radiowave propagation and remote sensing. In particular, the issue of wave scattering from random discrete scatterers and rough surfaces presents both theoretical and numerical challenges due to the large degrees of freedom in these systems and the need to include multiple scattering effects precisely. In the past three decades, considerable theoretical improvement has been made in enlightening and understanding the scattering process involved in such problems. Diagrammatic techniques and effective medium theories persist essential for analytical studies; however, rapid development in computer technology has opened new doors for researchers with the full power of Monte Carlo simulations in the numerical analysis of rough and random media scattering. Numerical simulations allow to solve the Maxwell's equations accurately without the limitations of analytical approximations, whose regimes of validity are often difficult to assess.

Both analytical [1]-[2] and numerical methods [3]-[5] have been devised for the analysis of the problem. Approximate analytical methods attract the attention, since they allow an immediate comprehension of scattering dependence on surface geometric and electromagnetic properties. However, they are not valid for a large range and do not include some important and interesting classes of rough surface

cases. For instance, grazing angle incidence cannot be easily handled by using analytical methods because they cannot properly account for multiple scattering and shadowing, which are very fundamental concepts for grazing angle case. Accordingly, in recent years many studies have focused on numerical methods, and in particular on the method of moments (MoM) [3]-[25] and furthermore the iterative methods [6]-[25] in order to reduce the high-computational cost of the direct numerical computation via the MoM.

1.1 Literature Survey

Axline and Fung [3] simulated the wave scattering from a perfectly conducting random surface by calculating the surface current density induced by an impinging plane wave using the MoM. The scattering coefficient was obtained by averaging scattered fields from samples of computer generated random surfaces. In a later paper by Fung and Chen [4], the method of generating random profiles with specified correlation functions was developed, giving the simulation technique an additional control over the statistical properties of the rough surface target. In the paper by Chen and Bai [5], the detailed MoM simulation of wave scattering from a computer generated-dielectric rough surface in two-dimensional space was given.

The direct solution procedure for the MoM matrix equation such as LU decomposition has $O(N^3)$ computational cost. Therefore, the usage of iterative schemes have been considered, which solve for the surface current (or near fields) in $O(N^2)$ steps. Holliday et al. in [6], and Kapp and Brown in [7] used the forward-backward method (FBM), a stationary iterative method, for the cases of perfectly electrically conducting (PEC) surfaces that are single valued and rough in one dimension. Then, Tran [8] applied the same method with its brand new name, the method of ordered multiple interactions (MOMI), to scattering from a two-dimensional perfectly conducting rough surface problem and derived that the convergence rate of the iterative procedure strongly depends on the order in which the current elements are updated. This method converges impressively

fast but shows some irregularities for some cases, like very rough surfaces, low grazing angles, circular cylindrical scatterers etc. On the other hand, nonstationary algorithms were imposed into scattering from PEC rough surface problems, by Smith et al. [9] who used the biconjugate gradient (BiCG) method, Donohue et al. [10] who used a preconditioned multigrid generalized conjugate residual (GCR) approach and Chen [11], who used the conjugate gradient type methods. Although nonstationary techniques are slower in terms of convergence, they are more robust in many ill-conditioned situations. West and Sturm in [12] examined the performance of both stationary (i.e., Jacobi and MOMI) and nonstationary iterative techniques (i.e., biconjugate gradient stabilized (Bi-CGSTAB), quasi minimal residual (QMR), general minimal residual (GMRES) and conjugate gradient-normal equation (CGNR) methods) under various conditions and investigated their convergence capabilities for rough PEC surface problems. In [13], the generalized forward-backward method (GFBM) has been proposed for re-entrant rough PEC surface problems such as a ship in a sea or a large breaking wave. This new method uses a hybrid combination of the conventional FBM method and the MoM. Afterwards, Chou and Johnson [14] spectrally accelerated the FBM (FB/NSA) resulting in an $O(N)$ computational cost. This new method became capable of solving electromagnetic scattering from electrically large, rough PEC and impedance surfaces. In [15], (FB/NSA) was used for calculation of backscattering from rough PEC surfaces.

Recently, the case of scattering from dielectric random rough surfaces has been of great interest. In the paper of Benali et al. [16], the scattering of plane waves from a dielectric medium bounded by a one-dimensional rough surface was formulated. In [17], an efficient numerical solution for the scattering problem of inhomogeneous dielectric rough surfaces was presented. In [18], using the MoM, the physics-based two-grid method (PBTG) was combined with the banded-matrix iterative approach/canonical grid method to solve rough surface scattering problem for near grazing incidences and for high dielectric permittivities. Then West, in [19], examined the integral equation formulations for scattering from lossy interfaces for their suitability to various iterative solution

methods. The analysis was limited to interfaces that are uniform in one dimension and of high enough conductivity so that impedance boundary conditions are accurate. After that, Iodice, Franceschetti and Riccio [23] focused on the problem of scattering of electromagnetic waves from rough dielectric surfaces. They assumed the rough surface to be fractal and solved the problem with MoM. They gave the matrix formulations in a detailed way and compared the MoM results with the small perturbation method (SPM) results. Afterwards, Iodice in [24] solved a similar problem using the FBM and chose the surface to be a Gaussian or exponentially correlated random surface. He modified the method in a way to fit into this matrix equation, which has some irregularities as will be discussed in the following chapters. Furthermore, he compared the convergence rate of the proposed iterative scheme by using the obtained scattering results with the ones computed by MoM. Following [24], he presented the forward-backward approach in [25] for scattering from dielectric fractal surfaces in a similar way.

Nowadays, electromagnetic scattering from partially buried objects at the dielectric random rough surfaces attracts the attention ([26]), but the study of such cases are beyond the scope of this thesis.

1.2 Scope and Contributions of the Thesis

This thesis addresses the iterative solution of dielectric random rough surface scattering problem in several aspects. The convergence behavior of the iterative methods are compared to figure out their limitations for these situations.

First of all, the analogous integral equations for electromagnetic wave scattering from rough dielectric surfaces are derived. The equations are compared with the ones presented in [23]. Then, by using MoM and direct lower-upper (LU) decomposition, "numerically exact" solutions are derived for the Gaussian and exponentially correlated rough Gaussian dielectric surfaces. In order to assess the accuracy of the solutions, both bistatic and monostatic noncoherent radar cross section (NRCS) of the corresponding surfaces for various angles of incidence are

evaluated and compared with the ones that are given in [24].

After achieving very good agreement, similar problems are solved by using iterative techniques, Forward-Backward Method (FBM), which is a stationary iterative method and three nonstationary algorithms; namely, Quasi Minimal Residual (QMR), Conjugate Gradient Squared (CGS) and BiConjugate Gradient Stabilized (Bi-CGSTAB) methods. Their convergence performances are investigated over various profiles of roughness scales and dielectric permittivities, by comparing the obtained scattering results with the "numerically exact ones", computed by employing the conventional MoM.

For electromagnetic wave scattering from dielectric random rough surface problems, investigation of the efficiency of nonstationary algorithms in the solution process is addressed first in this thesis. Furthermore, the problem of electromagnetic scattering from re-entrant dielectric surfaces is included, which is another novel contribution.

1.3 Outline of the Thesis

This thesis is organized as follows. Chapter 2 introduces the fundamental concepts about dielectric rough surface scattering, and contains the random rough surface generation methodologies as well as other fundamental definitions that are going to be used. Chapter 3 describes the formulation and the solution of the problem along with the employment of the MoM. Chapter 4 includes the derivation and implementation of the iterative methods that are used to solve the formulated matrix equation. In Chapter 5, numerical results are given along with a discussion of their convergence rate. Finally, Chapter 6 contains conclusions and directions for future research. An e^{jwt} time convention is used and suppressed throughout this thesis. On the other hand, in matrix equations, such as $\underline{\underline{A}}\,\underline{x} = \underline{b}$, the vectors are denoted by $\underline{x}, \underline{b}$ and the matrix is denoted by $\underline{\underline{A}}$. However, in other cases (mainly in the formulation of the integral equations), vectors are typed bold, such as $\mathbf{E}, \mathbf{H}$.

Chapter 2

Background

2.1 Integral Equation Formulation For Dielectric Surfaces

The objective of the integral equation (IE) method for scattering is to derive the solution for the unknown current density, which is induced on the surface of the scatterer, in the form of an integral equation where the unknown induced current density is part of the integrand. Then by solving the integral equation using numerical techniques such as the method of moments (MoM), the current density on the surface and the scattered field can be determined [27].

2.1.1 General Equations for Electromagnetic Fields with Electric and Magnetic Sources and Boundary Conditions

In formulating integral equations for electromagnetic wave scattering, a convenient method is the use of equivalent electric and magnetic currents [28].

The Maxwell's and the continuity equations with electric sources of current

density $\mathbf{J}$, volume charge density ρ_{ev}, and surface charge density ρ_{es} are written as follows [29]:

$$\nabla \times \mathbf{E} = -j\omega\mu\mathbf{H} \tag{2.1}$$

$$\nabla \times \mathbf{H} = j\omega\epsilon\mathbf{E} + \mathbf{J} \tag{2.2}$$

$$\nabla \cdot \epsilon\mathbf{E} = \rho_{ev} \tag{2.3}$$

$$\nabla \cdot \mu\mathbf{H} = 0 \tag{2.4}$$

$$\nabla \cdot \mathbf{J} + j\omega\rho_{ev} = 0 \tag{2.5}$$

$$\nabla_s \cdot \mathbf{J}_s + j\omega\rho_{es} = 0 \tag{2.6}$$

where $\nabla_s \cdot \mathbf{J}_s$ is the surface divergence of $\mathbf{J}_s$ with $\mathbf{J}_s$ being the surface current density.

Electric and magnetic fields can also be written in terms of vector potential $\mathbf{A}$ and scalar potential ϕ as

$$\mathbf{H} = \frac{1}{\mu}\nabla \times \mathbf{A} \tag{2.7}$$

$$\mathbf{E} = -j\omega\mathbf{A} - \nabla\phi \tag{2.8}$$

where $\mathbf{A}$ and ϕ satisfy the following wave equations:

$$\left(\nabla^2 + k^2\right)\mathbf{A} = -\mu\mathbf{J} \tag{2.9}$$

$$\left(\nabla^2 + k^2\right)\phi = -\frac{\rho_{ev}}{\epsilon}. \tag{2.10}$$

Making use of the free-space scalar Green's function given by

$$g(\mathbf{r}, \mathbf{r}') = \frac{e^{-jk|\mathbf{r}-\mathbf{r}'|}}{4\pi|\mathbf{r} - \mathbf{r}'|}, \tag{2.11}$$

the vector potential $\mathbf{A}$ and the scalar potential ϕ can be expressed in the form of an integral as

$$\mathbf{A}(\mathbf{r}) = \mu \int d\mathbf{r}' g(\mathbf{r}, \mathbf{r}')\mathbf{J}(\mathbf{r}') \tag{2.12}$$

$$\phi(\mathbf{r}) = \frac{1}{\epsilon}\int d\mathbf{r}' g(\mathbf{r}, \mathbf{r}')\rho_{ev}(\mathbf{r}'). \tag{2.13}$$

Then, the magnetic field can be found by using (2.7) and (2.12) as

$$\mathbf{H} = \nabla \times \int d\mathbf{r}' g(\mathbf{r}, \mathbf{r}')\mathbf{J}(\mathbf{r}') = \int d\mathbf{r}' \nabla g(\mathbf{r}, \mathbf{r}') \times \mathbf{J}(\mathbf{r}'), \tag{2.14}$$

where the vector identity

$$\nabla \times (\psi \mathbf{A}) = \nabla\psi \times \mathbf{A} + \psi \nabla \times \mathbf{A} \tag{2.15}$$

is used. Similarly, substituting (2.12) and (2.13) into (2.8), the electric field is given by

$$\mathbf{E}(\mathbf{r}) = -j\omega\mu \int d\mathbf{r}' g(\mathbf{r}, \mathbf{r}')\mathbf{J}(\mathbf{r}') - \nabla \frac{1}{\epsilon} \int d\mathbf{r}' g(\mathbf{r}, \mathbf{r}')\rho_{ev}(\mathbf{r}') \tag{2.16}$$

and making use of the equation of continuity (2.5), the final expression for the electric field is obtained as

$$\mathbf{E}(\mathbf{r}) = -j\omega\mu \left[\int d\mathbf{r}' g(\mathbf{r}, \mathbf{r}')\mathbf{J}(\mathbf{r}') + \frac{1}{k^2} \nabla \int d\mathbf{r}' g(\mathbf{r}, \mathbf{r}') \nabla' \cdot \mathbf{J}(\mathbf{r}') \right]. \tag{2.17}$$

Consequently, fields are expressed in terms of only the electric current density ($\mathbf{J}$).

A similar procedure is carried out for the case of equivalent magnetic sources such that for a magnetic current density $\mathbf{M}$, volume charge density ρ_{mv}, and surface charge density ρ_{ms}, the Maxwell's and the continuity equations are given by

$$\nabla \times \mathbf{E} = -j\omega\mu\mathbf{H} - \mathbf{M} \tag{2.18}$$

$$\nabla \times \mathbf{H} = j\omega\epsilon\mathbf{E} \tag{2.19}$$

$$\nabla \cdot \epsilon\mathbf{E} = 0 \tag{2.20}$$

$$\nabla \cdot \mu\mathbf{H} = \rho_{mv} \tag{2.21}$$

$$\nabla \cdot \mathbf{M} + j\omega\rho_{mv} = 0 \tag{2.22}$$

$$\nabla_s \cdot \mathbf{M}_s + j\omega\rho_{ms} = 0. \tag{2.23}$$

The electric and magnetic fields can be expressed in terms of another vector potential $\mathbf{F}$ and another scalar potential ψ as

$$\mathbf{E} = -\frac{1}{\epsilon} \nabla \times \mathbf{F} \tag{2.24}$$

$$\mathbf{H} = -j\omega\mathbf{F} - \nabla\psi \tag{2.25}$$

where $\mathbf{F}$ and ψ satisfy the following wave equations:

$$\left(\nabla^2 + k^2\right)\mathbf{F} = -\epsilon\mathbf{M} \tag{2.26}$$

$$\left(\nabla^2 + k^2\right)\psi = -\frac{\rho_{mv}}{\mu}. \tag{2.27}$$

Using the free-space scalar Green's function given in (2.11) we have

$$\mathbf{F}(\mathbf{r}) = \epsilon \int d\mathbf{r}' g(\mathbf{r},\mathbf{r}')\mathbf{M}(\mathbf{r}') \tag{2.28}$$

$$\psi(\mathbf{r}) = \frac{1}{\mu}\int d\mathbf{r}' g(\mathbf{r},\mathbf{r}')\rho_{mv}(\mathbf{r}'). \tag{2.29}$$

Substituting (2.28) into (2.24) and making use of (2.15), the electric field is obtained as

$$\mathbf{E} = -\nabla \times \int d\mathbf{r}' g(\mathbf{r},\mathbf{r}')\mathbf{M}(\mathbf{r}') = -\int d\mathbf{r}' \nabla g(\mathbf{r},\mathbf{r}') \times \mathbf{M}(\mathbf{r}'), \tag{2.30}$$

and by substituting (2.28) and (2.29) into (2.25) and making use of (2.22), the magnetic field is given by

$$\mathbf{H}(\mathbf{r}) = -j\omega\epsilon\left[\int d\mathbf{r}' g(\mathbf{r},\mathbf{r}')\mathbf{M}(\mathbf{r}') + \frac{1}{k^2}\nabla \int d\mathbf{r}' g(\mathbf{r},\mathbf{r}')\nabla' \cdot \mathbf{M}(\mathbf{r}')\right]. \tag{2.31}$$

Consequently, similar to equivalent electric sources case, the fields are expressed in terms of only the magnetic current density ($\mathbf{M}$).

Finally, when both electric and magnetic sources are present, (2.14), (2.16) and (2.30), (2.31) are combined to give

$$\begin{aligned}\mathbf{E}(\mathbf{r}) = & -\int d\mathbf{r}' \nabla g(\mathbf{r},\mathbf{r}') \times \mathbf{M}(\mathbf{r}') \\ & -j\omega\mu\left[\int d\mathbf{r}' g(\mathbf{r},\mathbf{r}')\mathbf{J}(\mathbf{r}') + \frac{1}{k^2}\nabla \int d\mathbf{r}' g(\mathbf{r},\mathbf{r}')\nabla' \cdot \mathbf{J}(\mathbf{r}')\right]\end{aligned} \tag{2.32}$$

$$\begin{aligned}\mathbf{H}(\mathbf{r}) = & \int d\mathbf{r}' \nabla g(\mathbf{r},\mathbf{r}') \times \mathbf{J}(\mathbf{r}') \\ & -j\omega\epsilon\left[\int d\mathbf{r}' g(\mathbf{r},\mathbf{r}')\mathbf{M}(\mathbf{r}') + \frac{1}{k^2}\nabla \int d\mathbf{r}' g(\mathbf{r},\mathbf{r}')\nabla' \cdot \mathbf{M}(\mathbf{r}')\right].\end{aligned} \tag{2.33}$$

On the other hand, the boundary conditions separating two media of μ_1, ϵ_1 and μ_2, ϵ_2 (refer to Figure 2.1) where also surface electric and magnetic sources exist are as follows:

$$\hat{n} \times \mathbf{E}_1 - \hat{n} \times \mathbf{E}_2 = -\mathbf{M}_s \tag{2.34}$$

$$\hat{n} \times \mathbf{H}_1 - \hat{n} \times \mathbf{H}_2 = \mathbf{J}_s \tag{2.35}$$

$$\hat{n} \cdot \epsilon_1\mathbf{E}_1 - \hat{n} \cdot \epsilon_2\mathbf{E}_2 = \rho_{es} \tag{2.36}$$

$$\hat{n} \cdot \mu_1\mathbf{H}_1 - \hat{n} \cdot \mu_2\mathbf{H}_2 = \rho_{ms}. \tag{2.37}$$

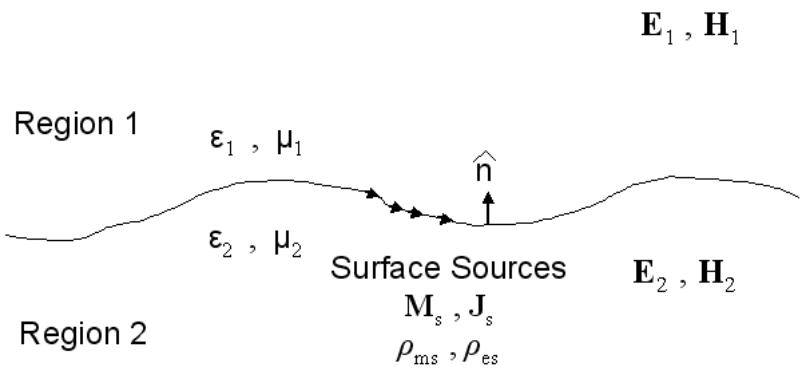

Figure 2.1: Two media with μ_1, ϵ_1 and μ_2, ϵ_2 where both electric and magnetic current sources exist.

2.1.2 Physical Problem

Consider an arbitrarily polarized incident wave (with electric field $\mathbf{E}^{inc}$ and magnetic field $\mathbf{H}^{inc}$) which illuminates a dielectric surface as depicted in Figure 2.2. Let ϵ_1, μ_1 be the permittivity and permeability of region 1 (which is above the interface), respectively, and ϵ_2, μ_2 be the permittivity and permeability of region 2 (which is below the interface), respectively. The unit normal $\hat{n}$ is defined pointing toward region 1 as shown in Figure 2.2. In region 1, the electromagnetic fields are given by

$$\mathbf{E}_1 = \mathbf{E}^{inc} + \mathbf{E}^s \tag{2.38}$$

$$\mathbf{H}_1 = \mathbf{H}^{inc} + \mathbf{H}^s \tag{2.39}$$

where $\mathbf{E}^s$ and $\mathbf{H}^s$ are the scattered electric and magnetic fields, respectively. On the other hand, in region 2, the electromagnetic fields are $\mathbf{E}_2$ and $\mathbf{H}_2$. Finally, for this situation, the boundary conditions are modified to be

$$\hat{n} \times \mathbf{E}_1 - \hat{n} \times \mathbf{E}_2 = 0 \tag{2.40}$$

$$\hat{n} \times \mathbf{H}_1 - \hat{n} \times \mathbf{H}_2 = 0 \tag{2.41}$$

$$\hat{n} \cdot \epsilon_1 \mathbf{E}_1 - \hat{n} \cdot \epsilon_2 \mathbf{E}_2 = 0 \tag{2.42}$$

$$\hat{n} \cdot \mu_1 \mathbf{H}_1 - \hat{n} \cdot \mu_2 \mathbf{H}_2 = 0, \tag{2.43}$$

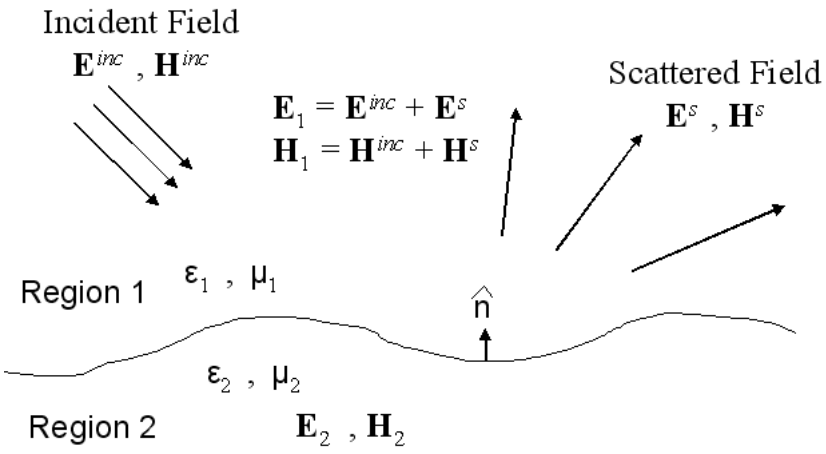

Figure 2.2: Physical problem describing the scattering from rough dielectric surface

since there is neither surface currents nor surface charges at the interface between the regions 1 and 2.

Two equivalent problems, one for region 1 and another for region 2 can be derived and then combined to obtain the resultant integral equations to be used in determining the surface **E** and **H** fields.

2.1.3 Equivalent Problem for Region 1

For Region 1 (let's consider as equivalent problem A), assume the same incident field $\mathbf{E}^{inc}$ and magnetic field $\mathbf{H}^{inc}$ and the same electric field $\mathbf{E}_1$ and magnetic field $\mathbf{H}_1$ in region 1 as in the physical problem. In this equivalent problem A, let there be equivalent sources on the boundary as seen in Figure 2.3, which satisfy

$$-\mathbf{M}_s^A = \hat{n} \times \mathbf{E}_1 \quad (2.44)$$

$$\mathbf{J}_s^A = \hat{n} \times \mathbf{H}_1 \quad (2.45)$$

$$\rho_{es}^A = \hat{n} \cdot \epsilon_1 \mathbf{E}_1 \quad (2.46)$$

$$\rho_{ms}^A = \hat{n} \cdot \mu_1 \mathbf{H}_1. \quad (2.47)$$

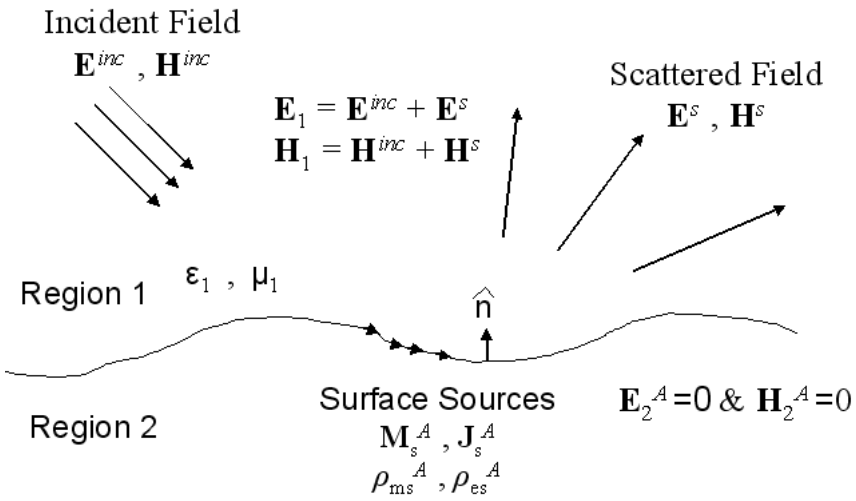

Figure 2.3: Equivalent problem A for scattering from dielectric rough surface

On the other hand, from the boundary conditions given by (2.34)-(2.37), we have

$$\hat{n} \times \mathbf{E}_1 - \hat{n} \times \mathbf{E}_2^A = \mathbf{M}_s^A \tag{2.48}$$

$$\hat{n} \times \mathbf{H}_1 - \hat{n} \times \mathbf{H}_2^A = \mathbf{J}_s^A \tag{2.49}$$

$$\hat{n} \cdot \epsilon_1 \mathbf{E}_1 - \hat{n} \cdot \epsilon_2 \mathbf{E}_2^A = \rho_{es}^A \tag{2.50}$$

$$\hat{n} \cdot \mu_1 \mathbf{H}_1 - \hat{n} \cdot \mu_2 \mathbf{H}_2^A = \rho_{ms}^A. \tag{2.51}$$

Using (2.44)-(2.47) in (2.48)-(2.51), we have $\mathbf{E}_2^A = 0$,and $\mathbf{H}_2^A = 0$ at the boundary. By Huygen's principle

$$\mathbf{E}_2^A = 0 \tag{2.52}$$

$$\mathbf{H}_2^A = 0 \tag{2.53}$$

everywhere in region 2 ([30], [31]). Whereas, in region 1 the scattered field generated by these equivalent sources can be derived by considering (2.32) and (2.33):

$$\begin{aligned} \mathbf{E}^s(\mathbf{r}) = & -j\omega\mu_1 \left[\int dS' g_1(\mathbf{r}, \mathbf{r}') \mathbf{J}_s^A(\mathbf{r}') + \frac{1}{k_1^2} \nabla \int dS' g_1(\mathbf{r}, \mathbf{r}') \nabla_s' \cdot \mathbf{J}_s^A(\mathbf{r}') \right] \\ & - \int dS' \nabla g_1(\mathbf{r}, \mathbf{r}') \times \mathbf{M}_s^A(\mathbf{r}') \end{aligned} \tag{2.54}$$

$$\mathbf{H}^s(\mathbf{r}) = -j\omega\epsilon_1\left[\int dS' g_1(\mathbf{r},\mathbf{r}')\mathbf{M}_s^A(\mathbf{r}') + \frac{1}{k_1^2}\nabla\int dS' g_1(\mathbf{r},\mathbf{r}')\nabla_s'\cdot\mathbf{M}_s^A(\mathbf{r}')\right] + \int dS'\nabla g_1(\mathbf{r},\mathbf{r}')\times\mathbf{J}_s^A(\mathbf{r}') \quad (2.55)$$

where

$$g_1(\mathbf{r},\mathbf{r}') = \frac{e^{-jk_1|\mathbf{r}-\mathbf{r}'|}}{4\pi|\mathbf{r}-\mathbf{r}'|}. \quad (2.56)$$

It should be mentioned at this point that the equivalent sources radiate to whole space. As these equivalent sources radiate into region 2, these fields will cancel the incident fields to yield $\mathbf{E}_2^A = 0$ and $\mathbf{H}_2^A = 0$ ((2.52) and (2.53)). Note that region 2 also has ϵ_1 and μ_1 as region 1. For $\mathbf{r}$ in region 2, we thus have the total electric field equation from the extinction theorem as $\mathbf{E}^{inc}+\mathbf{E}^s = 0$ yielding an expression for the incident electric field $\mathbf{E}^{inc}(\mathbf{r})$ as

$$\mathbf{E}^{inc}(\mathbf{r}) = j\omega\mu_1\left[\int dS' g_1(\mathbf{r},\mathbf{r}')\mathbf{J}_s^A(\mathbf{r}') + \frac{1}{k_1^2}\nabla\int dS' g_1(\mathbf{r},\mathbf{r}')\nabla_s'\cdot\mathbf{J}_s^A(\mathbf{r}')\right] + \int dS'\nabla g_1(\mathbf{r},\mathbf{r}')\times\mathbf{M}_s^A(\mathbf{r}'). \quad (2.57)$$

In a similar fashion, from $\mathbf{H}^{inc}+\mathbf{H}^s = 0$ an expression for the incident magnetic field $\mathbf{H}^{inc}(\mathbf{r})$ can be obtained as

$$\mathbf{H}^{inc}(\mathbf{r}) = j\omega\epsilon_1\left[\int dS' g_1(\mathbf{r},\mathbf{r}')\mathbf{M}_s^A(\mathbf{r}') + \frac{1}{k_1^2}\nabla\int dS' g_1(\mathbf{r},\mathbf{r}')\nabla_s'\cdot\mathbf{M}_s^A(\mathbf{r}')\right] - \int dS'\nabla g_1(\mathbf{r},\mathbf{r}')\times\mathbf{J}_s^A(\mathbf{r}'). \quad (2.58)$$

Details of the application of Huygen's Principle and extinction theorem on dielectric rough surface scattering problems can be found in [30] (Section 2.2) or in [31] (Chapter 6).

If we consider (2.57) and (2.58), (2.57) and (2.58) yield overall 6 scalar integral equations, in which the incident fields are known and the equivalent surface current currents are unknown. However, the surface fields (i.e. the equivalent surface currents) cannot be calculated by using them, since they are not independent. Surface fields (i.e. the equivalent surface currents) further depend on the second medium and its parameters, but μ_2, ϵ_2 and g_2 (Green's function for region 2) are not involved in the equations. Thus, we need to solve the equivalent problem for region 2 to conclude the solution to the problem.

2.1.4 Equivalent Problem for Region 2

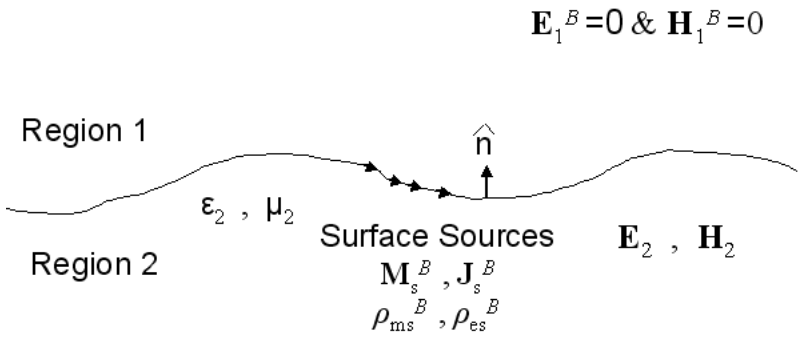

Figure 2.4: Equivalent problem B for region 2 for scattering from dielectric rough surface

Now, let's consider the equivalent problem B for region 2 with the same electric field $\mathbf{E}_2$ and magnetic field $\mathbf{H}_2$ in region 2 as in the physical problem. At the boundary we introduce equivalent sources (Figure 2.4), which satisfy

$$-\mathbf{M}_s^B = \hat{n}_i \times \mathbf{E}_2 \tag{2.59}$$

$$\mathbf{J}_s^B = \hat{n}_i \times \mathbf{H}_2 \tag{2.60}$$

$$\rho_{es}^B = \hat{n}_i \cdot \epsilon_2 \mathbf{E}_2 \tag{2.61}$$

$$\rho_{ms}^B = \hat{n}_i \cdot \mu_2 \mathbf{H}_2 \tag{2.62}$$

where $\hat{n}_i = -\hat{n}$. Then similar to the equivalent problem A case, via the help of boundary conditions given by (2.34)-(2.37), we obtain

$$\mathbf{E}_1^B = 0 \tag{2.63}$$

$$\mathbf{H}_1^B = 0 \tag{2.64}$$

everywhere in region 1. Whereas in region 2, the fields generated by these equivalent sources can be obtained by using (2.32) and (2.33) as

$$\begin{aligned}\mathbf{E}^B(\mathbf{r}) = & -j\omega\mu_2\left[\int dS' g_2(\mathbf{r},\mathbf{r}')\mathbf{J}_s^B(\mathbf{r}') + \frac{1}{k_2^2}\nabla\int dS' g_2(\mathbf{r},\mathbf{r}')\nabla_s'\cdot\mathbf{J}_s^B(\mathbf{r}')\right] \\ & - \int dS' \nabla g_2(\mathbf{r},\mathbf{r}')\times\mathbf{M}_s^B(\mathbf{r}')\end{aligned} \tag{2.65}$$

$$\mathbf{H}^B(\mathbf{r}) = -j\omega\epsilon_2\left[\int dS' g_2(\mathbf{r},\mathbf{r}')\mathbf{M}_s^B(\mathbf{r}') + \frac{1}{k_2^2}\nabla\int dS' g_2(\mathbf{r},\mathbf{r}')\nabla'_s\cdot\mathbf{M}_s^B(\mathbf{r}')\right] + \int dS'\nabla g_2(\mathbf{r},\mathbf{r}')\times\mathbf{J}_s^B(\mathbf{r}') \quad (2.66)$$

where

$$g_2(\mathbf{r},\mathbf{r}') = \frac{e^{-jk_2|\mathbf{r}-\mathbf{r}'|}}{4\pi|\mathbf{r}-\mathbf{r}'|}. \quad (2.67)$$

Similar to the equivalent problem A case, these equivalent sources radiate with the Green's function g_2 to whole space. As these equivalent sources radiate into region 1, these fields will yield $\mathbf{E}_1^B = 0$ and $\mathbf{H}_1^B = 0$ ((2.63) and (2.64)). Note that we also have ϵ_2 and μ_2 for region 1 as well. Thus, for $\mathbf{r}$ in region 1, we have the electric field equation which is obtained from $\mathbf{E}_1^B = 0$ as

$$-\ j\omega\mu_2\left[\int dS' g_2(\mathbf{r},\mathbf{r}')\mathbf{J}_s^B(\mathbf{r}') + \frac{1}{k_2^2}\nabla\int dS' g_2(\mathbf{r},\mathbf{r}')\nabla'_s\cdot\mathbf{J}_s^B(\mathbf{r}')\right] - \int dS'\nabla g_2(\mathbf{r},\mathbf{r}')\times\mathbf{M}_s^B(\mathbf{r}') = 0. \quad (2.68)$$

In a similar fashion from $\mathbf{H}_1^B = 0$, we obtain

$$-\ j\omega\epsilon_2\left[\int dS' g_2(\mathbf{r},\mathbf{r}')\mathbf{M}_s^B(\mathbf{r}') + \frac{1}{k_2^2}\nabla\int dS' g_2(\mathbf{r},\mathbf{r}')\nabla'_s\cdot\mathbf{M}_s^B(\mathbf{r}')\right] + \int dS'\nabla g_2(\mathbf{r},\mathbf{r}')\times\mathbf{J}_s^B(\mathbf{r}') = 0. \quad (2.69)$$

Since the right hand side of (2.68) and (2.69) are zero (they are not unknowns), then making use of (2.68) and (2.69) results in a total number of 6 scalar integral equations to be solved. However, the surface fields cannot be calculated by using these equations, since they are not independent. This is obvious, because μ_1, ϵ_1 and g_1 (Green's function for region 1) are not involved in these equations. Neither is the incident field involved in the above equations. Thus, we also need the equivalent problem for region 1.

Finally, because of the continuity of tangential $\mathbf{E}$ and $\mathbf{H}$, and the continuity of normal $\mathbf{D}$ and $\mathbf{B}$ for the physical problem, and $\hat{n}_i = -\hat{n}$, we have the following

relations for the equivalent sources A and B.

$$\mathbf{M}_s^A = -\mathbf{M}_s^B \tag{2.70}$$
$$\mathbf{J}_s^A = -\mathbf{J}_s^B \tag{2.71}$$
$$\rho_{es}^A = -\rho_{es}^B \tag{2.72}$$
$$\rho_{ms}^A = -\rho_{ms}^B. \tag{2.73}$$

2.1.5 Surface Integral Equations for Equivalent Surface Currents

Surface integral equations are obtained by considering both of the regions and letting both $\mathbf{r}$ and $\mathbf{r}'$ be on the interface of region 1 and region 2. Different surface integral equations can be obtained by taking various combinations of the equations for region 1 and region 2. In this thesis, we considered (2.57) and (2.58) for region 1 (electric field equation and magnetic field equation, respectively), and (2.68) and (2.69) for region 2 (electric field equation and magnetic field equation, respectively).

First let's start with the cross product of (2.57) and (2.58) with $\hat{n}$ at the interface. In that case, when $\mathbf{r} = \mathbf{r}'$ we will have a singularity to be handled. To remove that singularity, the surface S in (2.57) and (2.58) is divided into two regions, namely S_a and P. S_a is the area of a circular disk of small radius a about $\mathbf{r}$ and P is the rest of the surface $S - S_a$. Note that, since we are dealing with a two dimensional problem in this study, for simplicity, we consider a circular disk rather than a circular sphere. Then, the surface integrals are written as

$$\int_S dS' = \int_{S_a} dS' + \int_{S-S_a} dS' = \int_{S_a} dS' + \int_P dS' \tag{2.74}$$

where $\int_P dS'$ is known as the principle value (PV) integral. It should be first mentioned that the first and second integrals of (2.57) and (2.58) are less singular. Therefore, the contributions $\int_{S_a} dS'$ from them will vanish. However, the part $\int_{S_a} dS' \nabla g_1(\mathbf{r}, \mathbf{r}')$ in the third integrals of (2.57) and (2.58) contains a higher order singularity. Because of this, the following procedure is proceeded by regarding

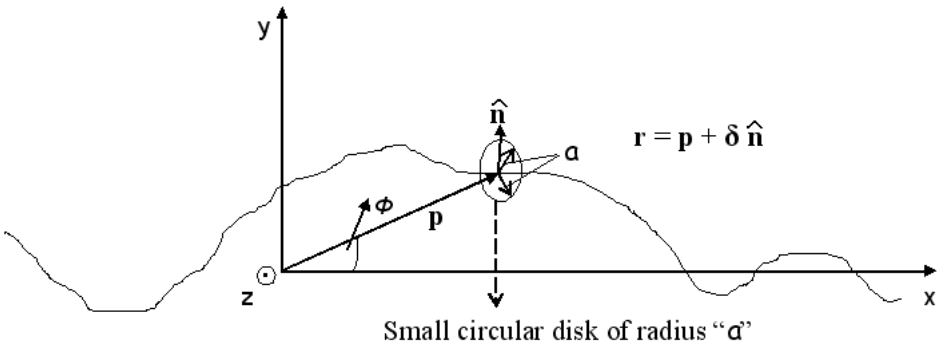

Figure 2.5: A small circular disk of radius a about $\mathbf{r}$.

to the Figure 2.5. Let $\mathbf{r} = \mathbf{p} + \delta\hat{n}$ where $\mathbf{p}$ is a point on the rough surface and δ is a small scalar quantity. Its sign is more important for us in the following derivations. If $\delta > 0$, then $\mathbf{r}$ is infinitesimally above the surface, if $\delta < 0$, then $\mathbf{r}$ is infinitesimally below the surface, where $\hat{n}$ is the normal to the surface at point $\mathbf{p}$. By letting (ρ',ϕ') be the polar coordinates of $\mathbf{r}'$ of circular disk of radius a centered about $\mathbf{p}$

$$\begin{aligned}
\int_{S_a} dS' \nabla g_1(\mathbf{r},\mathbf{r}') &= \int_0^a d\rho'\rho' \int_0^{2\pi} d\phi' \nabla \frac{1}{4\pi|\mathbf{r}-\mathbf{r}'|} \\
&= \int_0^a d\rho'\rho' \int_0^{2\pi} d\phi' \left[-\frac{(\mathbf{r}-\mathbf{r}')}{4\pi|\mathbf{r}-\mathbf{r}'|^3} \right] \\
&= \int_0^a d\rho'\rho' \int_0^{2\pi} d\phi' \left[-\frac{\hat{n}\delta - (\rho'\cos\phi'\hat{x} + \rho'\sin\phi'\hat{y})}{4\pi(\rho'^2+\delta^2)^{3/2}} \right]
\end{aligned}$$

The $\hat{x}$ and $\hat{y}$ components integrate to zero because of their $\sin\phi'$ and $\cos\phi'$ coefficients, respectively. Thus

$$\begin{aligned}
\int_{S_a} dS' \nabla g_1(\mathbf{r},\mathbf{r}') &= -\hat{n}\frac{\delta}{2} \int_0^a d\rho'\rho' \frac{1}{(\rho'^2+\delta^2)^{3/2}} \\
&= -\hat{n}\frac{1}{2}\left[-\frac{\delta}{(\rho'^2+\delta^2)^{1/2}} \right]_0^a = -\frac{\hat{n}}{2}\left[-\frac{\delta}{(a^2+\delta^2)^{1/2}} \pm 1 \right]
\end{aligned}$$

where the + sign is for $\delta > 0$ and − sign is for $\delta < 0$. Hence,

$$\int_{S_a} dS' \nabla g_1(\mathbf{r},\mathbf{r}') = \begin{cases} -\frac{\hat{n}}{2} & \text{for } \delta > 0 \\ \frac{\hat{n}}{2} & \text{for } \delta < 0. \end{cases} \tag{2.75}$$

Therefore, the third integrals of (2.57) and (2.58) become

$$\begin{aligned} \hat{n} \times & \int_{S_a} dS' \nabla g_1(\mathbf{r},\mathbf{r}') \times \mathbf{J}(\mathbf{r}') \\ &= \hat{n} \times \left(\frac{\hat{n}}{2} \times \mathbf{J}_s(\mathbf{r}) \right) = -\frac{\mathbf{J}_s}{2} = -\frac{\hat{n} \times \mathbf{H}}{2} \end{aligned} \tag{2.76}$$

$$\begin{aligned} \hat{n} \times & \int_{S_a} dS' \nabla g_1(\mathbf{r},\mathbf{r}') \times \mathbf{M}(\mathbf{r}') \\ &= \hat{n} \times \left(\frac{\hat{n}}{2} \times \mathbf{M}_s(\mathbf{r}) \right) = -\frac{\mathbf{M}_s}{2} = \frac{\hat{n} \times \mathbf{E}}{2}. \end{aligned} \tag{2.77}$$

After rearranging the terms, we get the governing surface electric field integral equation and the surface magnetic field integral equation, respectively, for region 1 as

$$\begin{aligned} \hat{n} \times \mathbf{E}^{inc}(\mathbf{r}) &= \hat{n} \times \int_P dS' \nabla g_1(\mathbf{r},\mathbf{r}') \times \mathbf{M}_s - \frac{\mathbf{M}_s}{2} \\ &\quad + \hat{n} \times \left[\int_P dS' j\omega\mu_1 g_1(\mathbf{r},\mathbf{r}') \mathbf{J}_s - \int_P dS' \nabla g_1(\mathbf{r},\mathbf{r}') \frac{[\nabla'_s \cdot \mathbf{J}_s(\mathbf{r}')]}{j\omega\epsilon_1} \right] \end{aligned} \tag{2.78}$$

$$\begin{aligned} \hat{n} \times \mathbf{H}^{inc}(\mathbf{r}) &= -\hat{n} \times \int_P dS' \nabla g_1(\mathbf{r},\mathbf{r}') \times \mathbf{J}_s(\mathbf{r}') + \frac{\mathbf{J}_s}{2} \\ &\quad + \hat{n} \times \left[\int_P dS' j\omega\epsilon_1 g_1(\mathbf{r},\mathbf{r}') \mathbf{M}_s - \int_P dS' \nabla g_1(\mathbf{r},\mathbf{r}') \frac{[\nabla'_s \cdot \mathbf{M}_s(\mathbf{r}')]}{j\omega\mu_1} \right]. \end{aligned} \tag{2.79}$$

Following the same procedure for (2.68) and (2.69), the surface magnetic and electric field integral equations, respectively, for region 2 are found as

$$\begin{aligned} 0 &= -\hat{n} \times \int_P dS' \nabla g_2(\mathbf{r},\mathbf{r}') \times \mathbf{M}_s - \frac{\mathbf{M}_s}{2} \\ &\quad - \hat{n} \times \left[\int_P dS' j\omega\mu_2 g_2(\mathbf{r},\mathbf{r}') \mathbf{J}_s - \int_P dS' \nabla g_2(\mathbf{r},\mathbf{r}') \frac{[\nabla'_s \cdot \mathbf{J}_s(\mathbf{r}')]}{j\omega\epsilon_2} \right] \end{aligned} \tag{2.80}$$

$$\begin{aligned} 0 &= \hat{n} \times \int_P dS' \nabla g_2(\mathbf{r},\mathbf{r}') \times \mathbf{J}_s(\mathbf{r}') + \frac{\mathbf{J}_s}{2} \\ &\quad - \hat{n} \times \left[\int_P dS' j\omega\epsilon_2 g_2(\mathbf{r},\mathbf{r}') \mathbf{M}_s - \int_P dS' \nabla g_2(\mathbf{r},\mathbf{r}') \frac{[\nabla'_s \cdot \mathbf{M}_s(\mathbf{r}')]}{j\omega\mu_2} \right]. \end{aligned} \tag{2.81}$$

Equations (2.78)-(2.81) are the basic integral equations for the electromagnetic scattering problems from dielectric surfaces. Details of the solution for those equations are discussed at Chapter 3.

2.2 Random Rough Surface Generation

In this section, random rough surface generation methodology that is used in this thesis is discussed [29]. Gaussian rough surfaces with Gaussian and Exponential correlation functions are generated.

A one-dimensional random rough surface can be represented by $z = f(x)$, where $f(x)$ is a real valued random rough height function (later we call it as a process) of x with zero mean

$$\int_0^L xf(x)dx = \langle f(x) \rangle = 0, \tag{2.82}$$

where L is the length of the random rough profile.

The Fourier transform of the rough surface height function, $f(x)$, is

$$F(k_x) = \frac{1}{2\pi} \int_{-\infty}^{\infty} dx e^{-jk_x x} f(x). \tag{2.83}$$

Then similar to the space domain, in the spectral domain we have

$$\langle F(k_x) \rangle = 0. \tag{2.84}$$

The process $f(x)$ is called Gaussian if the random variables $f(x_1), f(x_2), \cdots, f(x_n)$ are jointly Gaussian for any $n, x_1, x_2, \cdots, x_n$ [32]. The Gaussian process is completely characterized by its correlation function $\langle f(x_1)f(x_2) \rangle = h^2 C(x_1, x_2)$, where h is the root mean square (rms) height.

A rough surface is modelled by a stationary random process, since it is desired to have the surface roughness to be shift invariant, i.e., it should have uniformity. For a stationary random process we have

$$\langle f(x_1)f(x_2) \rangle = h^2 C(x_1 - x_2). \tag{2.85}$$

The Fourier transform of (2.85) is given by

$$h^2C(x_1 - x_2) = \int_{-\infty}^{\infty} dk_{1x} \int_{-\infty}^{\infty} dk_{2x} e^{jk_{1x}x_1 - jk_{2x}x_2} \langle F(k_{1x})F^*(k_{2x})\rangle. \tag{2.86}$$

Since the left hand side of (2.86) depends only on $x_1 - x_2$ and $f(x)$ is real (i.e., $F^*(k_x) = F(-k_x)$) then

$$\langle F(k_{1x})F^*(k_{2x})\rangle = \langle F(k_{1x})F(-k_{2x})\rangle = \delta(k_{1x} - k_{2x})W(k_{1x}) \tag{2.87}$$

where $W(k_x)$ is known as the spectral density. The Fourier transform of $h^2C(x)$ is the spectral density $W(k_x)$ given by [32]

$$h^2C(x) = \int_{-\infty}^{\infty} dk_x e^{jk_x x} W(k_x). \tag{2.88}$$

The right hand side of (2.87) is nonzero only if $k_{1x} = k_{2x}$, so $F(k_{1x})$ and $F^*(k_{2x})$ are independent random variables, then (2.87) equals to zero,

$$\langle F(k_{1x})F^*(k_{2x})\rangle = \langle F(k_{1x})\rangle\langle F^*(k_{2x})\rangle = 0. \tag{2.89}$$

Now, let's consider that $f(x)$ is a periodic function with periodicity of L, i.e., $f(x) = f(x + L)$. We can represent $f(x)$ via its Fourier series as

$$f(x) = \frac{1}{L} \sum_{n=-\infty}^{\infty} b_n e^{\frac{j2\pi nx}{L}} \tag{2.90}$$

where b_n is Gaussian distributed which will be shown shortly. From (2.85) and (2.90) we have

$$\langle f(x_1)f(x_2)\rangle = \frac{1}{L^2} \sum_{n=-\infty}^{\infty} \sum_{m=-\infty}^{\infty} \langle b_n b_m^*\rangle e^{\frac{j2\pi nx_1}{L}} e^{-\frac{j2\pi mx_2}{L}}. \tag{2.91}$$

By using (2.85) and (2.87) in (2.86)

$$\langle f(x_1)f(x_2)\rangle = h^2C(x_1 - x_2) = \int_{-\infty}^{\infty} dk_x e^{jk_x(x_1 - x_2)} W(k_x), \tag{2.92}$$

and by equating (2.91) to (2.92)

$$\int_{-\infty}^{\infty} dk_x e^{jk_x(x_1 - x_2)} W(k_x) = \frac{1}{L^2} \sum_{n=-\infty}^{\infty} \sum_{m=-\infty}^{\infty} \langle b_n b_m^*\rangle \exp\left(\frac{j2\pi n}{L}(x_1 - x_2)\right), \tag{2.93}$$

(2.93) can be written as

$$\frac{2\pi}{L}\sum_{n=-\infty}^{\infty} e^{jK_n(x_1-x_2)}W(K_n) = \frac{1}{L^2}\sum_{n=-\infty}^{\infty}\sum_{m=-\infty}^{\infty}\langle b_n b_m^*\rangle e^{jK_n(x_1-x_2)} \tag{2.94}$$

where

$$K_n = \frac{2\pi n}{L} = n\Delta k_x. \tag{2.95}$$

From (2.94),

$$\langle b_n b_m^*\rangle = 2\pi L W(K_n). \tag{2.96}$$

Since b_n and b_m are independent, $\langle b_n b_m^*\rangle$ is zero unless $m = n$. Thus,

$$\langle |b_n|^2\rangle = 2\pi L W(K_n). \tag{2.97}$$

When $f(x)$ is real, Fourier series coefficients satisfy,

$$b_n = b_{-n}^*. \tag{2.98}$$

Then from (2.96), we know that

$$\langle b_n b_{-n}^*\rangle = 0. \tag{2.99}$$

Combining (2.98) and (2.99) results in

$$\langle b_n b_n\rangle = 0. \tag{2.100}$$

If we represent real and imaginary parts of b_n as $\Re(b_n)$ and $\Im(b_n)$, respectively,

$$b_n = \Re(b_n) + j\Im(b_n), \tag{2.101}$$

(2.100) results in

$$\langle(\Re(b_n))^2\rangle = \langle(\Im(b_n))^2\rangle \tag{2.102}$$

$$\langle\Re(b_n)\rangle\langle\Im(b_n)\rangle = 0. \tag{2.103}$$

Thus $\Re(b_n)$ and $\Im(b_n)$ are independent Gaussian random variables, $\mathcal{N}(0, \frac{\langle|b_n|^2\rangle}{2})$ (with mean zero and variance equal to half of that of $\langle|b_n|^2\rangle$), so b_n turns out to be circularly symmetric complex Gaussian random variable. Then, a random rough

Gaussian surface can be represented by a Fourier series with Gaussian distributed coefficients satisfying (2.98)-(2.102).

In order to generate N independent Gaussian random numbers, which are Fourier series coefficients for Gaussian surface formulation, we divide the surface L into N units and we use a DFT (discrete Fourier transform) version of (2.90). Let there be N points in both space and spectral domains, then the unit distance will be

$$\Delta x = \frac{L}{N} \tag{2.104}$$

and

$$x_m = m\Delta x \tag{2.105}$$

for

$$m = -\frac{N}{2}+1, \cdots, 0, 1, \cdots, \frac{N}{2} \tag{2.106}$$

$$f(x_m) \equiv f_m. \tag{2.107}$$

Then

$$f_m = \frac{1}{L} \sum_{n=-\frac{N}{2}+1}^{\frac{N}{2}} b_n \exp\left(j\frac{2\pi nm}{N}\right). \tag{2.108}$$

The DFT is

$$b_n = \frac{L}{N} \sum_{m=-\frac{N}{2}+1}^{\frac{N}{2}} f_m e^{-j\frac{2\pi nm}{N}}. \tag{2.109}$$

Equations (2.108) and (2.109) can readily be computed by FFT. Both f_m and b_n are periodic with period N. That is,

$$b_{n+N} = b_n \tag{2.110}$$

$$f_{m+N} = f_m. \tag{2.111}$$

Hence,

$$b_{-\frac{N}{2}} = b_{\frac{N}{2}}. \tag{2.112}$$

Moreover from (2.98) we know that

$$b_{-\frac{N}{2}} = b_{\frac{N}{2}} = b^*_{-\frac{N}{2}}. \tag{2.113}$$

Then (2.112) and (2.113) yield both $b_{+\frac{N}{2}}$ and b_0 are real.

We have shown that any periodic discrete function has special DFT coefficients satisfying (2.110)-(2.113). Using MATLAB, we can generate independent Gaussian random numbers satisfying these special conditions, thus a random Gaussian surface using inverse DFT. Below is the MATLAB methodology given in step by step format:

1. With a given seed, N Gaussian distributed random numbers that have zero mean and unit variance are generated using MATLAB function `randn`. These N numbers are independent and they are not required to be grouped or arranged in any order. Let the numbers be labeled as $r_1, r_2, \cdots, r_N$.

2. Then two real Gaussian numbers $b_{+\frac{N}{2}}$ and b_0 are calculated as

$$b_0 = \sqrt{2\pi LW(0)}r_\alpha \tag{2.114}$$

$$b_{+\frac{N}{2}} = \sqrt{2\pi LW(\frac{\pi N}{L})}r_\beta \tag{2.115}$$

   where $\alpha \neq \beta$ and $\alpha, \beta \in \big\{1, 2, \cdots, N\big\}$.

3. $(N/2-1)$ Gaussian numbers are calculated by using

$$b_n = \sqrt{2\pi LW(|K_N|)}\left[\frac{1}{\sqrt{2}}(r_\sigma + jr\xi)\right] \tag{2.116}$$

   for $n = -\frac{N}{2}+1, \cdots, -2, -1$ where σ, ξ are distinct indices selected from set $S = \Big\{\big\{1, 2, \cdots, N\big\}/\big\{\alpha, \beta\big\}\Big\}$.

4. Using (2.98),

$$b_n = b^*_{-n} \tag{2.117}$$

   b_n for $n = 1, 2, \cdots, \frac{N}{2}-1$ can be calculated in a straightforward way.

5. Finally, using the inverse DFT relation in (2.118) with $X(n) = b_n$,

$$x(m) = \frac{1}{N}\sum_{n=-\frac{N}{2}+1}^{\frac{N}{2}} X(n)e^{\frac{2\pi j}{N}mn} \tag{2.118}$$

$x(m), m \in \{1, 2, \cdots, N-1\}$ is obtained. Extending $x(m)$ periodically, rough surface height profile is figured out as

$$f_m = \frac{N}{L} x(m) \tag{2.119}$$

for $m = -\frac{N}{2} + 1, \cdots, \frac{N}{2}$.

Our method in this study is to evaluate the derivative and higher order derivatives of the rough surface profile by means of finite difference

$$f'(x_m) = \frac{f(x_m + 1) - f(x_m - 1)}{2\Delta x}. \tag{2.120}$$

For the two endpoints $m = -\frac{N}{2} + 1$ and $m = \frac{N}{2}$, we use the periodic condition of DFT to get $f(x_m)$ for $m = -\frac{N}{2}$ and $m = \frac{N}{2} + 1$.

2.2.1 Gaussian Spectrum

For the case that the correlation function is Gaussian

$$C(x) = \exp\left(-\frac{x^2}{l^2}\right). \tag{2.121}$$

Using (2.88), the Gaussian Spectral Density can be shown to be

$$W(k_x) = \frac{h^2 l}{2\sqrt{\pi}} \exp\left(-\frac{k_x^2 l^2}{4}\right) \tag{2.122}$$

where h is rms height, l is correlation length, and k_x is surface wavenumber. It also holds that,

$$l = \sqrt{2}\frac{h}{s} \tag{2.123}$$

where s is the rms slope.

In Figure 2.6a, there is a Gaussian correlated moderately rough profile that has rms height of $\lambda/6$ and correlation length of λ, so the rms slope is approximately 13°. In Figure 2.6b, there is a Gaussian correlated very rough profile that has rms height of 0.707λ and correlation length of λ, so the rms slope is approximately 45°. The frequency is set to 1 GHz for both of the cases ($\lambda = 0.3m$).

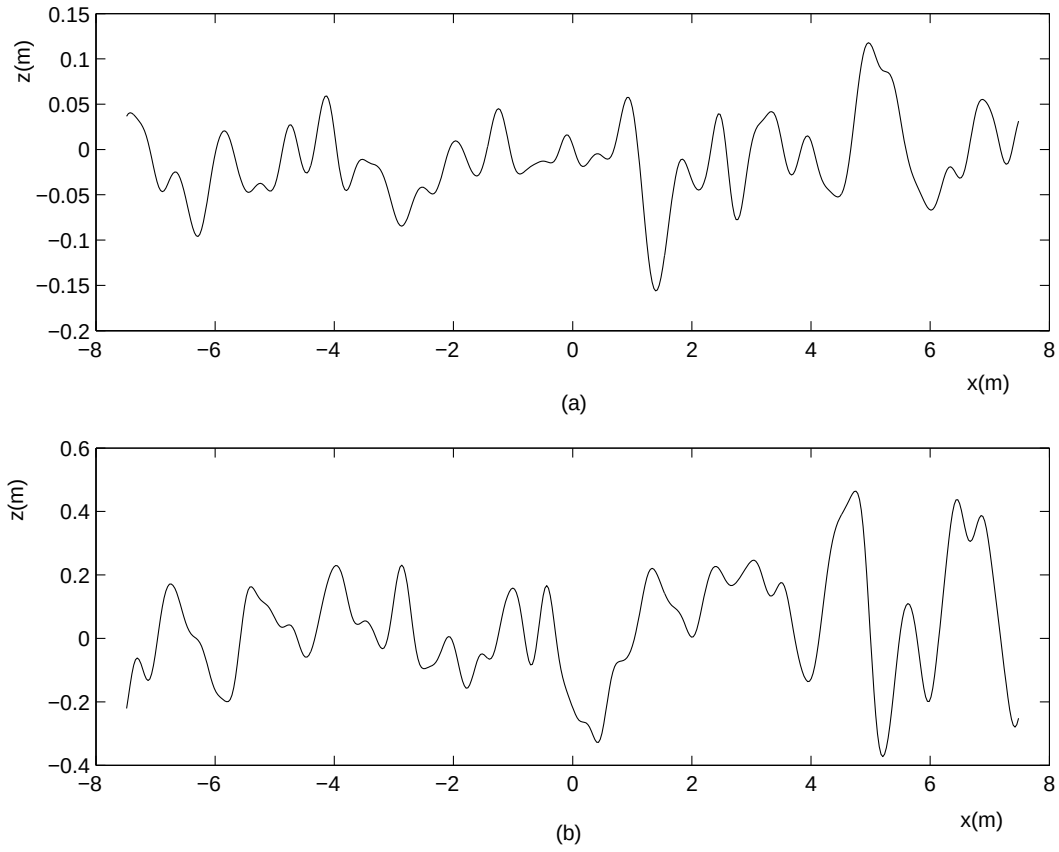

Figure 2.6: (a)Gaussian correlated moderately rough surface with $\sigma = \lambda/6, L_c = \lambda$, so that the rms slope is = 13° at 1 GHz (b)Gaussian correlated very rough surface with $\sigma = 0.707\lambda, L_c = \lambda$, so that the rms slope is = 45° at 1 GHz

2.2.2 Exponential Spectrum

Similarly, when the correlation function is exponential, i.e.,

$$C(x) = \exp\left(-\frac{|x|}{l}\right), \tag{2.124}$$

the Exponential Spectral Density can be shown to be

$$W(k_x) = \frac{h^2 l}{\pi} \frac{1}{1 + k_x^2 l^2} \tag{2.125}$$

where h is rms height, l is correlation length, and k_x is surface wavenumber.

In Figure 2.7a, there is an exponentially correlated moderately rough profile

that has rms height of $\lambda/6$ and correlation length of λ, so the rms slope is approximately 13°. In Figure 2.7b, there is an exponentially correlated very rough profile that has rms height of 0.707λ and correlation length of λ, so the rms slope is approximately 45°. The frequency is set to 1 GHz for both of the cases ($\lambda = 0.3m$).

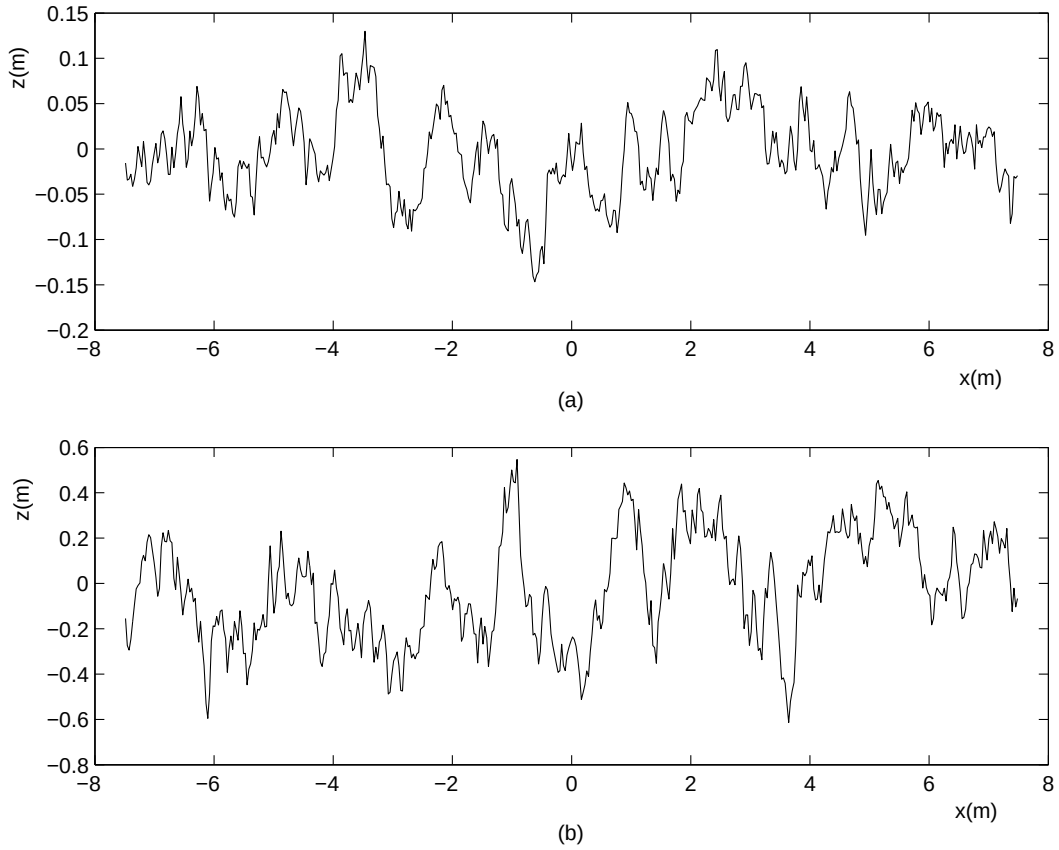

Figure 2.7: (a)Exponentially correlated moderately rough surface with $\sigma = \lambda/6, L_c = \lambda$, so that the rms slope is = 13° at 1 GHz (b)Exponentially correlated very rough surface with $\sigma = 0.707\lambda, L_c = \lambda$, so that the rms slope is = 45° at 1 GHz

2.3 Method of Moments

The method of moments (MoM) is a numerical technique that has been widely used to evaluate the field scattered by (deterministic) metallic objects in antenna and radar applications. Many detailed and interesting texts have been written on MoM [28],[33]. However, its use in the evaluation of scattering from random rough dielectric surfaces is not so widespread and is more recent. In fact, it has been first presented in [5]. In this section, we recall main concepts of the method.

MoM converts an equation that contains a linear operator into a matrix equation, which can be solved by matrix inversion. Often, the operator is an integral, which just as often contains an integrand with a singularity.

With the use of Green's function, integral equations can be derived that we have discussed at the beginning of this chapter. Consider a one dimensional integral equation of the form

$$\int_a^b dx' G(x,x') f(x') = c(x) \tag{2.126}$$

where $G(x,x')$ is the Green's function, $f(x')$ is the unknown for the domain $a \leq x' \leq b$, and $c(x)$ is known for $a \leq x \leq b$. To solve (2.126), two sets of functions are used in the MoM: Basis functions and weighting functions.

1. Basis functions: In the domain of $a \leq x \leq b$, a set of N basis functions are chosen and they are labelled as $f_1, f_2, ..., f_N$. Then the unknown function $f(x')$ is written in terms of linear combinations of these basis functions as

$$f(x') = \sum_{n=1}^{N} b_n f_n(x'). \tag{2.127}$$

The number of basis functions has to be chosen well in a sense that the linear combination of $f_n(x')$ should well represent the unknown $f(x')$ in the domain. Next, the equation (2.127) is substituted into (2.126) to obtain

$$\sum_{n=1}^{N} b_n \int_a^b dx' G(x,x') f_n(x') = c(x). \tag{2.128}$$

If the unknown coefficients $b_1, b_2, ..., b_n$ are determined then the solution is achieved.

2. Now one equation with N unknowns is obtained. However, N independent equations with the same unknowns have to be derived in order to find a solution. Next a set of N weighting functions (testing functions) $w_1(x), w_2(x), ..., w_N(x)$ is chosen. Multiplying (2.128) by $w_m(x)$ and integrating the result over the domain yields

$$\sum_{n=1}^{N} b_n \int_a^b dx w_m(x) \int_a^b dx' G(x,x') f_n(x') = \int_a^b dx w_m(x) c(x). \tag{2.129}$$

(2.129) gives the matrix equation

$$\sum_{n=1}^{N} G_{mn} b_n = c_m \tag{2.130}$$

with $m = 1, 2, ..., N$, and

$$c_m = \int_a^b dx w_m(x) c(x) = \langle w_m, c \rangle \tag{2.131}$$

$$G_{mn} = \int_a^b dx w_m(x) \int_a^b dx' G(x,x') f_n(x') = \langle w_m, G f_n \rangle \tag{2.132}$$

where the inner product notation is used such that

$$\langle f, g \rangle = \int_a^b dx f(x) g(x). \tag{2.133}$$

2.3.1 Computational Considerations

For the matrix equation (2.130) the following notes have to be taken into account.

- Matrix solution: To solve a full matrix equation of order N by matrix inversion (e.g., LU decomposition or Gaussian elimination), $O(N^3)$ number of operations will be required. Because of this, the number of operations, and so the solution time rapidly increase with an increase in N

- The unknown function: The unknown function $f(x)$ has to be decomposed into a suitable number of pieces, $f_n(x)$, in order to well represent the correct solution.The number of f_n, $n = 1, 2, ..., N$ should be neither so high that the computational cost increases nor so low that the accurate solution cannot be achieved.

2.3.2 Basis Functions

Either entire domain or subsectional basis functions can be used. Entire domain basis functions are nonzero over the entire domain of the structure (a, b) such as sines, cosines, etc. On the other hand, subsectional basis functions are nonzero over a small (subsectional) part of the entire domain such as pulse, rooftop, piecewise-sinusoidal basis functions.

A common choice for rough surface scattering type problems is the pulse basis function, which is a subsectional basis function in the form of

$$f_n(x) = \begin{cases} 1 & \text{if } a_n \leq x \leq b_n \\ 0 & \text{otherwise} \end{cases} \tag{2.134}$$

where the interval $a \leq x \leq b$ has been divided into N intervals with endpoints a_n and b_n, for $n = 1, 2, ..., N$.

2.3.3 Weighting Functions

There are two common choices for the weighting functions.

1. Galerkin's Method: In this case, the weighting functions are the same as the basis functions, i.e., $w_n(x) = f_n(x)$.

2. Point Matching Method: One can pick a set of points $x = x_1, x_2, ..., x_N$ to enforce (2.128). Then

$$\sum_{n=1}^{N} b_n \int_a^b dx' G(x_m, x') f_n(x') = c(x_m) \tag{2.135}$$

where

$$c_m = c(x_m) \tag{2.136}$$

$$G_{mn} = \int_a^b dx' G(x_m, x') f_n(x'). \tag{2.137}$$

This particular choice of testing procedure is called point matching. In terms of weighting functions, this means that the weighting functions are

$$w_m(x) = \delta(x - x_m) \tag{2.138}$$

where $m = 1, 2, ..., N$ and δ is the Dirac delta function.

In this thesis, MoM solutions are used as the reference solution. The basis functions are chosen as pulse functions and the weighting functions are chosen as Dirac delta functions.

In this chapter, the necessary background information and the governing surface integral equations for the scattering of electromagnetic waves from random rough dielectric surfaces are introduced. The solution methodology to this problem and the improvements are discussed next.

Chapter 3

Solution for the Problem

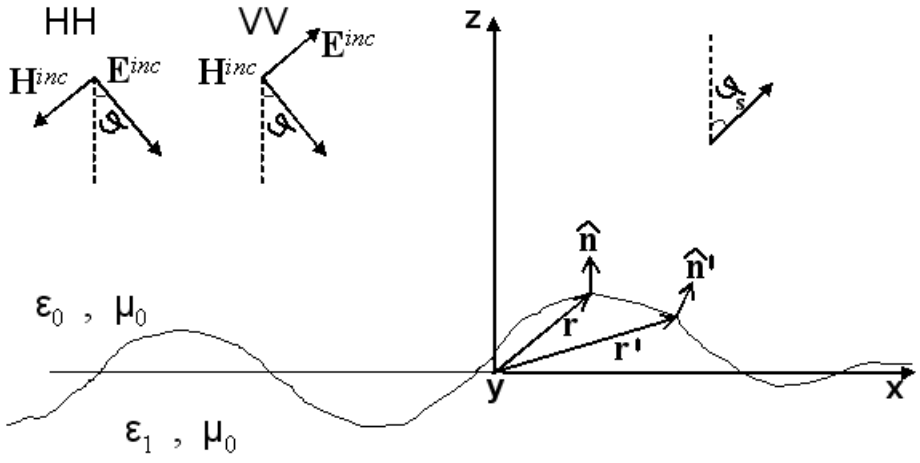

Figure 3.1: Geometry of scattering from dielectric random rough surface problem

As we discussed in Chapter 2, the solution to the problem of scattering of electromagnetic waves from random rough surfaces starts with the derivation of the corresponding surface integral equations. Then, MoM will be applied to those integral equations to solve for the unknowns.

Consider the geometry depicted in Figure 3.1. Surface height profile and electromagnetic fields are assumed to be constant along the y-direction. "HH" means that both the incident and scattered electric fields are horizontally polarized (i.e.

they have only $\hat{y}$ component) and "VV" means both the incident and scattered electric fields are vertically polarized (i.e. they don't have any $\hat{y}$ component). For this geometry, if the incident field is horizontally polarized, then the surface electric and magnetic fields can be evaluated solving the following pair of integral equations derived in Chapter 2 given by (2.78) and (2.80)

$$\begin{aligned}\hat{n}\times\mathbf{E}^{inc}(\mathbf{r}) &= -\frac{\mathbf{M}_s(\mathbf{r})}{2}+\hat{n}\times\int_S\Big[j\omega\mu_0\phi_0(\mathbf{r},\mathbf{r}')\mathbf{J}_s(\mathbf{r}')-\mathbf{M}_s(\mathbf{r}')\times\nabla\phi_0(\mathbf{r},\mathbf{r}')\\ &\quad -\frac{\nabla'_s\cdot\mathbf{J}_s(\mathbf{r}')}{j\omega\epsilon_0}\nabla\phi_0(\mathbf{r},\mathbf{r}')\Big]ds' \qquad (3.1)\\ 0 &= -\frac{\mathbf{M}_s(\mathbf{r})}{2}-\hat{n}\times\int_S\Big[j\omega\mu_0\phi_1(\mathbf{r},\mathbf{r}')\mathbf{J}_s(\mathbf{r}')-\mathbf{M}_s(\mathbf{r}')\times\nabla\phi_1(\mathbf{r},\mathbf{r}')\\ &\quad -\frac{\nabla'_s\cdot\mathbf{J}_s(\mathbf{r}')}{j\omega\epsilon_1}\nabla\phi_1(\mathbf{r},\mathbf{r}')\Big]ds'. \qquad (3.2)\end{aligned}$$

On the other hand, if the incident field is vertically polarized, then the surface electric and magnetic fields can be evaluated by solving the following pair of integral equations derived in Chapter 2 given by (2.79) and (2.81)

$$\begin{aligned}\hat{n}\times\mathbf{H}^{inc}(\mathbf{r}) &= \frac{\mathbf{J}_s(\mathbf{r})}{2}+\hat{n}\times\int_S\Big[j\omega\epsilon_0\phi_0(\mathbf{r},\mathbf{r}')\mathbf{M}_s(\mathbf{r}')+\mathbf{J}_s(\mathbf{r}')\times\nabla\phi_0(\mathbf{r},\mathbf{r}')\\ &\quad -\frac{\nabla'_s\cdot\mathbf{M}_s(\mathbf{r}')}{j\omega\mu_0}\nabla\phi_0(\mathbf{r},\mathbf{r}')\Big]ds' \qquad (3.3)\\ 0 &= \frac{\mathbf{J}_s(\mathbf{r})}{2}-\hat{n}\times\int_S\Big[j\omega\epsilon_1\phi_1(\mathbf{r},\mathbf{r}')\mathbf{M}_s(\mathbf{r}')+\mathbf{J}_s(\mathbf{r}')\times\nabla\phi_1(\mathbf{r},\mathbf{r}')\\ &\quad -\frac{\nabla'_s\cdot\mathbf{M}_s(\mathbf{r}')}{j\omega\epsilon_1}\nabla\phi_1(\mathbf{r},\mathbf{r}')\Big]ds' \qquad (3.4)\end{aligned}$$

where $\hat{n}$ is the unit outward normal to the surface. In (3.1)-(3.4), $\mathbf{M}_s=-\hat{n}\times\mathbf{E}$ is the equivalent surface magnetic current density, $\mathbf{J}_s=\hat{n}\times\mathbf{H}$ is the equivalent surface electric current density and both $\mathbf{r}$ and $\mathbf{r}'$ belong to the surface profile. First terms in (3.1)-(3.4) correspond to the case where $\mathbf{r}=\mathbf{r}'$. Since we are dealing with a two-dimensional problem, the integrals $\int_s ds'$ become $\int_l dl'$ and we use the two dimensional free-space Green's function which is the zeroth order Hankel function of the second kind given by

$$\phi_{0,1}(\mathbf{r},\mathbf{r}')=-\frac{j}{4}H_0^{(2)}(k_{0,1}|\mathbf{r}-\mathbf{r}'|) \qquad (3.5)$$

where k_0, k_1 are the propagation constants of the upper and lower media, respectively. Equations (3.1)-(3.4) assume the lower space to be homogeneous, unlimited, and with the same magnetic permeability, i.e. μ_0, of the upper one.

3.1 HH Polarization

For the scattering geometry given in Figure 3.1, the horizontally polarized incident fields are

$$\mathbf{E}^{inc} = \hat{y}e^{jk_0(-x\sin\vartheta+z\cos\vartheta)} \tag{3.6}$$

$$\mathbf{H}^{inc} = \frac{1}{\eta}(-\hat{x}\cos\vartheta-\hat{z}\sin\vartheta)e^{jk_0(-x\sin\vartheta+z\cos\vartheta)} \tag{3.7}$$

where η is the free-space intrinsic impedance. Also the induced electric surface current density on the surface is only a function of the surface contour variable r', therefore

$$\nabla'_s\cdot\mathbf{J}_s = 0. \tag{3.8}$$

This leads to a simplification to the pair of electric surface field integral equations, (3.1) and (3.2), resulting

$$\hat{n}\times\mathbf{E}^{inc}(\mathbf{r}) = -\frac{\mathbf{M}_s(\mathbf{r})}{2}+\hat{n}\times\int_l\Big[j\omega\mu_0\phi_0(\mathbf{r},\mathbf{r}')\mathbf{J}_s(\mathbf{r}')-\mathbf{M}_s(\mathbf{r}')\times\nabla\phi_0(\mathbf{r},\mathbf{r}')\Big]dl' \tag{3.9}$$

$$0 = -\frac{\mathbf{M}_s(\mathbf{r})}{2}-\hat{n}\times\int_l\Big[j\omega\mu_0\phi_1(\mathbf{r},\mathbf{r}')\mathbf{J}_s(\mathbf{r}')-\mathbf{M}_s(\mathbf{r}')\times\nabla\phi_1(\mathbf{r},\mathbf{r}')\Big]dl' \tag{3.10}$$

where l is the surface profile.

By using the following vector identity

$$\mathbf{M}_s\times\nabla\phi_{0,1} = (-\hat{n}'\times\mathbf{E})\times\nabla\phi_{0,1} = -\mathbf{E}(\hat{n}'\cdot\nabla\phi_{0,1}) \tag{3.11}$$

and considering only the scalar form of the equations, (3.9) and (3.10) can be further simplified to

$$E^{inc}(\mathbf{r}) = \frac{E(\mathbf{r})}{2}+\int_l\Big\{j\omega\mu_0\phi_0(\mathbf{r},\mathbf{r}')J_s(\mathbf{r}')+E(\mathbf{r}')\big[\hat{n}'\cdot\nabla\phi_0(\mathbf{r},\mathbf{r}')\big]\Big\}dl' \tag{3.12}$$

$$0 = \frac{E(\mathbf{r})}{2}-\int_l\Big\{j\omega\mu_0\phi_1(\mathbf{r},\mathbf{r}')J_s(\mathbf{r}')+E(\mathbf{r}')\big[\hat{n}'\cdot\nabla\phi_1(\mathbf{r},\mathbf{r}')\big]\Big\}dl' \tag{3.13}$$

where $\mathbf{E}^{inc} = E^{inc}\hat{y}$ and $\mathbf{E} = E\hat{y}$ are incident and total electric fields, respectively.

Using rectangular pulse basis functions and the point matching method, the integral equation pair (3.12)-(3.13) can be converted into a pair of matrix equations for the unknowns $\underline{E}$ and $\underline{J_s}$ given by

$$\begin{aligned} \underline{\underline{S}}_0\underline{E} + \underline{\underline{Z}}_0\underline{J_s} &= \underline{E}^{inc} \\ \underline{\underline{S}}_1\underline{E} + \underline{\underline{Z}}_1\underline{J_s} &= \underline{0} \end{aligned} \tag{3.14}$$

where $\underline{\underline{\cdot}}$ stands for a matrix and $\underline{\cdot}$ stands for a vector. Equation (3.14) can be expressed in a more compact from as

$$\underline{\underline{A}}\,\underline{x} = \underline{y} \tag{3.15}$$

with

$$\underline{\underline{A_{mn}}} = \begin{pmatrix} S_{0mn} & Z_{0mn} \\ S_{1mn} & Z_{1mn} \end{pmatrix}, \underline{x_n} = \begin{pmatrix} E_n \\ J_{s,n} \end{pmatrix}, \underline{y_m} = \begin{pmatrix} E_m^{inc} \\ 0 \end{pmatrix} \tag{3.16}$$

where the size of the matrix is $2N \times 2N$, with N being the number of rectangular pulse basis functions used to expand the unknown current density J_y and the unknown surface field E_y over the entire illuminated surface contour. The full expressions for the coefficients of the matrix elements can be obtained as

$$\begin{aligned} S_{0mn} &= \frac{1}{2}\delta_{mn} + \int_{\Delta l_n} \hat{n}' \cdot \nabla\phi_0 dl' \\ &\cong \begin{cases} \frac{1}{2} - \frac{(d^2z/dx^2)_n \Delta x}{4\pi[1+(dz/dx)_n^2]}, & m = n \\ \frac{jk_0}{4}(\hat{n}_n \cdot \mathbf{R}) H_1^{(2)}(k_0|\mathbf{r}_m - \mathbf{r}_n|)\sqrt{1+(dz/dx)_n^2}\Delta x, & m \neq n \end{cases} \end{aligned} \tag{3.17}$$

$$\begin{aligned} Z_{0mn} &= j\omega\mu_0 \int_{\Delta l_n} \phi_0 dl' \\ &\cong j\omega\mu_0 \begin{cases} -\frac{j}{4}\left(1 - \frac{2j}{\pi}\ln\frac{\gamma k_0 \sqrt{1+(dz/dx)_n^2}\Delta x}{4e}\right) & \\ \sqrt{1+(dz/dx)_n^2}\Delta x, & m = n \\ -\frac{j}{4}H_0^{(2)}(k_0|\mathbf{r}_m - \mathbf{r}_n|)\sqrt{1+(dz/dx)_n^2}\Delta x, & m \neq n \end{cases} \end{aligned} \tag{3.18}$$

$$\begin{aligned} S_{1mn} &= \frac{1}{2}\delta_{mn} - \int_{\Delta l_n} \hat{n}' \cdot \nabla\phi_1 dl' \\ &\cong \begin{cases} \frac{1}{2} + \frac{(d^2z/dx^2)_n \Delta x}{4\pi[1+(dz/dx)_n^2]}, & m = n \\ -\frac{jk_1}{4}(\hat{n}_n \cdot \mathbf{R}) H_1^{(2)}(k_1|\mathbf{r}_m - \mathbf{r}_n|)\sqrt{1+(dz/dx)_n^2}\Delta x, & m \neq n \end{cases} \end{aligned} \tag{3.19}$$

$$
\begin{aligned}
Z_{1mn} &= -j\omega\mu_0 \int_{\Delta l_n} \phi_1 dl' \\
&\cong j\omega\mu_0 \begin{cases} \frac{j}{4}\left(1 - \frac{2j}{\pi}\ln\frac{\gamma k_1 \sqrt{1+(dz/dx)_n^2}\Delta x}{4e}\right) \\ \sqrt{1+(dz/dx)_n^2}\Delta x, & m = n \\ \frac{j}{4}H_0^{(2)}(k_1|\mathbf{r}_m - \mathbf{r}_n|)\sqrt{1+(dz/dx)_n^2}\Delta x, & m \neq n. \end{cases}
\end{aligned} \tag{3.20}
$$

In (3.17)-(3.20), $\gamma = \exp(0.5772...)$, i.e., the exponential of Euler's constant, and $\mathbf{R} = (\mathbf{r}_m - \mathbf{r}_n)/|\mathbf{r}_m - \mathbf{r}_n|$, with $\mathbf{r}_m$ and $\mathbf{r}_n$ representing position vectors from the origin to the surface points at x_m and x_n, respectively. Detailed derivations of the equations (3.17)-(3.20) are given at Appendix A. Note that in (3.17) and (3.19), the second term for $m = n$ is negligible and can be ignored in the numerical computation. Furthermore, if a linear approximation of the surface contour is used, this term is exactly zero.

On the other hand, the elements of the source vector can be written from (3.6) as

$$
\mathbf{E}^{inc} = \hat{y}e^{jk_0(-x_m \sin\vartheta + z_m \cos\vartheta)}. \tag{3.21}
$$

Once the matrix $\underline{\underline{A}}$ is filled by computing all of its elements using (3.17)-(3.20), and the vector $\underline{y}$ by using (3.21), the unknown current densities and surface fields are solved. Then, the scattered field can be evaluated by inserting the obtained current densities and surface fields into

$$
E_y^s = \int_l [j\omega\mu_0\phi_0 J_y + E_y(\hat{n}' \cdot \nabla\phi_0)]dl'. \tag{3.22}
$$

In microwave remote sensing applications, the scattering coefficient is usually the parameter used to represent the scattering characteristics of extensive surface targets. To obtain the scattering coefficient, the far zone scattered field is required. Using the large argument approximation for the Hankel function and for $\nabla\phi_0$ ([27], [34]) given by

$$
\phi_0 \approx -\frac{j}{4}H_0^{(2)}(k_0 r - k_0\hat{n}_s' \cdot \mathbf{r}') \approx \frac{-je^{j\frac{\pi}{4}}}{\sqrt{8\pi k_0 r}}e^{-jk_0 r}e^{jk_0\hat{n}_s'\cdot\mathbf{r}'} \tag{3.23}
$$

$$
\nabla\phi_0 \approx \hat{n}_s\frac{jk_0}{4}H_1^{(2)}(k_0 r - k_0\hat{n}_s' \cdot \mathbf{r}') \approx \hat{n}_s\frac{(-k_0)e^{j\frac{\pi}{4}}}{\sqrt{8\pi k_0 r}}e^{-jk_0 r}e^{jk_0\hat{n}_s'\cdot\mathbf{r}'}, \tag{3.24}
$$

the far zone scattered field can be written as

$$\begin{aligned} E^s(\mathbf{r}) &= \frac{k_0 \exp(j\frac{\pi}{4})}{\sqrt{8\pi k_0 r}} \exp(-jk_0 r) \int_l [\eta J_s(\mathbf{r}') - (\hat{n}' \cdot \hat{n}_s) E(\mathbf{r}')] \exp(jk_0 \hat{n}_s \cdot \mathbf{r}') \\ &\quad \sqrt{1 + (dz/dx)^2} g(x') dx' \\ &\approx \frac{k_0 \exp[-j(k_0 r - \pi/4)]}{\sqrt{8\pi k_0 r}} \sum_{i=1}^{N} [\eta J_i - (\hat{n}_i' \cdot \hat{n}_s) E_i] \exp(jk_0 \hat{n}_s \cdot \mathbf{r}') \\ &\quad \sqrt{1 + (dz/dx)^2} g(x_i) \Delta x. \end{aligned} \tag{3.25}$$

where $\hat{n}_s$ is the unit vector indicating the scattering direction, $\mathbf{r}$ is the point in the far zone and $\mathbf{r}'$ belongs to the surface profile. In (3.25), $g(\cdot)$ is the (slowly varying) illumination function that reduces the edge effect and is assumed to be negligible for $|x'| \geq L_s/2$ where L_s is the profile length. More exactly, we assume that $g(x)$ is Gaussian with $g(0) = 1$ and a width such that $g(L_s/2) = 10^{-6}$ ([23]), so that the profile effective length can be defined as ([5],[23])

$$L_{eff} = \int_{L_s} g^2(x') dx' \tag{3.26}$$

which is directly related to the profile length, L_s.

The non-coherent normalized radar cross section (NRCS) of a 1-D profile is expressed as ([35])

$$\sigma^0 = \frac{2\pi r}{L_{eff}} \frac{|E^s|^2}{|E^{inc}|^2}. \tag{3.27}$$

If a number of random rough surfaces are generated, the mean value of the non-coherent normalized radar cross section (NRCS) of a 1-D profile is defined as ([24])

$$\sigma^0 = \frac{2\pi r \Big(\langle |E^s|^2 \rangle - |\langle E^s \rangle|^2 \Big)}{L_{eff} |E^{inc}|^2} \tag{3.28}$$

where $\langle \cdot \rangle$ stands for the mean value. This definition is based on the hypothesis that the mean square value of the scattered field is directly proportional to the profile effective length L_{eff} and has no other dependence on the illuminating function shape, so that the NRCS turns out to depend only on surface properties [23]. Equation (3.28) can be rewritten for numerical calculations as ([5])

$$\sigma^0 = \frac{2\pi r}{N_s L_{eff}} \left[\sum_{i=1}^{N_s} |E_i^s|^2 - \frac{1}{N_s} \Big| \sum_{i=1}^{N_s} E_i^s \Big|^2 \right] \tag{3.29}$$

where N_s is the number of scattered field samples.

3.2 VV Polarization

For the scattering geometry given in Figure 3.1, the vertically polarized incident fields are

$$\mathbf{H}^{inc} = \hat{y}e^{jk_0(-x\sin\vartheta+z\cos\vartheta)} \tag{3.30}$$

$$\mathbf{E}^{inc} = (\hat{x}\cos\vartheta+\hat{z}\sin\vartheta)\eta e^{jk_0(-x\sin\vartheta+z\cos\vartheta)} \tag{3.31}$$

where η is again the free-space intrinsic impedance. Also the induced magnetic surface current density on the surface is only a function of the surface contour variable r', therefore

$$\nabla_s' \cdot \mathbf{M}_s = 0. \tag{3.32}$$

Similar to the HH polarization case, this leads to a simplification to the pair of magnetic surface field integral equations, (3.3) and (3.4), resulting

$$\hat{n}\times\mathbf{H}^{inc}(\mathbf{r}) = \frac{\mathbf{J}_s(\mathbf{r})}{2} + \hat{n}\times\int_l\Big[j\omega\epsilon_0\phi_0(\mathbf{r},\mathbf{r}')\mathbf{M}_s(\mathbf{r}') + \mathbf{J}_s(\mathbf{r}')\times\nabla\phi_0(\mathbf{r},\mathbf{r}')\Big]dl' \tag{3.33}$$

$$0 = \frac{\mathbf{j}_s(\mathbf{r})}{2} - \hat{n}\times\int_l\Big[j\omega\epsilon_1\phi_1(\mathbf{r},\mathbf{r}')\mathbf{M}_s(\mathbf{r}') + \mathbf{J}_s(\mathbf{r}')\times\nabla\phi_1(\mathbf{r},\mathbf{r}')\Big]dl'. \tag{3.34}$$

By using the vector identity

$$\mathbf{J}_s\times\nabla\phi_{0,1} = (\hat{n}'\times\mathbf{H})\times\nabla\phi_{0,1} = \mathbf{H}(\hat{n}'\cdot\nabla\phi_{0,1}) \tag{3.35}$$

and considering only the scalar form of (3.33) and (3.34), they can be further simplified to

$$H^{inc}(\mathbf{r}) = \frac{H(\mathbf{r})}{2} + \int_l\Big\{j\omega\epsilon_0\phi_0(\mathbf{r},\mathbf{r}')M_s(\mathbf{r}') + H(\mathbf{r}')\big[\hat{n}'\cdot\nabla\phi_0(\mathbf{r},\mathbf{r}')\big]\Big\}dl' \tag{3.36}$$

$$0 = \frac{H(\mathbf{r})}{2} - \int_l\Big\{j\omega\epsilon_1\phi_1(\mathbf{r},\mathbf{r}')M_s(\mathbf{r}') + H(\mathbf{r}')\big[\hat{n}'\cdot\nabla\phi_1(\mathbf{r},\mathbf{r}')\big]\Big\}dl' \tag{3.37}$$

where $\mathbf{H}^{inc} = H^{inc}\hat{y}$ and $\mathbf{H} = H\hat{y}$ are incident and total magnetic fields, respectively.

Using rectangular pulse basis functions and the point matching method, the integral equation pair, (3.36)-(3.37) can be converted into a pair of matrix equations for the unknowns $\underline{H}$ and $\underline{M_s}$ given by

$$\begin{aligned} \underline{\underline{S}}_0\underline{H} + \underline{\underline{Z}}_0\underline{M_s} &= \underline{H}^{inc} \\ \underline{\underline{S}}_1\underline{H} + \underline{\underline{Z}}_1\underline{M_s} &= \underline{0}. \end{aligned} \tag{3.38}$$

Equation (3.38) can be expressed in a more compact from as

$$\underline{\underline{A}}\,\underline{x} = \underline{y} \tag{3.39}$$

with

$$\underline{\underline{A_{mn}}} = \begin{pmatrix} S_{0mn} & Z_{0mn} \\ S_{1mn} & Z_{1mn} \end{pmatrix}, \underline{x_n} = \begin{pmatrix} H_n \\ M_{s,n} \end{pmatrix}, \underline{y_m} = \begin{pmatrix} H_m^{inc} \\ 0 \end{pmatrix} \tag{3.40}$$

where the size of the matrix is $2N \times 2N$, with N being the number of rectangular pulse basis functions used to expand the unknown current density M_y and the unknown surface field H_y over the entire illuminated surface contour. The full expressions for the coefficients of the matrix elements can be obtained as

$$\begin{aligned} S_{0mn} &= \frac{1}{2}\delta_{mn} + \int_{\Delta l_n} \hat{n}' \cdot \nabla\phi_0 dl' \\ &\cong \begin{cases} \frac{1}{2} - \frac{(d^2z/dx^2)_n \Delta x}{4\pi[1+(dz/dx)_n^2]}, & m = n \\ \frac{jk_0}{4}(\hat{n}_n \cdot \mathbf{R}) H_1^{(2)}(k_0|\mathbf{r}_m - \mathbf{r}_n|)\sqrt{1+(dz/dx)_n^2}\Delta x, & m \neq n \end{cases} \end{aligned} \tag{3.41}$$

$$\begin{aligned} Z_{0mn} &= j\omega\epsilon_0 \int_{\Delta l_n} \phi_0 dl' \\ &\cong j\omega\epsilon_0 \begin{cases} -\frac{j}{4}\left(1 - \frac{2j}{\pi}\ln\frac{\gamma k_0 \sqrt{1+(dz/dx)_n^2}\Delta x}{4e}\right) & \\ \sqrt{1+(dz/dx)_n^2}\Delta x, & m = n \\ -\frac{j}{4}H_0^{(2)}(k_0|\mathbf{r}_m - \mathbf{r}_n|)\sqrt{1+(dz/dx)_n^2}\Delta x, & m \neq n \end{cases} \end{aligned} \tag{3.42}$$

$$\begin{aligned} S_{1mn} &= \frac{1}{2}\delta_{mn} - \int_{\Delta l_n} \hat{n}' \cdot \nabla\phi_1 dl' \\ &\cong \begin{cases} \frac{1}{2} + \frac{(d^2z/dx^2)_n \Delta x}{4\pi[1+(dz/dx)_n^2]}, & m = n \\ -\frac{jk_1}{4}(\hat{n}_n \cdot \mathbf{R}) H_1^{(2)}(k_1|\mathbf{r}_m - \mathbf{r}_n|)\sqrt{1+(dz/dx)_n^2}\Delta x, & m \neq n \end{cases} \end{aligned} \tag{3.43}$$

$$
\begin{aligned}
Z_{1mn} &= -j\omega\epsilon_1 \int_{\Delta l_n} \phi_1 dl' \\
&\cong j\omega\epsilon_1 \begin{cases} \frac{j}{4}\left(1 - \frac{2j}{\pi}\ln\frac{\gamma k_1 \sqrt{1+(dz/dx)_n^2}\Delta x}{4e}\right) & \\ \sqrt{1+(dz/dx)_n^2}\Delta x, & m = n \\ \frac{j}{4}H_0^{(2)}(k_1|\mathbf{r}_m - \mathbf{r}_n|)\sqrt{1+(dz/dx)_n^2}\Delta x, & m \neq n. \end{cases}
\end{aligned} \tag{3.44}
$$

In (3.41)-(3.44), $\gamma = \exp(0.5772...)$, i.e., the exponential of Euler's constant, and $\mathbf{R} = (\mathbf{r}_m - \mathbf{r}_n)/|\mathbf{r}_m - \mathbf{r}_n|$, with $\mathbf{r}_m$ and $\mathbf{r}_n$ representing position vectors from the origin to the surface points at x_m and x_n, respectively. Detailed derivations of the equations (3.41)-(3.44) are given at Appendix A. Note that in (3.41) and (3.43), the second term for $m = n$ is negligible and can be ignored in the numerical computation. Furthermore, if a linear approximation of the surface contour is used, this term is exactly zero.

On the other hand, the elements of the source vector can be written from (3.30) as

$$
\mathbf{H}^{inc} = \hat{y} e^{jk_0(-x_m \sin\vartheta + z_m \cos\vartheta)}. \tag{3.45}
$$

Once the matrix $\underline{\underline{A}}$ is filled by computing all of its elements using (3.41)-(3.44), and the vector $\underline{y}$ by using (3.45), the unknown current densities and surface fields are solved. The scattered field can be evaluated by inserting the solved current densities and surface fields into

$$
H_y^s = \int_l [j\omega\epsilon_0\phi_0 M_y + H_y(\hat{n}' \cdot \nabla\phi_0)] dl'. \tag{3.46}
$$

Using (3.23) and (3.24), the far zone scattered magnetic fields can now be written as

$$
\begin{aligned}
H^s(\mathbf{r}) &= \frac{k_0 \exp(j\frac{\pi}{4})}{\sqrt{8\pi k_0 r}} \exp(-jk_0 r) \int_l [\frac{M_s(\mathbf{r}')}{\eta} - (\hat{n}' \cdot \hat{n}_s) H(\mathbf{r}')] \exp(jk_0 \hat{n}_s \cdot \mathbf{r}') \\
&\quad \sqrt{1+(dz/dx)^2} g(x') dx' \\
&\approx \frac{k_0 \exp[-j(k_0 r - \pi/4)]}{\sqrt{8\pi k_0 r}} \sum_{i=1}^{N} [\frac{M_i}{\eta} - (\hat{n}_i' \cdot \hat{n}_s) H_i] \exp(jk_0 \hat{n}_s \cdot \mathbf{r}') \\
&\quad \sqrt{1+(dz/dx)^2} g(x_i) \Delta x.
\end{aligned} \tag{3.47}
$$

In (3.47), $g(\cdot)$ is the (slowly varying) illumination function that reduces the edge effect and is assumed to be negligible for $|x'| \geq L_s/2$ where L_s is the profile length. And the profile effective length is as same as (3.26).

The non-coherent normalized radar cross section (NRCS) of a 1-D profile is expressed as

$$\sigma^0 = \frac{2\pi r}{L_{eff}} \frac{|H^s|^2}{|H^{inc}|^2}. \tag{3.48}$$

If a number of random rough surfaces are generated, then the mean value of the non-coherent normalized radar cross section (NRCS) of a 1-D profile is defined as

$$\sigma^0 = \frac{2\pi r \left(\langle |H^s|^2 \rangle - |\langle H^s \rangle|^2 \right)}{L_{eff} |H^{inc}|^2} \tag{3.49}$$

where $\langle \cdot \rangle$ stands for the mean value. Finally, the equation (3.49) can be rewritten for numerical calculations as ([5])

$$\sigma^0 = \frac{2\pi r}{N_s L_{eff}} \left[\sum_{i=1}^{N_s} |H_i^s|^2 - \frac{1}{N_s} \Big| \sum_{i=1}^{N_s} H_i^s \Big|^2 \right] \tag{3.50}$$

where N_s is the number of scattered field samples.

3.3 Solution Procedure

The corresponding equations for the solution of scattering of electromagnetic waves from random rough dielectric surfaces are derived in (3.17)-(3.20) for HH polarization and (3.41)-(3.44) for VV polarization. However, if the number of the matrix elements is high, then the solution for that matrix equation will be difficult due to reasonings explained in Section 2.3.1. Then our aim is to find faster solution methodologies to the matrix equations in order not to struggle with the computational constraints that are mentioned in Section 2.3.1 for electrically large terrains.

In the next chapter, several iterative algorithms which accelerates the solution are presented.

Chapter 4

Iterative Algorithms

Numerical Linear Algebra is an effective way of solving linear systems, such as $\underline{\underline{A}}\,\underline{x} = \underline{b}$. The computer can solve an easier equation many times and each answer $\underline{x}_k$ goes back into the same equation to find the next guess $\underline{x}_{k+1}$. The direct method for these systems, such as the LU decomposition, requires $O(N^3)$ operations. However, by using iterative methods this number can be reduced to $O(N^2)$ operations. The term "Iterative Method" refers to a wide range of techniques that use successive approximations to obtain more accurate solutions to a linear system at each step [36]. There are two kinds of iterative methods, one of them is stationary iterative methods, and the other is nonstationary ones. Stationary methods are simpler and older with respect to nonstationary ones and as a result they are less efficient. However, nonstationary methods, if applied to the right systems, are extremely useful that the answer can be reached in less number of iterations. In this chapter, first of all, one stationary, namely Forward-Backward method (FBM) is examined. Before proceeding with the nonstationary methods used in this thesis, Conjugate Gradient (CG) and BiConjugate Gradient (BiCG) methods are discussed briefly, since they are the building blocks of other nonstationary algorithms. Then three nonstationary methods, namely Conjugate Gradient Squared (CGS), BiConjugate Gradient Stabilized (Bi-CGSTAB) and Quasi-Minimal Residual (QMR) methods are examined.

4.1 Stationary Methods

In this part, the FBM is described as the stationary method which is implemented in this thesis. First, the FBM for scattering from the rough impedance and PEC surface problem is described. Then, modifications are given for the scattering from rough dielectric surfaces.

4.1.1 Forward-Backward Method

Consider the matric equation

$$\underline{V} = \underline{\underline{Z}} \cdot \underline{I} \tag{4.1}$$

obtained by applying the MoM procedure to the integral equation derived for the scattering from impedance and/or PEC rough surfaces. In (4.1), $\underline{\underline{Z}}$ is the MoM impedance matrix and $\underline{V}$ is the column vector. The system defined by (4.1) should be solved for unknown current coefficients $\underline{I} = \{I_m\}$ in order to find the induced current on the surface.

FBM proposes a forward and backward decomposition over the matrices and vectors involved in (4.1) such that

$$\underline{I} = \underline{I}^f + \underline{I}^b \tag{4.2}$$

$$\underline{\underline{Z}} = \underline{\underline{Z}}^f + \underline{\underline{Z}}^s + \underline{\underline{Z}}^b, \tag{4.3}$$

where $\underline{I}^f$ is the forward component denoting the current distribution due to the wave propagation in the forward direction and $\underline{I}^b$ is the backward component representing the current distribution due to the wave propagation in the backward direction. In (4.3), $\underline{\underline{Z}}^f$ and $\underline{\underline{Z}}^b$ are the impedance matrices consisting of elements in the lower and upper triangular parts of $\underline{\underline{Z}}$ excluding the diagonal terms, respectively. It is noted that $\underline{\underline{Z}}^s$ is a diagonal matrix consisting only of the self impedances of all surface segments [37].

Using (4.2) and (4.3), the matrix equation given by (4.1) can be separated

into two matrix equations, namely

$$\underline{\underline{Z}}^s \cdot \underline{I}^f = \underline{V} - \underline{\underline{Z}}^f \cdot \left(\underline{I}^f + \underline{I}^b\right) \quad (4.4)$$

$$\underline{\underline{Z}}^s \cdot \underline{I}^b = -\underline{\underline{Z}}^b \cdot \left(\underline{I}^f + \underline{I}^b\right). \quad (4.5)$$

The second term in the right-hand side of (4.4) represents the forward propagating field contribution due to the radiation of current elements in front (elements where $x < x_n$) of the receiving element. Likewise, the term on the right-hand side of (4.5) represents the backward propagating field contribution due to the radiation of current elements in the rear (elements where $x > x_n$) of the receiving element. Therefore, (4.4) and (4.5) may be defined as the forward propagation and backward propagation equations, respectively. The total induced current on the nth receiving element is composed of the sum of the forward $\left(\underline{I}^f\right)$ and backward $\left(\underline{I}^b\right)$ field-induced currents. An iterative procedure can be used to solve forward and backward propagation equations by initializing $\underline{I}^{b,0} = 0$, and at the nth sweep,

$$\left(\underline{\underline{Z}}^s + \underline{\underline{Z}}^f\right) \cdot \underline{I}^{f,(n)} = \underline{V} - \underline{\underline{Z}}^f \cdot \underline{I}^{b,(n-1)} \quad (4.6)$$

$$\left(\underline{\underline{Z}}^s + \underline{\underline{Z}}^b\right) \cdot \underline{I}^{b,(n)} = -\underline{\underline{Z}}^b \cdot \underline{I}^{f,(n)}. \quad (4.7)$$

Since $\underline{\underline{Z}}^s + \underline{\underline{Z}}^b$ is an upper triangular matrix and $\underline{\underline{Z}}^s + \underline{\underline{Z}}^f$ is a lower triangular matrix, the matrices in this iterative process do not need to be factorized or inverted. Thus, (4.6) and (4.7) can be solved for $\underline{I}^{f,(n)}$ and $\underline{I}^{b,(n)}$ by forward and backward substitution, respectively. Iterations are continued until surface currents show convergence to within a specified accuracy criterion.

FBM presents very fast convergence within a few iterations. Using FBM, there is no need to store the elements of the impedance matrix, because of the sweeping procedure. However, the surface height data, incident field values at matching points, and forward, backward and total currents have to be stored in N element arrays, where N is the surface unknowns. Therefore, the memory requirement of the method is $O(N)$. The matrix elements are recomputed at each iteration with a computational cost of $O(QN^2)$, where Q is the number of iterations. Since the method obtains very accurate results within a few iterations (usually Q is less than 10), the total computational requirement of the method becomes $O(N^2)$ for very large N values [37].

The FBM algorithm is mathematically equivalent to the well-known *symmetric successive over relaxation - SSOR* iteration [12]. This method is very good at obtaining accurate results, when the matrix in the linear equation system is diagonally dominant. However, investigation of dielectric surfaces with this method or changing the order of current elements disturb the diagonally dominant nature (re-entrant surfaces), which in turn, strongly affect the convergence of the method. The algorithm may become unstable for such surfaces that the method should be modified even to satisfy convergence for some of those cases.

Thus, for the case of scattering from dielectric rough surfaces, implementation of the FBM should be slightly modified [24]. Following the work done in [24], the integral equation pair of HH polarization derived for the scattering from dielectric rough surfaces (3.12)-(3.13) are converted into a pair of matrix equations (3.14) given by

$$\begin{aligned} \underline{\underline{S}}_0 \underline{E} + \underline{\underline{Z}}_0 \underline{J_s} &= \underline{E}^{inc} \\ \underline{\underline{S}}_1 \underline{E} + \underline{\underline{Z}}_1 \underline{J_s} &= \underline{0} \end{aligned} \tag{4.8}$$

and similarly, integral equation pair of VV polarization, (3.36)-(3.37) are converted into a pair of matrix equations (3.38) given by

$$\begin{aligned} \underline{\underline{S}}_0 \underline{H} + \underline{\underline{Z}}_0 \underline{M_s} &= \underline{H}^{inc} \\ \underline{\underline{S}}_1 \underline{H} + \underline{\underline{Z}}_1 \underline{M_s} &= \underline{0}. \end{aligned} \tag{4.9}$$

As done in the previous chapter, both can be expressed in a more compact form as

$$\underline{\underline{A}}\,\underline{x} = \underline{y} \tag{4.10}$$

where

$$\underline{\underline{A_{mn}}} = \begin{pmatrix} S_{0mn} & Z_{0mn} \\ S_{1mn} & Z_{1mn} \end{pmatrix}, \underline{x_n} = \begin{pmatrix} X_n \\ Y_{s,n} \end{pmatrix}, \underline{y_m} = \begin{pmatrix} X_m^{inc} \\ 0 \end{pmatrix}. \tag{4.11}$$

In (4.11), $\underline{\underline{A_{mn}}}$ are 2×2 submatrices of $\underline{\underline{A}}$, so that the size of the matrix $\underline{\underline{A}}$ is $2N \times 2N$, where N is the number of rectangular pulse basis functions used to expand the unknown functions. Furthermore, to let (4.11) be a general representation of the matrix equations for HH and VV polarizations, we let X stand for the total

electric field (E), X^{inc} stand for the incident electric field (E^{inc}) and Y_s stand for the equivalent electric surface current density (J_s) for HH polarization, and X stand for the total magnetic field (H), X^{inc} stand for the incident magnetic field (H^{inc}) and Y_s stand for the equivalent magnetic surface current density (M_s) for VV polarization. We start the forward backward procedure from (4.11) and let

$$\begin{aligned} \underline{X} &= \underline{X}^f + \underline{X}^b \\ \underline{Y_s} &= \underline{Y_s}^f + \underline{Y_s}^b \end{aligned} \tag{4.12}$$

and

$$\begin{aligned} \underline{\underline{S}}_0 &= \underline{\underline{S}}^L_0 + \underline{\underline{S}}^D_0 + \underline{\underline{S}}^U_0 \\ \underline{\underline{Z}}_0 &= \underline{\underline{Z}}^L_0 + \underline{\underline{Z}}^D_0 + \underline{\underline{Z}}^U_0 \\ \underline{\underline{S}}_1 &= \underline{\underline{S}}^L_1 + \underline{\underline{S}}^D_1 + \underline{\underline{S}}^U_1 \\ \underline{\underline{Z}}_1 &= \underline{\underline{Z}}^L_1 + \underline{\underline{Z}}^D_1 + \underline{\underline{Z}}^U_1 \end{aligned} \tag{4.13}$$

wherein $\underline{X}^f$ and $\underline{Y_s}^f$ are the forward components, while $\underline{X}^b$ and $\underline{Y_s}^b$ are the backward components. In addition, $\underline{\underline{S}}^L_{0,1}$ and $\underline{\underline{Z}}^L_{0,1}$ are the lower triangular parts of $\underline{\underline{S}}_{0,1}$ and $\underline{\underline{Z}}_{0,1}$, respectively; $\underline{\underline{S}}^D_{0,1}$ and $\underline{\underline{Z}}^D_{0,1}$ are the diagonal parts; and $\underline{\underline{S}}^U_{0,1}$ and $\underline{\underline{Z}}^U_{0,1}$ are their upper triangular parts. Then using (4.12) and (4.13) in (4.11), (4.11) can be decomposed into forward-propagation and backward-propagation pairs of equations as

$$\underline{\underline{S}}^D_0\underline{X}^f + \underline{\underline{Z}}^D_0\underline{Y_s}^f = \underline{X}^{inc} - \underline{\underline{S}}^L_0\Big(\underline{X}^f + \underline{X}^b\Big) - \underline{\underline{Z}}^L_0\Big(\underline{Y_s}^f + \underline{Y_s}^b\Big)$$

$$\underline{\underline{S}}^D_1\underline{X}^f + \underline{\underline{Z}}^D_1\underline{Y_s}^f = -\underline{\underline{S}}^L_1\Big(\underline{X}^f + \underline{X}^b\Big) - \underline{\underline{Z}}^L_1\Big(\underline{Y_s}^f + \underline{Y_s}^b\Big) \tag{4.14}$$

$$\underline{\underline{S}}^D_0\underline{X}^b + \underline{\underline{Z}}^D_0\underline{Y_s}^b = -\underline{\underline{S}}^U_0\Big(\underline{X}^f + \underline{X}^b\Big) - \underline{\underline{Z}}^U_0\Big(\underline{Y_s}^f + \underline{Y_s}^b\Big)$$

$$\underline{\underline{S}}^D_1\underline{X}^b + \underline{\underline{Z}}^D_1\underline{Y_s}^b = -\underline{\underline{S}}^U_1\Big(\underline{X}^f + \underline{X}^b\Big) - \underline{\underline{Z}}^U_1\Big(\underline{Y_s}^f + \underline{Y_s}^b\Big). \tag{4.15}$$

Equation (4.14) defines the forward components of magnetic and electric equivalent surface currents, and explicitly shows that they are due to the incident electric field and to the radiation of current elements placed on the left of the considered surface element. In a similar fashion equation (4.15) defines the backward components of the corresponding surface currents and clearly shows that they are due to the radiation of current elements placed on the right of the considered surface element.

Equations (4.14) and (4.15) can be rewritten in a more compact form as

$$\underline{\underline{A}}^{D}\underline{I}^{f} = \underline{V} - \underline{\underline{A}}^{L}\left(\underline{I}^{f} + \underline{I}^{b}\right) \tag{4.16}$$

$$\underline{\underline{A}}^{D}\underline{I}^{b} = -\underline{\underline{A}}^{U}\left(\underline{I}^{f} + \underline{I}^{b}\right). \tag{4.17}$$

which are very similar to (4.4) and (4.5). However the matrices and vectors in (4.16) and (4.17) are block matrices and vectors and given by

$$\underline{\underline{A^{L}_{mn}}} = \begin{pmatrix} S^{L}_{0mn} & Z^{L}_{0mn} \\ S^{L}_{1mn} & Z^{L}_{1mn} \end{pmatrix}, \quad \underline{\underline{A^{D}_{mn}}} = \begin{pmatrix} S^{D}_{0mn} & Z^{D}_{0mn} \\ S^{D}_{1mn} & Z^{D}_{1mn} \end{pmatrix}, \quad \underline{\underline{A^{U}_{mn}}} = \begin{pmatrix} S^{U}_{0mn} & Z^{U}_{0mn} \\ S^{U}_{1mn} & Z^{U}_{1mn} \end{pmatrix} \tag{4.18}$$

$$\underline{{I_n}^{f}} = \begin{pmatrix} X^{f}_{n} \\ Y^{f}_{s,n} \end{pmatrix}, \quad \underline{{I_n}^{b}} = \begin{pmatrix} X^{b}_{n} \\ Y^{b}_{s,n} \end{pmatrix}. \tag{4.19}$$

Note that, while $\underline{\underline{A}}^{L}$ and $\underline{\underline{A}}^{U}$ are lower and upper triangular matrices, respectively, $\underline{\underline{A}}^{D}$ is a block diagonal matrix, with blocks of 2×2.

Equations (4.16) and (4.17) can be solved iteratively as in the original FBM. Currents $\underline{I}^{f,(i)}$, $\underline{I}^{b,(i)}$ at the ith step can be obtained by using the following set of equations:

$$\left(\underline{\underline{A}}^{D} + \underline{\underline{A}}^{L}\right)\underline{I}^{f,(i)} = \underline{V} - \underline{\underline{A}}^{L}\underline{I}^{b,(i-1)} \tag{4.20}$$

$$\left(\underline{\underline{A}}^{D} + \underline{\underline{A}}^{U}\right)\underline{I}^{b,(i)} = -\underline{\underline{A}}^{U}\underline{I}^{f,(i)} \tag{4.21}$$

with $\underline{I}^{b,(0)} = 0$.

From (4.20), one can conclude that $\left(\underline{\underline{A}}^{D} + \underline{\underline{A}}^{L}\right)$ is a block-lower triangular matrix with 2×2 blocks and can be solved by forward substitution as follows ([24]): Let $\underline{\underline{A}}^{DL} = \left(\underline{\underline{A}}^{D} + \underline{\underline{A}}^{L}\right)$ and $\underline{V}^{(i)} = \underline{V} - \underline{\underline{A}}^{L}\underline{I}^{b,(i-1)}$, then

$$\begin{aligned} \underline{{I_1}}^{f,(i)} &= \left(\underline{\underline{A_{11}}}^{DL}\right)^{-1}\underline{V_1}^{(i)} \\ \underline{{I_n}}^{f,(i)} &= \left(\underline{\underline{A_{nn}}}^{DL}\right)^{-1}\left(\underline{V_n}^{(i)} - \sum_{k=1}^{n-1}\underline{\underline{A_{nk}}}^{DL}\underline{I_k}^{f,(i)}\right) \\ &\quad \text{with} \quad n = 2, 3, ..., N. \end{aligned} \tag{4.22}$$

Similarly, from (4.21), the matrix $\left(\underline{\underline{A}}^D + \underline{\underline{A}}^U\right)$ is a block-upper triangular matrix with 2×2 blocks and can be solved by backward substitution as follows: Let $\underline{\underline{A}}^{DU} = \left(\underline{\underline{A}}^D + \underline{\underline{A}}^U\right)$ and $\underline{V}^{(i)} = -\underline{\underline{A}}^U \underline{I}^{f,(i)}$, then

$$\begin{aligned} \underline{I_1}^{b,(i)} &= \left(\underline{\underline{A_{11}}}^{DU}\right)^{-1} \underline{V_1}^{(i)} \\ \underline{I_n}^{b,(i)} &= \left(\underline{\underline{A_{nn}}}^{DU}\right)^{-1} \left(\underline{V_n}^{(i)} - \sum_{k=1}^{n-1} \underline{\underline{A_{nk}}}^{DU} \underline{I_k}^{b,(i)}\right) \\ &\quad \text{with} \quad n = 2, 3, ..., N. \end{aligned} \tag{4.23}$$

Equation (4.22) for forward substitution or (4.23) for backward substitution shows that each step of the algorithm requires the solution of a linear system of two equations in two unknowns, so that only a simple inversion of a 2×2 matrix is needed. Thus, the solution for all unknowns for each of (4.22) and (4.23) requires $N(N-1)/2$ products of 2×2 matrices by two-element column vectors and N inversions of 2×2 matrices. In conclusion, totally $4N(N-1) + 6N = 4N^2 + 2N$ complex multiplications required, leading to the conclusion that the complexity of the overall algorithm is $O(N^2)$.

4.2 Nonstationary Methods

Nonstationary methods discussed here are CGS, Bi-CGSTAB and QMR methods which are the derivatives of Conjugate Gradient (CG) and BiConjugate Gradient (BiCG) Method. Therefore, first the CG and BiCG methods are briefly discussed, which will supply a deep inside for the other methods used, namely, CGS, Bi-CGSTAB and QMR. Most of the following descriptions are directly taken from [36].

4.2.1 Conjugate Gradient Method [36]

CG is an effective method for symmetric positive definite systems. It is the oldest and the best known of the nonstationary methods. The method proceeds

by generating vector sequences of iterates (i.e., successive approximations to the solution), residuals corresponding to the iterates, and search directions used in updating the iterates and residuals. Although the length of these sequences can become large, only a small number of vectors are required to be kept in memory. In every iteration of the method, two inner products are performed in order to compute update scalars that are defined to make the sequences satisfy certain orthogonality conditions. On a symmetric positive definite linear system these conditions imply that the distance to the true solution is minimized in some norm [36]. Only the results of the previous iteration need to be stored.

The iterates $\underline{x}^i$ are updated in each iteration by a multiple (α_i) of the search vector $\underline{p}^i$:

$$\underline{x}^{(i)} = \underline{x}^{(i-1)} + \alpha_i \underline{p}^{(i)} \tag{4.24}$$

Correspondingly the residuals $\underline{r}^{(i)} = \underline{b} - \underline{\underline{A}}\,\underline{x}^{(i)}$ are updated as

$$\underline{r}^{(i)} = \underline{r}^{(i-1)} + \alpha \underline{q}^{(i)} \text{where} \underline{q}^{(i)} = \underline{\underline{A}}\,\underline{p}^{(i)} \tag{4.25}$$

The choice $\alpha = \alpha_i = \underline{r}^{(i-1)^T}\underline{r}^{(i-1)} / \underline{p}^{(i)^T}\underline{\underline{A}}\,\underline{p}^{(i)}$ minimizes $\underline{r}^{(i)^T}\underline{\underline{A}}^{-1}\underline{r}^{(i)}$ over all possible choices for α in equation (4.25).

The search directions are updated using the residuals

$$\underline{p}^{(i)} = \underline{r}^{(i)} + \beta_{i-1}\underline{p}^{(i-1)} \tag{4.26}$$

where the choice $\beta_i = \underline{r}^{(i)^T}\underline{r}^{(i)} / \underline{r}^{(i-1)^T}\underline{r}^{(i-1)}$ ensures that $\underline{p}^{(i)}$ and $\underline{\underline{A}}\,\underline{p}^{(i-1)}$ or equivalently $\underline{r}^{(i)}$ and $\underline{r}^{(i-1)}$ are orthogonal. In fact, one can show that this choice of β_i makes $\underline{p}^{(i)}$ and $\underline{r}^{(i)}$ orthogonal to all previous $\underline{\underline{A}}\,\underline{p}^{(j)}$ and $\underline{r}^{(j)}$ respectively.

4.2.1.1 Convergence of CG [36]

The Unpreconditioned Conjugate Gradient Method constructs the ith iterate $\underline{x}^{(i)}$ as an element of $\underline{x}^{(0)} + \text{span}\big(\underline{r}^{(0)}, ..., \underline{\underline{A}}^{(i-1)}\underline{r}^{(0)}\big)$ so that $(\underline{x}^{(i)} - \underline{\hat{x}})^T\underline{\underline{A}}(\underline{x}^{(i)} - \underline{\hat{x}})$ is minimized, where $\underline{\hat{x}}$ is the exact solution of $\underline{\underline{A}}\,\underline{x} = \underline{b}$. This minimum and so the convergence of the method is guaranteed to exist in general only if $\underline{\underline{A}}$ is symmetric positive definite.

Pseudocode:

Compute $\underline{r}^{(0)} = \underline{b} - \underline{\underline{A}}\,\underline{x}^{(0)}$ for some initial guess $\underline{x}^{(0)}$
for $i = 1, 2, ...$
  solve $\underline{\underline{M}}\,\underline{z}^{(i-1)} = \underline{r}^{(i-1)}$
  $\rho_{i-1} = \underline{r}^{(i-1)^T}\underline{z}^{(i-1)}$
  if $i = 1$
    $\underline{p}^{(1)} = \underline{z}^{(0)}$
  else
    $\beta_{i-1} = \rho_{i-1}/\rho_{i-2}$
    $\underline{p}^{(i)} = \underline{z}^{(i-1)} + \beta_{i-1}\underline{p}^{(i-1)}$
  endif
  $\underline{q}^{(i)} = \underline{\underline{A}}\,\underline{p}^{(i)}$
  $\alpha_i = \rho_{i-1}/\underline{p}^{(i)^T}\underline{q}^{(i)}$
  $\underline{x}^{(i)} = \underline{x}^{(i-1)} + \alpha_i\underline{p}^{(i)}$
  $\underline{r}^{(i)} = \underline{r}^{(i-1)} - \alpha_i\underline{q}^{(i)}$
  check convergence; continue if necessary
end

Figure 4.1: Pseudocode of the Preconditioned Conjugate Gradient Method

Since the matrices for our problem are not positive definite, then CG method is not effective for the solution of our problem.

4.2.1.2 Implementation of CG [36]

CG involves one matrix-vector product, three vector updates and two inner products per iteration. The pseudocode for the Preconditioned Conjugate Gradient Method is given in Figure 4.1 ([36]). It uses a preconditioner $\underline{\underline{M}}$. Preconditioners are very commonly used matrix forms which enhance the condition number of the original matrix $\underline{\underline{A}}$, thus generally reducing the number of iterations to converge to the solution of the linear system. If a good preconditioner is constructed, then the iterative technique can improve by means of iteration number, but the effort in terms of computational cost usually increases. For $\underline{\underline{M}} = \underline{\underline{I}}$ (where $\underline{\underline{I}}$ is the identity matrix), one obtains the unpreconditioned version of the conjugate gradient

algorithm. In that case, the algorithm may be further simplified by skipping the "solve" line, and replacing $\underline{z}^{(i-1)}$ by $\underline{r}^{(i-1)}$ (and $\underline{z}^{(0)}$ by $\underline{r}^{(0)}$).

4.2.1.3 Preconditioning

Because a large condition number of $\underline{\underline{A}}$ slows down the convergence of the CG method, it is natural to think if the condition number of $\underline{\underline{A}}$ can be lessened before the implementation. In the case of a good preconditioner, the rate of convergence of the method will be very explicit. One of the most common preconditioning is Jacobi preconditioning which is the one used in the implementations of the methods here.

Jacobi Preconditioning: This is the simplest preconditioner consists of just the diagonal of the matrix. ($\underline{\underline{M_{ii}}} = \underline{\underline{A_{ij}}}$ if $i = j$, the rest of the entries are zero.) It is possible to use this preconditioner without using any extra storage beyond that of the matrix itself. However, division operations are usually quite costly, so in practice storage is allocated for the reciprocals of the matrix diagonal. On the other hand, on parallel computers this preconditioner does not present any particular problems. The algorithm will normally develop due to preconditioning.

4.2.2 BiConjugate Gradient Method [36]

CG is not suitable for nonsymmetrical systems because the residual vectors cannot be made orthogonal with short recurrences. BiCG somehow related to CG, that there are two matrices formed and they are solved in the sense of CG. To be more explicit, instead of an orthogonal sequence (idea in CG), two mutually orthogonal sequences are formed. It provides two update sequences of the residuals

$$\underline{r}^{(i)} = \underline{r}^{(i-1)} + \alpha_i \underline{\underline{A}}\, \underline{p}^{(i)}, \hat{\underline{r}}^{(i)} = \hat{\underline{r}}^{(i-1)} + \alpha_i \underline{\underline{A}}^T \hat{\underline{p}}^{(i)} \tag{4.27}$$

and two sequences of search directions

$$\underline{p}^{(i)} = \underline{r}^{(i-1)} + \beta_{i-1} \underline{p}^{(i-1)}, \hat{\underline{p}}^{(i)} = \hat{\underline{r}}^{(i-1)} + \beta_{i-1} \hat{\underline{p}}^{(i-1)} \tag{4.28}$$

The choices:

$$\alpha_i = \frac{\underline{\hat{r}}^{(i-1)^T}\underline{r}^{(i-1)}}{\underline{\hat{p}}^{(i)^T}\underline{\underline{A}}\,\underline{p}^{(i)}}, \beta_i = \frac{\underline{\hat{r}}^{(i)^T}\underline{r}^{(i)}}{\underline{\hat{r}}^{(i-1)^T}\underline{r}^{(i-1)}} \tag{4.29}$$

ensures the bi-orthogonality relations

$$\underline{\hat{r}}^{(i)^T}\underline{r}^{(i)} = \underline{\hat{p}}^{(i)^T}\underline{\underline{A}}\,\underline{p}^{(i)} = 0 \text{ if } i \neq j. \tag{4.30}$$

4.2.2.1 Convergence of BiCG [36]

Few theoretical results are known about the convergence of BiCG. For symmetric positive definite systems the method delivers the same results as CG, but at twice the cost per iteration. For nonsymmetrical matrices it has been shown that in phases of the process where there is significant reduction of the norm of the residual. In practice this is often confirmed, but it is also observed that the convergence behavior may be quite irregular, and the method may even break down. The breakdown situation due to the possible event is $\underline{z}^{(i-1)^T}\underline{\hat{r}}^{(i-1)} \approx 0$. The other breakdown situation is $\underline{\hat{p}}^{(i)^T}\underline{q}^{(i)} \approx 0$ and it occurs when the LU-decomposition fails and can be repaired by using another decomposition. This is done in the version of quasi minimal residual method (QMR).

Sometimes, breakdown or near-breakdown situations can be satisfactorily avoided by a restart at the iteration step immediately before the (near-) breakdown step.

4.2.2.2 Implementation of BiCG [36]

BiCG requires computing a matrix-vector product $\underline{\underline{A}}\,\underline{p}^{(k)}$ and a transpose product $\underline{\underline{A}}^T\,\underline{\hat{p}}^{(k)}$. In some applications the latter product may be impossible to perform, for instance if the matrix is not formed explicitly and the regular product is only given in operation form, for instance as a function call evaluation. In a parallel environment, the two matrix-vector products can theoretically be performed simultaneously; however, in a distributed-memory environment, there will be extra communication costs associated with one of the two matrix-vector products,

depending upon the storage scheme for $\underline{\underline{A}}$. A duplicate copy of the matrix will alleviate this problem, at the cost of doubling the storage requirements for the matrix. Care must also be exercised in choosing the preconditioner, since similar problems arise during the two solves involving the preconditioning matrix.

The pseudocode for the Preconditioned BiConjugate Gradient Method is given in Figure 4.2 ([36]). If the algorithm is examined, everything is as same as the algorithm of CG method, but the iterations go on in two directions one of which starts with $\underline{\underline{A}}$ and the other starts with $\underline{\underline{A^T}}$. Because of this the number of the calculations will be twice more when compared to CG method.

4.2.3 Conjugate Gradient Squared Method [36]

CGS generates two sequences, both of which are conjugate gradient sequences; however, the matrix used is somehow different. One of the sequences are generated by matrix $\underline{\underline{A}}$, but the other is produced by the transpose of that matrix as $\underline{\underline{A}}^T$. Then the updating operations are done for the $\underline{\underline{A}}$-sequence and the$\underline{\underline{A}}^T$-sequences both to the same vectors. Normally, the convergence rate of the system will be doubled, but the convergence could be much more irregular, that the values for the corresponding errors may fluctuate. Another important fact for this method is that there are not any multiplications with the transpose of the coefficient matrix which means less number of operations.

CGS accelerates the convergence of the BiCG by generating residuals which are related to the original residual by the square of a polynomial in $\underline{\underline{A}}$, instead of a polynomial in $\underline{\underline{A}}$, as in the case of the CG and BiCG. In practice, this results in CGS converging roughly twice as fast as the BiCG. The additional advantage is that only the matrix $\underline{\underline{A}}$ is involved and not $\underline{\underline{A}}^T$. The computational cost for both the BiCG and CGS are about the same per iteration. CGS is applicable to nonsymmetrical matrices.

In CGS, the residual vector $\underline{r}^{(i)}$ can be regarded as the product of $\underline{r}^{(0)}$ and the

Pseudocode:

Compute $\underline{r}^{(0)} = \underline{b} - \underline{\underline{A}}\,\underline{x}^{(0)}$ for some initial guess $\underline{x}^{(0)}$
choose $\underline{\hat{r}}^{(0)}$ for example, $\underline{r}^{(0)} = \underline{\hat{r}}^{(0)}$
for $i = 1, 2, ...$
  solve $\underline{\underline{M}}\,\underline{z}^{(i-1)} = \underline{r}^{(i-1)}$
  solve $\underline{\underline{M^T}}\,\underline{\hat{z}}^{(i-1)} = \underline{\hat{r}}^{(i-1)}$
  $\rho_{i-1} = \underline{z}^{(i-1)^T}\underline{\hat{r}}^{(i-1)}$
  if $\rho_{i-1} = 0,$ method fails
  if $i = 1$
    $\underline{p}^{(1)} = \underline{z}^{(0)}$
    $\underline{\hat{p}}^{(1)} = \underline{\hat{z}}^{(0)}$
  else
    $\beta_{i-1} = \rho_{i-1}/\rho_{i-2}$
    $\underline{p}^{(i)} = \underline{z}^{(i-1)} + \beta_{i-1}\underline{p}^{(i-1)}$
    $\underline{\hat{p}}^{(i)} = \underline{\hat{z}}^{(i-1)} + \beta_{i-1}\underline{\hat{p}}^{(i-1)}$
  endif
  $\underline{q}^{(i)} = \underline{\underline{A}}\,\underline{p}^{(i)}$
  $\underline{\hat{q}}^{(i)} = \underline{\underline{A^T}}\,\underline{\hat{p}}^{(i)}$
  $\alpha_i = \rho_{i-1}/\underline{\hat{p}}^{(i)^T}\underline{q}^{(i)}$
  $\underline{x}^{(i)} = \underline{x}^{(i-1)} + \alpha_i\underline{p}^{(i)}$
  $\underline{r}^{(i)} = \underline{r}^{(i-1)} - \alpha_i\underline{q}^{(i)}$
  $\underline{\hat{r}}^{(i)} = \underline{\hat{r}}^{(i-1)} - \alpha_i\underline{\hat{q}}^{(i)}$
  check convergence; continue if necessary
end

Figure 4.2: Pseudocode of the Preconditioned BiConjugate Gradient Method

ith degree polynomial in $\underline{\underline{A}}$, that is;

$$\underline{r}^{(i)} = P_i(\underline{\underline{A}})\underline{r}^{(0)}. \tag{4.31}$$

This same polynomial satisfies $\hat{\underline{r}}^{(i)} = P_i(A^T)\hat{\underline{r}}^{(0)}$ so that

$$\rho_i = (\hat{\underline{r}}^{(i)}, \underline{r}^{(i)}) = (P_i(\underline{\underline{A}}^T)\hat{\underline{r}}^{(0)}, P_i(\underline{\underline{A}})\underline{r}^{(0)}) = (\hat{\underline{r}}^{(0)}, P_i^2(\underline{\underline{A}})\underline{r}^{(0)}) \tag{4.32}$$

This suggests that if $P_i(\underline{\underline{A}})$ reduces $\underline{r}^{(0)}$ to a smaller vector $\underline{r}^{(i)}$, then it might be advantageous to apply this "contraction" operator twice and compute $P_i^2(\underline{\underline{A}})\underline{r}^{(0)}$. By this way, it turns out to be easy to find the corresponding approximations for $\underline{x}$.

4.2.3.1 Convergence of CGS [36]

The convergence of this method is about as twice as for BiCG, which is in agreement with the observation that the same "contraction" operator if applied twice. However, there is no reason that the "contraction" operator, even if it really reduces the initial residual $\underline{r}^{(0)}$, it should also reduce the once reduced vector $\underline{r}^{(k)} = P_k(\underline{\underline{A}})\underline{r}^{(0)}$. This is evidenced by the often highly irregular convergence behavior of the method.

4.2.3.2 Implementation of CGS [36]

CGS requires about the same number of operations per iteration as BiCG, but does not involve computations with $\underline{\underline{A}}^T$ Hence, in circumstances where computation with $\underline{\underline{A}}^T$ is impractical, CGS may be attractive.

The pseudocode for the Preconditioned Conjugate Gradient Squared Method with preconditioner $\underline{\underline{M}}$, Jacobi Preconditioner, is given in Figure 4.3 ([36]).

4.2.4 BiConjugate Gradient Stabilized Method [36]

Bi-CGSTAB also generates two sequences, both of which are conjugate gradient sequences; One of the sequences are generated by matrix $\underline{\underline{A}}$, but the other

Pseudocode:

Compute $\underline{r}^{(0)} = \underline{b} - \underline{\underline{A}}\,\underline{x}^{(0)}$for some initial guess $\underline{x}^{(0)}$
choose $\hat{\underline{r}}^{(0)}$ for example, $\underline{r}^{(0)} = \hat{\underline{r}}^{(0)}$
for $i = 1, 2, ...$
  $\rho_{i-1} = \hat{\underline{r}}^T \underline{r}^{(i-1)}$
  if $\rho_{i-1} = 0,$ method fails
  if $i = 1$
    $\underline{u}^{(1)} = \underline{r}^{(0)}$
    $\underline{p}^{(1)} = \underline{u}^{(1)}$
  else
    $\beta_{i-1} = \rho_{i-1}/\rho_{i-2}$
    $\underline{u}^{(i)} = \underline{r}^{(i-1)} + \beta_{i-1}\underline{q}^{(i-1)}$
    $\underline{p}^{(i)} = \underline{u}^{(i)} + \beta_{i-1}(\underline{q}^{(i-1)} + \beta_{i-1}\underline{p}^{(i-1)})$
  endif
  solve $\underline{\underline{M}}\,\hat{\underline{p}} = \underline{p}^{(i)}$
  $\hat{\underline{\nu}} = \underline{\underline{A}}\,\hat{\underline{p}}$
  $\alpha_i = \rho_{i-1}/\hat{\underline{r}}^T\hat{\underline{\nu}}$
  $\underline{q}^{(i)} = \underline{u}^{(i)} - \alpha_i\hat{\underline{\nu}}$
  solve $\underline{\underline{M}}\,\hat{\underline{u}} = \underline{u}^{(i)} + \underline{q}^{(i)}$
  $\underline{x}^{(i)} = \underline{x}^{(i-1)} + \alpha_i\hat{\underline{u}}$
  $\hat{\underline{q}} = \underline{\underline{A}}\,\hat{\underline{u}}$
  $\underline{r}^{(i)} = \underline{r}^{(i-1)} - \alpha_i\hat{\underline{q}}$
  check convergence; continue if necessary
end

Figure 4.3: Pseudocode of the Preconditioned Conjugate Gradient Squared Method

is produced by the transpose of that matrix as $\underline{\underline{A}}^T$. Instead of orthogonalizing each sequence, they are made mutually orthogonal, or bi-orthogonal [36]. This method is effective when the coefficient matrix is nonsymmetrical and nonsingular. Usually smoother convergence is obtained when compared to CGS. The reason is that different updates for the $\underline{\underline{A}}^T$ are being used.

Bi-CGSTAB was developed to solve nonsymmetric linear systems while avoiding the often irregular convergence patterns of CGS and requires no transpose calculations. Instead of computing the CGS sequence $i \mapsto P_i^2(\underline{\underline{A}})\underline{r}^{(0)}$, Bi-CGSTAB computes i $i \mapsto Q_i(\underline{\underline{A}})P_i(\underline{\underline{A}})\underline{r}^{(0)}$ where Q_i is an ith degree polynomial describing a steepest descent update.

4.2.4.1 Convergence of Bi-CGSTAB [36]

The convergence behavior of this method cannot be compared with the other methods' easily, since it is sometimes faster, sometimes slower. However the exact point is that the convergence is smoother. Bi-CGSTAB can be interpreted as the product of BiCG and repeatedly applied general minimum residual method (GMRES) [36]. At least locally, a residual vector is minimized, which leads to a considerably smoother convergence behavior. Since the method is composed of BiCG method, there might have some breakdown situations occur at the conditions where BiCG diverges and these breakdown possibilities may be decreased by combining BiCG with other methods, i.e. by selecting other values for $\underline{w}_i$.(see the algorithm) [36].

Furthermore, Bi-CGSTAB has two stopping tests; if the method has already converged at the first test on the norm of s(s is a relation between the recent and preceding residual error vectors), then the subsequent update would be numerically tentative. Additionally, stopping on the first test saves a few unnecessary steps as well ([36], [38]).

4.2.4.2 Implementation of Bi-CGSTAB [36]

This method requires two matrix-vector products and four inner products, i.e., two inner products more than BiCG and CGS. The pseudocode for the preconditioned Bi-CGSTAB with preconditioner $\underline{\underline{M}}$ is given in Figure 4.4 ([36]).

4.2.5 Quasi - Minimal Residual Method [36]

QMR applies a least - squares solve and update to the biconjugate gradient residuals, thereby smoothing out the irregular convergence behavior of BiCG. QMR largely avoids the breakdown that can occur in BiCG.

The BiConjugate Gradient Method has a irregular convergence character and furthermore some breakdowns even may occur during computation. This method, QMR, has more developed algorithm so these problems are mostly overcome by QMR. The main idea behind this algorithm is to solve the reduced tridiagonal system in a least squares sense. Additionally, QMR uses look-ahead techniques to avoid breakdowns in the underlying Lanczos process, which makes it more robust than BiCG [36]. This method can also be applicable to nonsymmetrical matrices.

4.2.5.1 Convergence of QMR [36]

One of the two breakdown situations of the BiCG method is being recovered by this method. This method shows similar steps in each iteration with the BiCG method if BiCG converges for that iteration. If BiCG method temporarily diverges or stagnates, then the difference between these methods will appear that QMR may still further reduce the residual. However, although the convergence behavior of the method seems to be better, the computation cost is higher than BiCG that it requires the transpose matrix - vector product.

Pseudocode:

Compute $\underline{r}^{(0)} = \underline{b} - \underline{\underline{A}}\,\underline{x}^{(0)}$ for some initial guess $\underline{x}^{(0)}$
choose $\hat{\underline{r}}^{(0)}$ for example, $\underline{r}^{(0)} = \hat{\underline{r}}^{(0)}$
for $i = 1, 2, ...$
  $\rho_{i-1} = \hat{\underline{r}}^T \underline{r}^{(i-1)}$
  if $\rho_{i-1} = 0,$ method fails
  if $i = 1$
    $\underline{p}^{(1)} = \underline{r}^{(0)}$
  else
    $\beta_{i-1} = (\rho_{i-1}/\rho_{i-2})(\alpha_{i-1}/\omega_{i-1})$
    $\underline{p}^{(i)} = \underline{r}^{(i-1)} + \beta_{i-1}(\underline{p}^{(i-1)} - \omega_{i-1}\underline{\nu}^{(i-1)})$
  endif
  solve $\underline{\underline{M}}\,\hat{\underline{p}} = \underline{p}^{(i)}$
  $\underline{\nu}^{(i)} = \underline{\underline{A}}\,\hat{\underline{p}}$
  $\alpha_i = \rho_{i-1}/\hat{\underline{r}}^T \underline{\nu}^{(i)}$
  $\underline{s} = \underline{r}^{(i-1)} - \alpha_i \underline{\nu}^{(i)}$
  check norm of $\underline{s}$; if small enough: set $\underline{x}^{(i)} = \underline{x}^{(i-1)} + \alpha_i \hat{\underline{p}}$ and stop
  solve $\underline{\underline{M}}\,\hat{\underline{s}} = \underline{s}$
  $\underline{t} = \underline{\underline{A}}\,\hat{\underline{s}}$
  $\omega_i = \underline{t}^T \underline{s}/\underline{t}^T \underline{t}$
  $\underline{x}^{(i)} = \underline{x}^{(i-1)} + \alpha_i \hat{\underline{p}} + \omega_i \hat{\underline{s}}$
  $\underline{r}^{(i)} = \underline{s} - \omega_i \underline{t}$
  check convergence; continue if necessary
  for continuation it is necessary that $\omega_i \neq 0$
end

Figure 4.4: Pseudocode of the Preconditioned BiConjugate Gradient Stabilized Method

4.2.5.2 Implementation of QMR [36]

The pseudocode for the Preconditioned Quasi Minimal Residual Method with preconditioner $\underline{\underline{M}} = \underline{\underline{M_1}}\,\underline{\underline{M_2}}$ is given in Figure 4.5 ([36]). This algorithm follows the two term recurrence version without look ahead, presented by Freund and Nachtigal [39]. This version of QMR is simpler to implement than the full QMR method with look ahead, but it is susceptible to breakdown of the underlying Lanczos process. (Other implementational variations are whether to scale Lanczos vectors or not, or to use three term recurrences instead of coupled two term recurrences. Such decisions usually have implications for the stability and the efficiency of the algorithm.)

The Algorithm presented here is modified in a sense to include a relatively inexpensive recurrence relation for the computation of the residual vector. This requires a few extra vectors of storage and vector update operations per iteration, but it avoids expending a matrix vector product on the residual calculation. Also, the algorithm has been modified so that only two full preconditioning steps are required instead of three.

Computation of the residual is done for the convergence test. If one uses right (or post) preconditioning, that is $\underline{\underline{M_1}} = \underline{\underline{I}}$ then a cheap upper bound for $||\underline{r}^{(i)}||$ can be computed in each iteration, avoiding the recursions for $||\underline{r}^{(i)}||$. QMR has roughly the same problems with respect to vector and parallel implementation as BiCG. The scalar overhead per iteration is slightly more than for BiCG. In all cases where the slightly cheaper BiCG method converges irregularly (but fast enough), QMR may be preferred for stability reasons.

4.3 Summary

Summary of operation count per iteration for the iterative methods described up-to-now are given in Table 4.1. The vector summations are less and there is no inner product for the FBM. Also the modified version of FBM in this study

Pseudocode:

Compute $\underline{r}^{(0)} = \underline{b} - \underline{\underline{A}}\,\underline{x}^{(0)}$ for some initial guess $\underline{x}^{(0)}$
$\hat{\underline{\nu}}^{(1)} = \underline{r}^{(0)}$; **solve** $\underline{\underline{M_1}}\,\underline{y} = \hat{\underline{\nu}}^{(1)}$; $\rho_1 = \left\|\underline{y}\right\|_2$
Choose $\hat{\underline{\omega}}^{(1)} == \underline{r}^{(0)}$
solve $\underline{\underline{M_2^t}}\,\underline{z} = \hat{\underline{\omega}}^{(1)}$; $\xi_1 = \left\|\underline{z}\right\|_2$
$\gamma_0 = 1; \eta_0 = -1$
for $i = 1, 2, ...$
  if $\rho_i = 0$ or $\xi_i = 0$ **method fails**
  $\underline{\nu}^{(i)} = \hat{\underline{\nu}}^{(i)}/\rho_i$; $\underline{y} = \underline{y}/\rho_i$
  $\underline{\omega}^{(i)} = \hat{\underline{\omega}}^{(i)}/\xi_i$; $\underline{z} = \underline{z}/\xi_i$
  $\delta_i = \underline{z}^T\underline{y}$; **if** $\delta_i = 0$ **method fails**
  solve $\underline{\underline{M_2}}\,\hat{\underline{y}} = \underline{y}$
  solve ${\underline{\underline{M_1}}}^T\,\hat{\underline{z}} = \underline{z}$
  if $i = 1$
    $\underline{p}^{(1)} = \hat{\underline{y}}$; $\underline{q}^{(1)} = \hat{\underline{z}}$
  else
    $\underline{p}^{(i)} = \hat{\underline{y}} - (\xi_i\delta_i/\epsilon_{i-1})\underline{p}^{(i-1)}$
    $\underline{q}^{(i)} = \hat{\underline{z}} - (\rho_i\delta_i/\epsilon_{i-1})\underline{q}^{(i-1)}$
  endif
  $\hat{\underline{p}} = \underline{\underline{A}}\underline{p}^{(i)}$
  $\epsilon_i = {\underline{q}^{(i)}}^T\hat{\underline{p}}$; **if** $\epsilon_i = 0$ **method fails**
  $\beta_i = \epsilon_i/\delta_i$; **if** $\beta_i = 0$ **method fails**
  $\hat{\underline{\nu}}^{(i+1)} = \hat{\underline{p}} - \beta_i\hat{\underline{\nu}}^{(i)}$
  solve $\underline{\underline{M_1}}\,\underline{y} = \hat{\underline{\nu}}^{(i+1)}$
  $\rho_{i+1} = \left\|\underline{y}\right\|_2$
  $\hat{\underline{\omega}}^{(i+1)} = \underline{\underline{A}}^T\underline{q}^{(i)} - \beta_i\underline{\omega}^{(i)}$
  solve ${\underline{\underline{M_2}}}^T\,\underline{z} = \hat{\underline{\omega}}^{(i+1)}$
  $\xi_{i+1} = \left\|\underline{z}\right\|_2$
  $\theta_i = \rho_{i+1}/(\gamma_{i-1}|\beta_i|)$; $\gamma_i = 1/\sqrt{1+\theta_i^2}$; **if** $\gamma_i = 0$ **method fails**
  $\eta_i = -\eta_{i-1}\rho_i\gamma_i^2/(\beta_i\gamma_{i-1}^2)$
  if $i = 1$
    $\underline{d}^{(1)} = \eta_1\underline{p}^{(1)}$; $\underline{s}^{(1)} = \eta_1\hat{\underline{p}}$
  else
    $\underline{d}^{(i)} = \eta_i\underline{p}^{(i)} + (\theta_{i-1}\gamma_i)^2\underline{d}^{(i-1)}$
    $\underline{s}^{(i)} = \eta_i\hat{\underline{p}} + (\theta_{i-1}\gamma_i)^2\underline{s}^{(i-1)}$
  endif
    $\underline{x}^{(i)} = \underline{x}^{(i-1)} + \underline{d}^{(i)}$
    $\underline{r}^{(i)} = \underline{r}^{(i-1)} - \underline{s}^{(i)}$
  check convergence; continue if necessary
end

Table 4.1: Comparison of operations count at ith iteration of the iterative methods.

Method	**Inner Prod.**	**Vector Sum.**	**Matrix-Vector Prod.**
FBM	0	1	1
CG	2	3	1
BiCG	2	5	2
CGS	2	6	2
Bi-CGSTAB	4	6	2
QMR	2	$8 + 4^*$	2

*:Less for implementations that do not recursively update the residual

Table 4.2: Storage Requirements for the iterative methods.

Method	**Storage Requirement**
FBM	matrix $+2K$
CG	matrix $+6K$
BiCG	matrix $+10K$
CGS	matrix $+11K$
Bi-CGSTAB	matrix $+10K$
QMR	matrix $+16K^*$

*:Less for implementations that do not recursively update the residual.

requires additional K times 2×2 matrix inverse in each iteration, where K is the number of unknowns.

The storage requirements of the corresponding iterative methods are given in Table 4.2.

Chapter 5

Simulations and Results

The main motivation of this study is to accelerate the conventional MoM solution (which is $O(N^3)$) for the electromagnetic wave scattering from dielectric random rough surfaces by using iterative algorithms (which is $O(N^2)$). However, various iterative algorithms (stationary and nonstationary) work differently and their convergence rates change depending upon the roughness of the surface, shape of the surface, etc. All these issues are discussed in a detailed fashion in this chapter.

First, the accuracy of the MoM for coupled integral equations and the iterative methods considered in this thesis namely FBM (as a stationary iterative method), and CGS, Bi-CGSTAB and QMR (as nonstationary iterative methods) for scattering from various dielectric random rough surfaces are verified by comparing them with the previously published results. Then, the efficiency and convergence properties of the iterative methods are discussed by applying them to various dielectric random rough surfaces, i.e., Gaussian and exponentially correlated random rough surfaces. It has been observed that if both stationary (FBM) and nonstationary (CGS, Bi-CGSTAB, QMR) methods converge, then FBM is more efficient (i.e. its convergence rate is much faster). However, there are cases where FBM fail to converge such as some exponentially correlated random rough surfaces and/or re-entrant surfaces. In such cases, the nonstationary methods are accurate, though their convergence rate may be relatively low. Such results

validate the superiority of the nonstationary algorithms over FBM (stationary ones). It should be noted that in general convergence properties of the iterative algorithms are discussed in terms of the monostatic and bistatic non-coherent radar cross section (NRCS), which are described in Chapter 3. It should be mentioned that monostatic NRCS is also referred to as backscattering coefficient, and bistatic NRCS is also referred to as scattering coefficient.

5.1 Validation of the Algorithms

In order to assess the accuracy of our formulas as well as the accuracy of our computer codes, we compare our results with the results of Iodice given in [24].

In all results, surface NRCS is computed by a Monte Carlo simulation. Basically, a large number of independent sample profiles, N_s, with prescribed statistics, are generated. Then the fields scattered by different surfaces are evaluated using MoM. Finally they are subsequently averaged to compute the NRCS via

$$\sigma^0 = \frac{2\pi r}{N_s L_{eff}} \left[\sum_{i=1}^{N_s} |E_i^s|^2 - \frac{1}{N_s} \Big| \sum_{i=1}^{N_s} E_i^s \Big|^2 \right] \tag{5.1}$$

for HH polarization and

$$\sigma^0 = \frac{2\pi r}{N_s L_{eff}} \left[\sum_{i=1}^{N_s} |H_i^s|^2 - \frac{1}{N_s} \Big| \sum_{i=1}^{N_s} H_i^s \Big|^2 \right] \tag{5.2}$$

for VV polarization. In the following examples, the number of independent sample profiles is set to 160, so that the error in the estimate of σ^0 is smaller than 1 dB with probability 0.997 [24]. The profiles are moderately rough surface for Figures 5.1(a)-5.4(a) and very rough surface for Figures 5.1(b)-5.4(b). The width of the rectangular basis functions is $\lambda/10$. The length of the surface is 15m and the frequency is chosen to be 1 GHz, where $\lambda = 0.3$m.

Figure 5.1 shows the comparison of the monostatic NRCS results of this study generated by MoM with that of given in [24] (again calculated by MoM) for moderately and very rough surface with $\epsilon_r = 4$ for HH polarization at 1 GHz. In

Figure 5.1a, σ is set to $\lambda/6$ and rms slope is set to 13° (i.e. moderately rough surface). In Figure 5.1b, σ is set to 0.707λ and rms slope is set to 45° (i.e. very rough surface). In both figures angle of incidence is increased from 0° to 60° with 10° steps. As seen in the figures, monostatic NRCS decreases as the incident angle increases (especially for a moderately rough profile), since the power of reflected wave to the initial point decreases. We see an excellent agreement in the results as seen in Figure 5.1, and the difference between the results is not more than 1 dB for all of the cases.

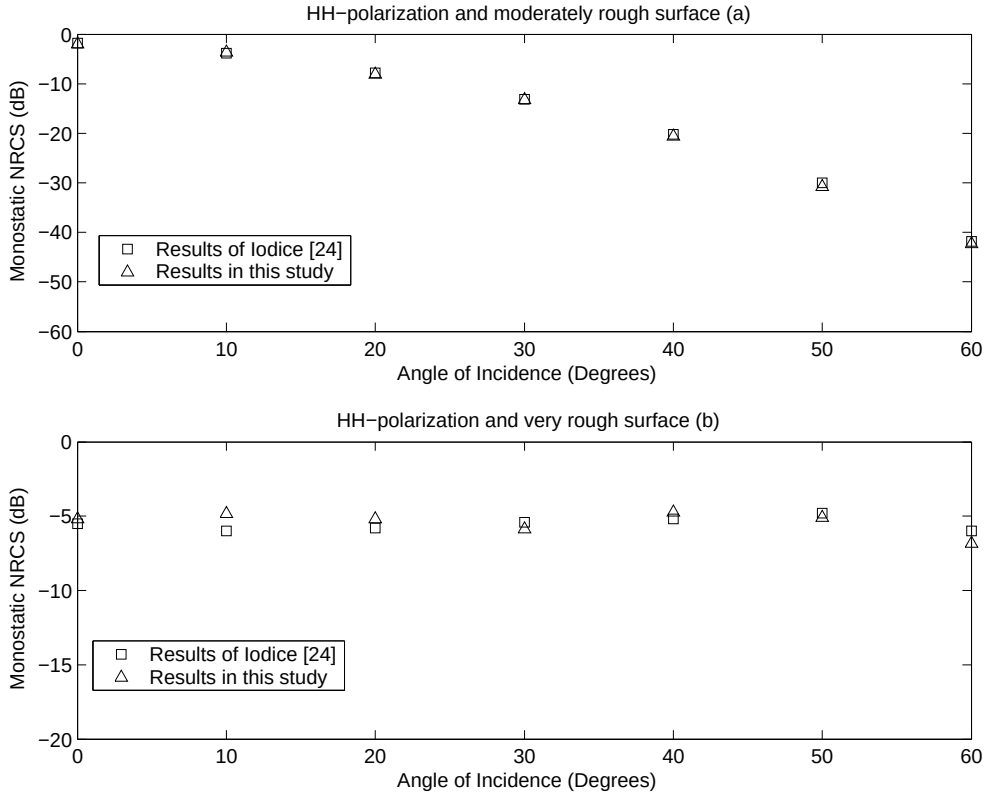

Figure 5.1: Comparison of the monostatic NRCS values from [24] for various angles of incidence with the results obtained in this study for a dielectric constant, $\epsilon_r = 4$ for HH polarization at 1 GHz. (a)$\sigma = \lambda/6$, rms slope= 13° (i.e. moderately rough surface). (b)$\sigma = 0.707\lambda$, rms slope= 45° (i.e. very rough surface).

Figure 5.2 shows a similar comparison of the monostatic NRCS results generated by MoM in this study with that of given in [24] for $\epsilon_r = 15 - j4$ (i.e. moist

soil) again for HH polarization at 1 GHz. Similar to Figure 5.1, in Figure 5.2a, σ is set to $\lambda/6$ and rms slope is set to 13° (i.e. moderately rough surface) and in Figure 5.2b, σ is set to 0.707λ and rms slope is set to 45° (i.e. very rough surface). In both figures angle of incidence is increased from 0° to 60° with 10° steps. Since the conductivity of the surface increases, the NRCS values also increases that the reflection of the electromagnetic waves from the surface is higher. In Figure 5.2,

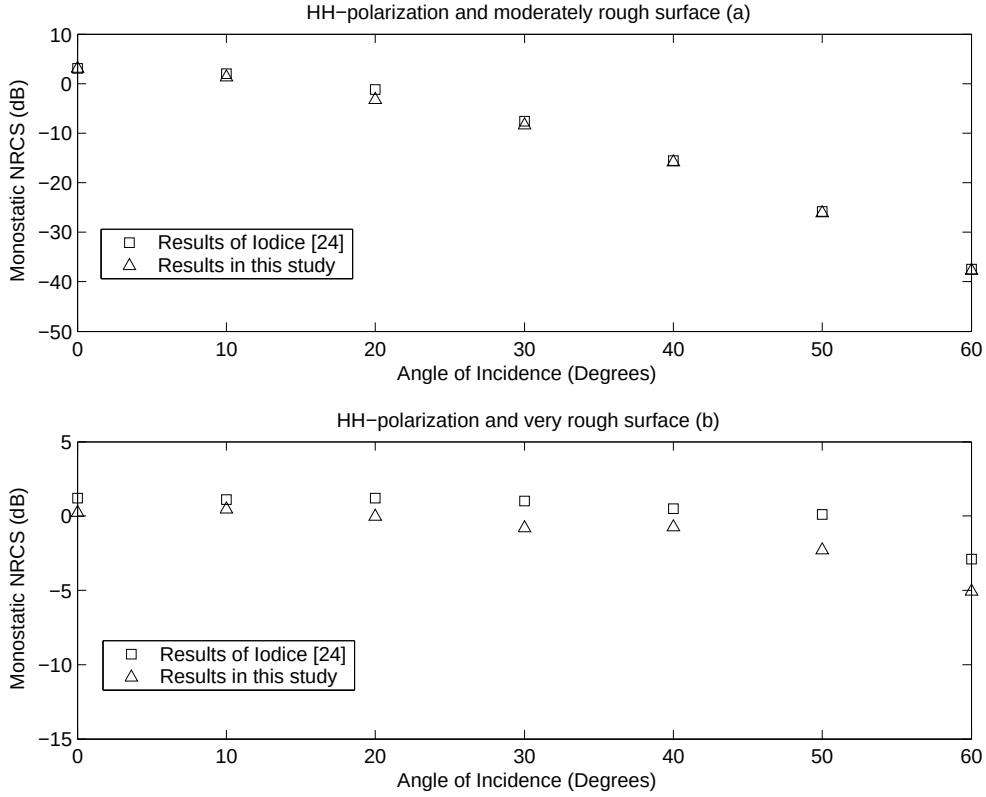

Figure 5.2: Comparison of the monostatic NRCS values from [24] for various angles of incidence with the results obtained in this study for a dielectric constant, $\epsilon_r = 15 - j4$ for HH polarization at 1 GHz. (a)$\sigma = \lambda/6$, rms slope= 13° (i.e. moderately rough surface). (b)$\sigma = 0.707\lambda$, rms slope= 45° (i.e. very rough surface).

again there is a good agreement and the difference between the results is not more than 1 dB for most of the cases. However, at the the points where the

angle of incidence is 50° and 60° for a very rough surface, the differences between the NRCS values are approximately 2.2 dB and 2 dB, respectively. Since the estimated error for such profiles is approximately 1 dB, the 2 dB difference between the results presented in [24] and the results presented in this thesis is acceptable. Furthermore, there are some inconsistencies in the results given in [24] (mentioned at the end of this subsection), which might be another reason for the aforementioned difference in the monostatic NRCS values.

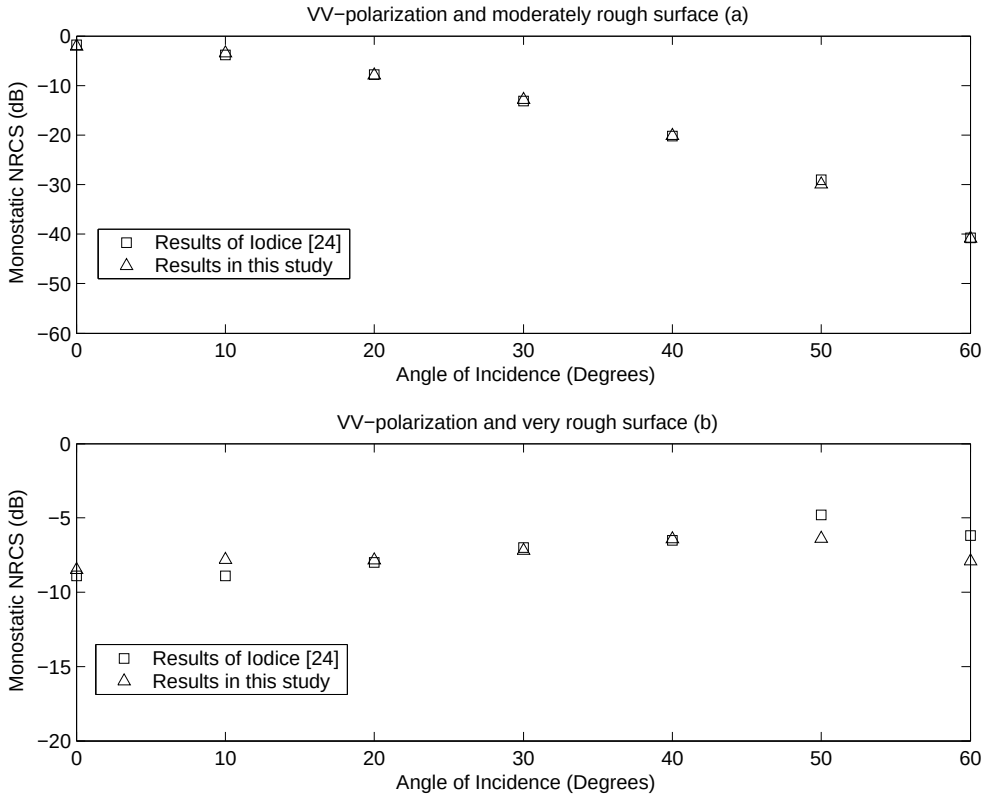

Figure 5.3: Comparison of the monostatic NRCS values from [24] for various angles of incidence with the results obtained in this study for a dielectric constant, $\epsilon_r = 4$ for VV polarization at 1 GHz. (a)$\sigma = \lambda/6$, rms slope= 13° (i.e. moderately rough surface). (b)$\sigma = 0.707\lambda$, rms slope= 45° (i.e. very rough surface).

Figure 5.3 shows a similar comparison of the monostatic NRCS results generated by MoM in this study with that of given in [24] for $\epsilon_r = 4$ (i.e. dry soil) for VV polarization at 1 GHz. Similar to Figure 5.2, in Figure 5.3a, σ is set to

$\lambda/6$ and rms slope is set to 13° (i.e. moderately rough surface) and in Figure 5.2b, σ is set to 0.707λ and rms slope is set to 45° (i.e. very rough surface). In both figures angle of incidence is increased from 0° to 60° with 10° steps. When we compare the data for each incident angle, the difference between the results is not more than 1 dB for all of the cases except the point at an incident angle of 60° for a very rough surface where the difference is 1.7 dB. Since the estimated error is 2dB in the comparison, we have an excellent agreement.

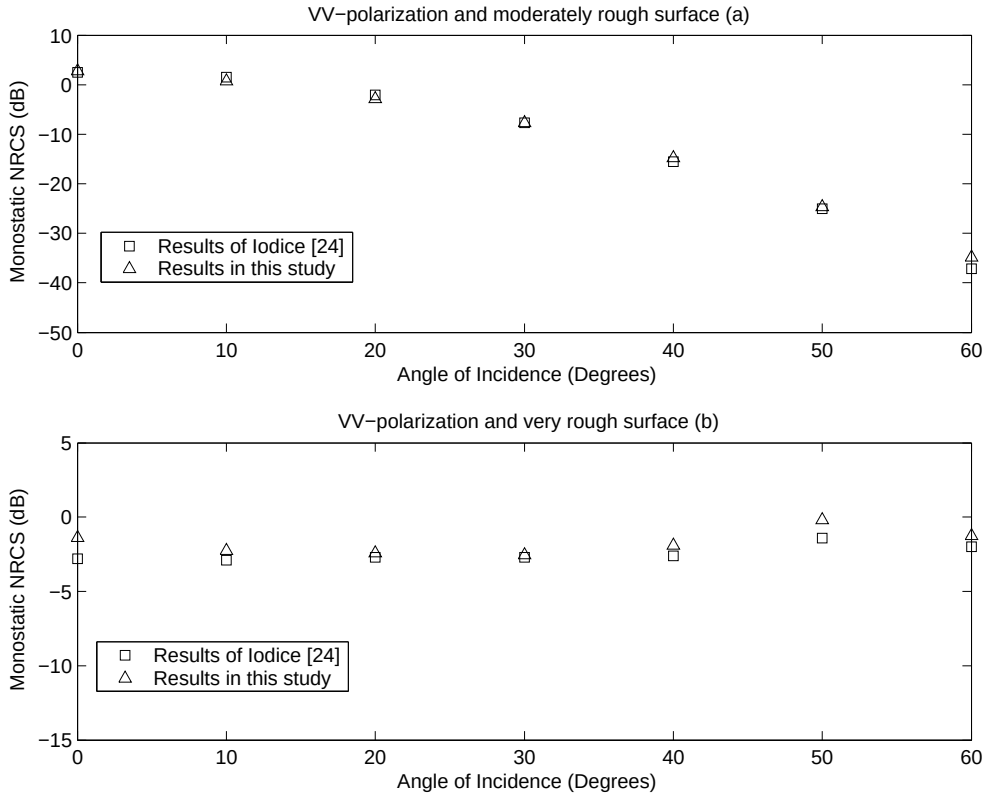

Figure 5.4: Comparison of the monostatic NRCS values from [24] for various angles of incidence with the results obtained in this study for a dielectric constant, $\epsilon_r = 15 - j4$ for VV polarization at 1 GHz. (a)$\sigma = \lambda/6$, rms slope= 13° (i.e. moderately rough surface). (b)$\sigma = 0.707\lambda$, rms slope= 45° (i.e. very rough surface).

Figure 5.4 shows a similar comparison of the the monostatic NRCS results generated by MoM in this study with that of given in [24] for $\epsilon_r = 15 - j4$ (i.e.

moist soil) for VV polarization at 1 GHz. Similar to Figure 5.3, in Figure 5.4a, σ is set to $\lambda/6$ and rms slope is set to 13° (i.e. moderately rough surface) and in Figure 5.2b, σ is set to 0.707λ and rms slope is set to 45° (i.e. very rough surface). In both figures angle of incidence is increased from 0° to 60° with 10° steps. Since the conductivity of the surface increases, the NRCS values also increases independent from the properties of the surface profile. In Figure 5.4, there is a perfect agreement and the difference between the NRCS values is not more than 1 dB for any of the angles of incidence.

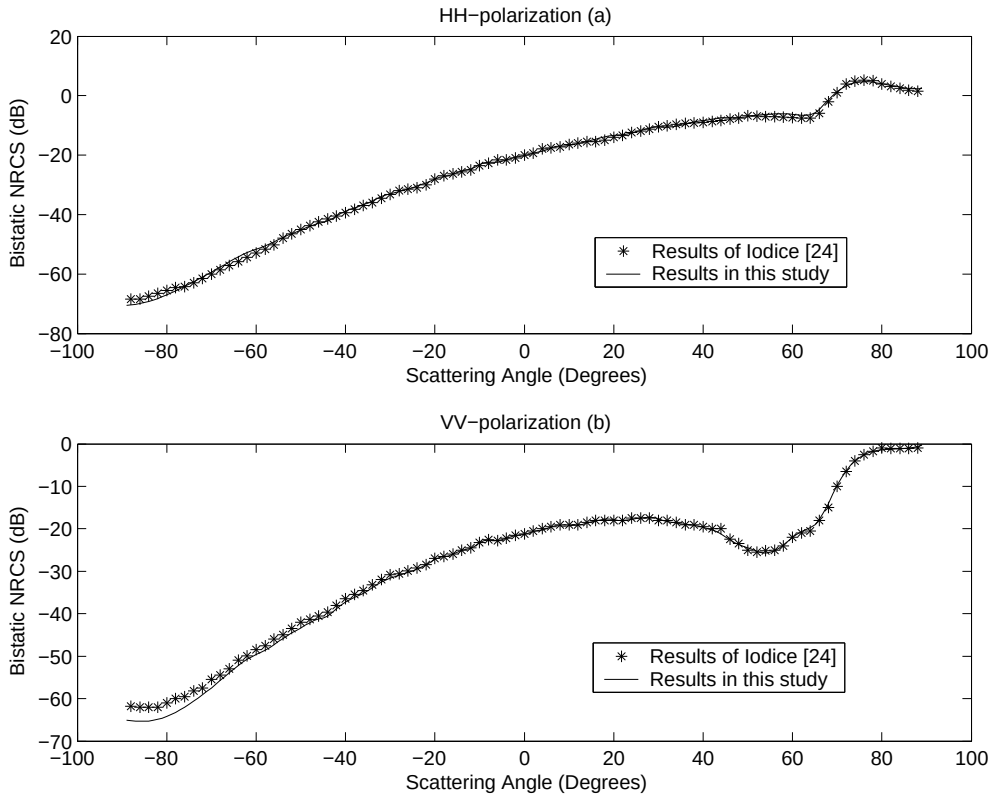

Figure 5.5: Comparison of the bistatic NRCS values from [24] for Gaussian correlated rough profile with the results obtained in this study for a dielectric constant, $\epsilon_r = 4$ at 1 GHz and $\sigma = \lambda/6$, rms slope= 13° (i.e. moderately rough surface) (Angle of incidence is 75°). (a) HH Polarization (b)VV Polarization

Figure 5.5 depicts the comparison of the bistatic results given in [24] (obtained by MoM) with the results obtained in this study by MoM for a Gaussian correlated

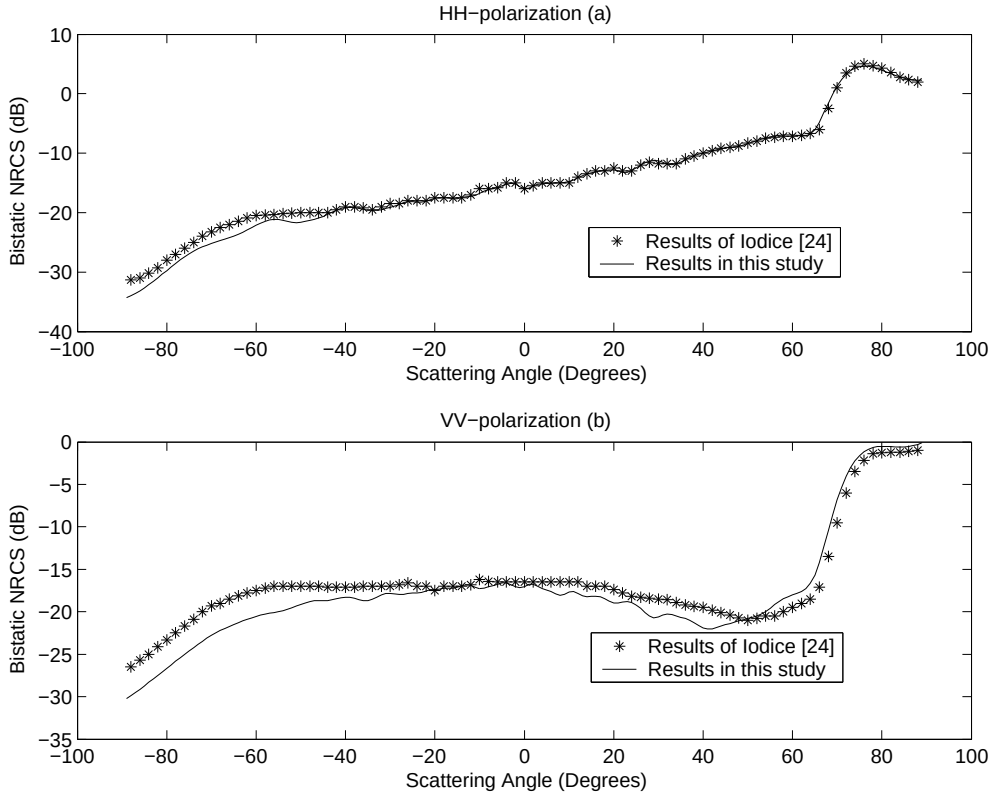

Figure 5.6: Comparison of the bistatic NRCS values from [24] for exponentially correlated rough profile with the ones we have derived for a dielectric constant, $\epsilon_r = 4$ at 1 GHz and $\sigma = \lambda/6$, rms slope= 13°. (Angle of incidence is 75°) (a) HH Polarization (b)VV Polarization

random rough profile with $\sigma = \lambda/6$ and rms slope= 13° (i.e. moderately rough surface) at 1 GHz when the angle of incidence is set to 75°. In Figure 5.5a, HH polarization case and in Figure 5.5b, VV polarization case are given. Bistatic NRCS is calculated by scanning all the scattering angles for each sample profile and then by (using Equation (5.2)) plotting the corresponding NRCS value versus scattering angle. There is again a perfect agreement for the bistatic NRCS values between the results given in [24] with the ones obtained in this study such that the error is not more than 1dB for almost all of the scattering angles.

Figure 5.6 depicts the comparison of the bistatic results derived in [24] by MoM with the results obtained in this study by MoM for an exponentially correlated

random rough profile with $\sigma = \lambda/6$ and rms slope= 13° (i.e. moderately rough surface) at 1 GHz when the angle of incidence is set to 75°. In Figure 5.5a, HH polarization case and in Figure 5.5b, VV polarization case is given. There is also a good agreement for most of the bistatic NRCS values between the results given in [24] with the ones obtained in this study. The error is more than 1dB (nominally 3dB) at angles around the backscattering angle. Normally, the error may be higher for exponentially correlated rough surfaces, since the surface profile of the exponentially correlated surface is not as smooth as Gaussian correlated surface. The slope calculated at the points where the integral is taken approaches to 1.5 for exponential case, where it is maximum 0.5 for Gaussian case for the moderately rough profile where $\sigma = \lambda/6$ and rms slope is 13°.

Note that, to assess the accuracy of our results and thereby to validate the algorithms used in this thesis, we compared our monostatic and bistatic NRCS results with those given in [24]. However, a careful investigation of Figure 7 and Figure 9 of [24] reveals the following accuracy problem in [24]. For the case of exponentially correlated rough profile, the monostatic NRCS value at 75° for HH polarization is approximately -29 dB. However, in Figure 9, the bistatic NRCS value for HH polarization (incident angle is set to 75°) at $-75°$, which corresponds to the monostatic NRCS value at 75°, is approximately 26 dB. As seen from these plots, the difference is at least 3 dB. Although such a difference can be attributed to the unstable nature of the exponentially correlated rough surface, we have not observed such a behavior in our results. Consequently, we believe that our results are more accurate.

5.2 Application of the Iterative Methods

Up to now, we have compared our results with the ones given in [24] and observed excellent agreement. Now we focus on the accuracy and efficiency of the iterative algorithms. In the following figures (i.e. Figures 5.7-5.10), we show the same monostatic NRCS results of Section 5.1 obtained by using FBM, Bi-CGSTAB, QMR and CGS. The results are also compared with the conventional MoM results.

As seen in all figures, there is an excellent agreement.

In order to quantitatively measure the agreement between the iterative methods and "numerically exact" results, their root mean square error, Δ, defined as

$$\Delta = \sqrt{\frac{\sum_{p=1}^{P}\left[\sigma^o_{dB,ITER}(\vartheta_p) - \sigma^o_{dB,MoM}(\vartheta_p)\right]^2}{P}} \tag{5.3}$$

is used, where P is the number of considered incident angles. In all of the cases considered in Figures 5.7-5.10, Δ is smaller than 0.05dB, which show the accuracy of the stopping criterion and the good estimates of the surface NRCS by iterative algorithms.

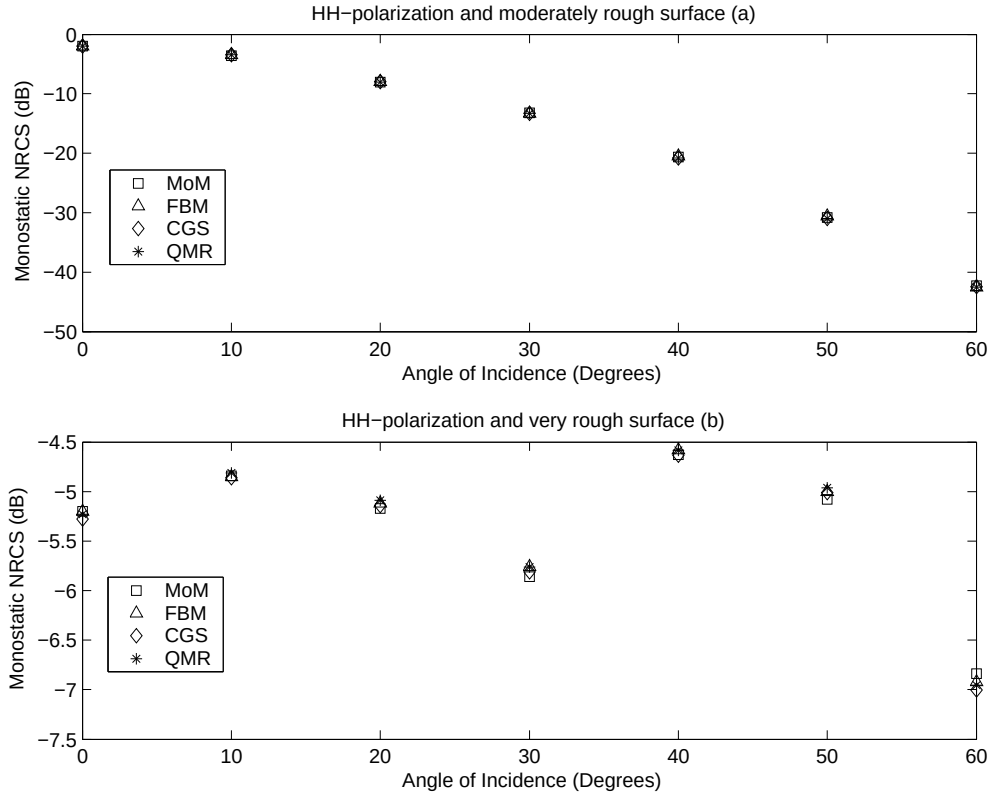

Figure 5.7: Comparison of the monostatic NRCS values for different iterative methods for Gaussian correlated rough profile with a dielectric constant, $\epsilon_r = 4$ for HH polarization at 1 GHz. (a)$\sigma = \lambda/6$, rms slope= 13°. (b)$\sigma = 0.707\lambda$, rms slope= 45°.

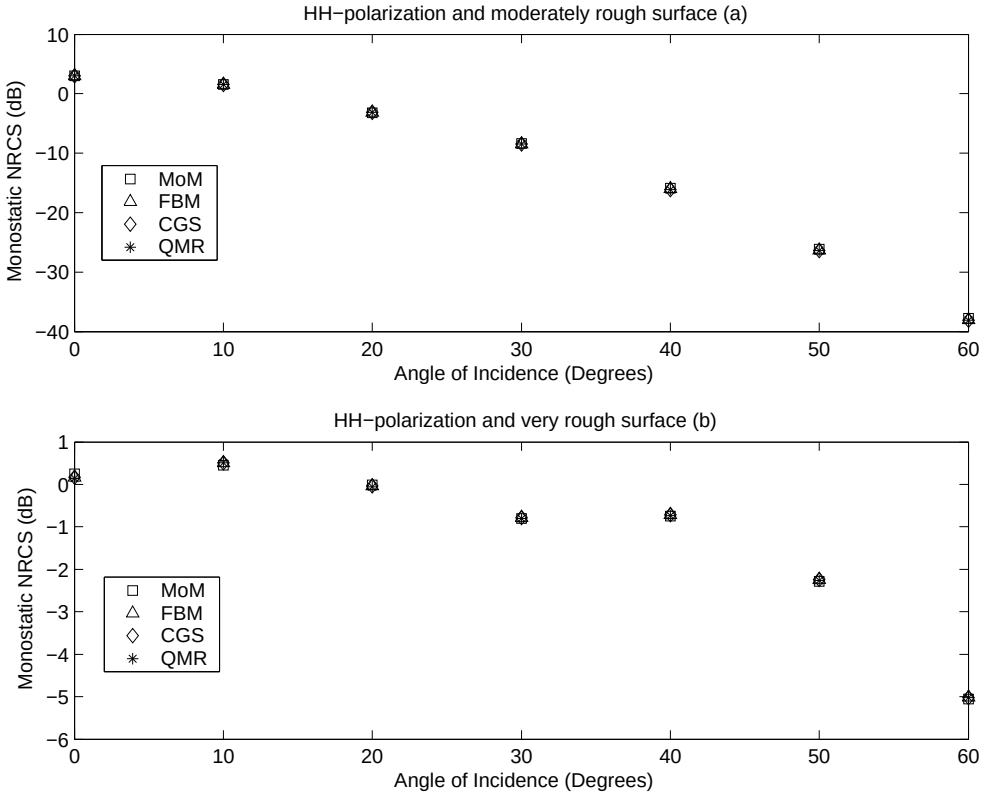

Figure 5.8: Comparison of the monostatic NRCS values for different iterative methods for Gaussian correlated rough profile with a dielectric constant, $\epsilon_r = 15 - j4$ for HH polarization at 1 GHz. (a)$\sigma = \lambda/6$, rms slope= 13°. (b)$\sigma = 0.707\lambda$, rms slope= 45°.

Furthermore, we can analyze the convergence rates of the iterative methods for various surface profiles. In the following tables (i.e. Tables 5.1-5.4), we mentioned the number of iterations, n_0, required for each iterative method to converge until an error of $r(n_0) < 10^{-2}$ is satisfied for different values of standard deviation (σ) and correlation length (L_c) for HH and VV polarization cases. For all of the following tables, incident angle is set to 60°. On the other hand, "nc" means that there is no convergence for at least one out of ten realizations. However, for the cases where nonstationary algorithms cannot converge, the error calculated cannot decrease below the estimated value, it fluctuates around $0.1 - 2$, but for the case of FBM (stationary iterative method), if there is no convergence, then

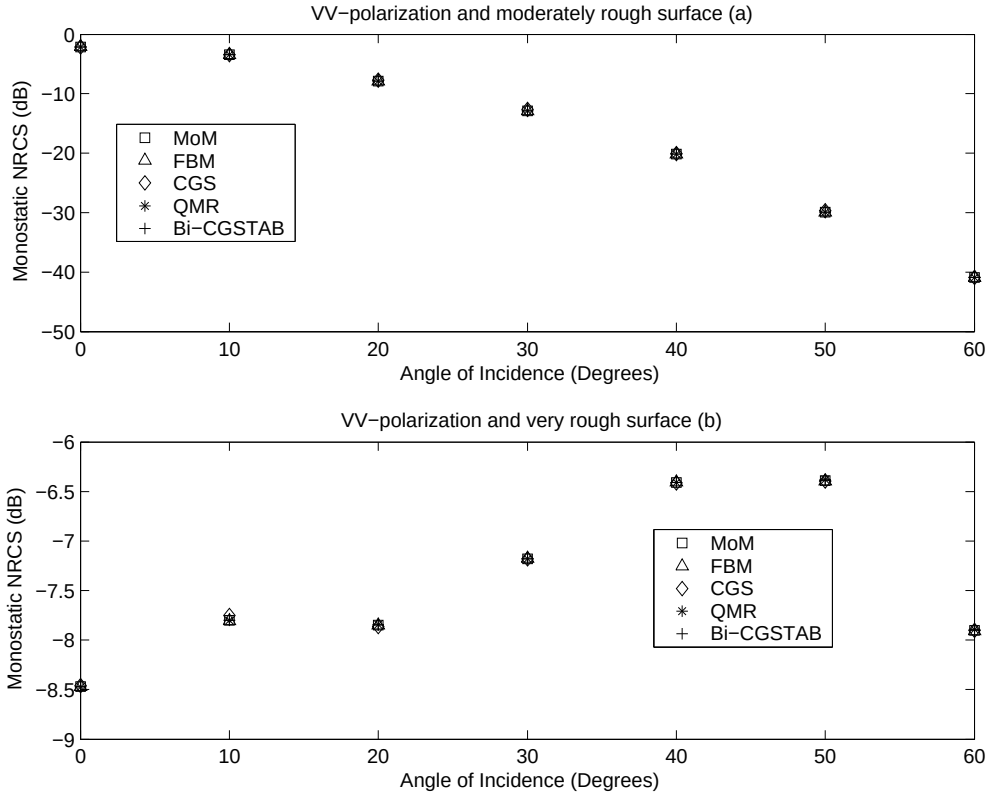

Figure 5.9: Comparison of the monostatic NRCS values for different iterative methods for Gaussian correlated rough profile with a dielectric constant, $\epsilon_r = 4$ for VV polarization at 1 GHz. (a)$\sigma = \lambda/6$, rms slope= 13°. (b)$\sigma = 0.707\lambda$, rms slope= 45°.

the error diverges.

In the tables the σ/λ ratio defines the the surface roughness. As this ratio increases the roughness of the surface also increases. On the other hand, the σ/L_c ratio defines the correlation between the surface samples. As this ratio increases, the correlation length decreases. Although the roughness of the surface remains unchanged, the smooth behavior of the surface profile diminishes. Interestingly, in the tables it is shown that Bi-CGSTAB cannot converge at least one out of ten realizations for HH polarization case, since the diagonal elements in matrix equation are not dominant even smaller when compared to non-diagonal elements. Thus, Bi-CGSTAB is marked as "nc" for all of those cases in Tables 5.1-5.4. More

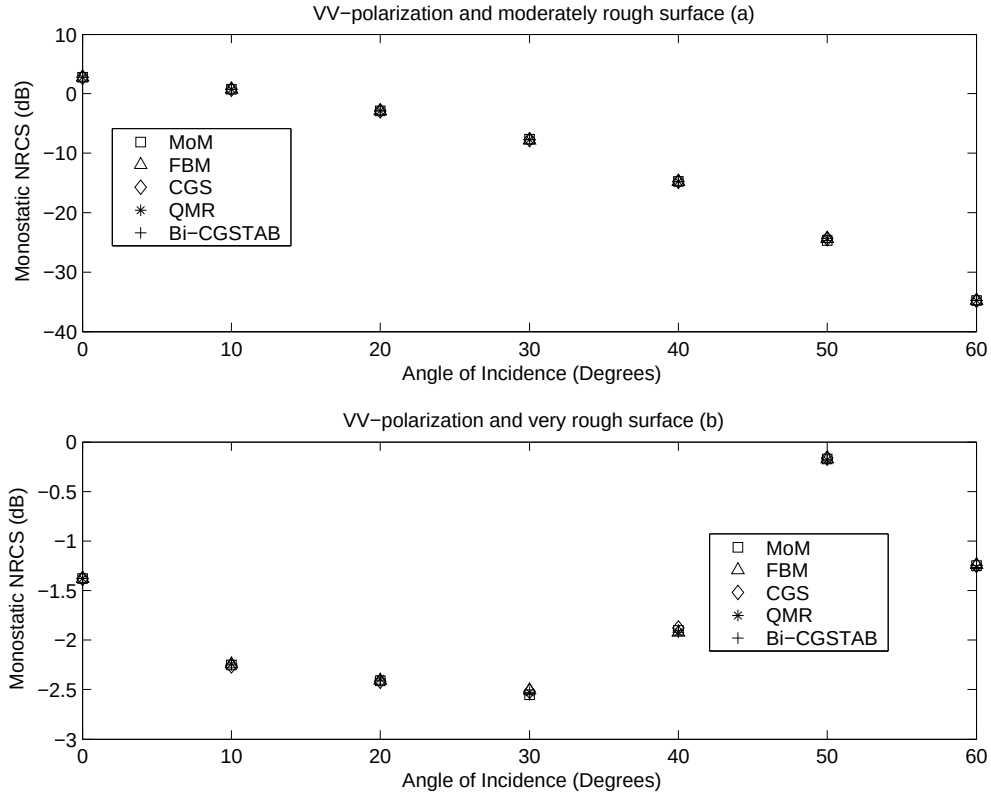

Figure 5.10: Comparison of the monostatic NRCS values for different iterative methods for Gaussian correlated rough profile with a dielectric constant, $\epsilon_r = 15 - j4$ for VV polarization at 1 GHz. (a)$\sigma = \lambda/6$, rms slope= 13°. (b)$\sigma = 0.707\lambda$, rms slope= 45°.

information about this point is given in Section 5.2.2.

In the first table, Table 5.1, the surface autocorrelation function is chosen to be Gaussian and the relative dielectric constant is, $\epsilon_r = 4$. Since the surface is smooth and the dielectric permittivity is small, the convergence rates of the all of the algorithms are high.

In the Table 5.2, the surface autocorrelation function is chosen to be exponential and the relative dielectric constant is still, $\epsilon_r = 4$. Since the surface is not as smooth as Gaussian correlated rough profile, the convergence rates of all of the algorithms are not as high as Gaussian correlated profile, even there are

Table 5.1: Average minimum number of iterations n_0 such that $r(n_0) < 10^{-2}$ is satisfied for different values of standard deviation (σ) and correlation length (L_c), and for VV and HH polarization. Angle of incidence=60°. Surface autocorrelation function: Gaussian. Relative Dielectric Constant: $\epsilon_r = 4$

Iterative Method	σ/λ σ/L_c	0.1 VV-HH	0.3 VV-HH	0.5 VV-HH	0.7 VV-HH	1.0 VV-HH	10.0 VV-HH
FBM	0.15	3-4	3-5	4-5	4-5	4-5	4-5
	0.20	4-4	4-5	4-5	4-5	4-5	4-5
	0.33	5-5	4-5	4-5	4-5	4-5	4-5
	0.71	5-5	4-5	4-5	4-5	4-5	4-5
	1.00	6-7	5-7	5-7	6-7	4-6	5-5
CGS	0.15	29-31	28-29	27-28	26-31	25-25	25-29
	0.20	32-35	33-32	27-28	23-30	21-29	22-32
	0.33	31-33	36-36	28-36	24-32	22-28	23-29
	0.71	33-31	39-42	28-41	26-33	23-33	24-31
	1.00	33-34	42-50	30-47	26-42	23-35	24-33
Bi-CGSTAB	0.15	24-nc	21-nc	30-nc	26-nc	19-nc	14-nc
	0.20	29-nc	32-nc	34-nc	28-nc	22-nc	19-nc
	0.33	35-nc	48-nc	38-nc	41-nc	27-nc	21-nc
	0.71	41-nc	61-nc	42-nc	43-nc	32-nc	25-nc
	1.00	45-nc	78-nc	58-nc	48-nc	41-nc	27-nc
QMR	0.15	43-46	46-42	43-42	41-41	44-39	43-53
	0.20	47-40	53-37	48-41	47-40	46-36	45-48
	0.33	51-46	62-43	51-67	48-48	46-43	45-51
	0.71	58-56	71-49	59-71	55-56	51-48	46-47
	1.00	69-65	80-64	67-84	69-62	57-68	48-50

some cases where the methods cannot converge. Naturally, number of iterations needed to converge for nonstationary iterative methods is higher than FBM, but there are also some cases where FBM cannot converge but nonstationary ones can.

In the Table 5.3, the surface autocorrelation function is chosen to be Gaussian and the relative dielectric constant is, $\epsilon_r = 15 - j4$. Although we have increased the conductivity, the methods still converge for both cases.

Table 5.2: Average minimum number of iterations n_0 such that $r(n_0) < 10^{-2}$ is satisfied for different values of standard deviation (σ) and correlation length (L_c), and for VV and HH polarization. Angle of incidence=60°. Surface autocorrelation function: Exponential. Relative Dielectric Constant: $\epsilon_r = 4$

Iterative Method	σ/λ σ/L_c	0.1 VV-HH	0.3 VV-HH	0.5 VV-HH	0.7 VV-HH	1.0 VV-HH	10.0 VV-HH
FBM	0.15	5-5	5-6	7-7	7-8	6-6	nc-nc
	0.20	5-5	6-7	8-7	8-7	nc-nc	nc-nc
	0.33	5-5	7-7	9-14	9-nc	nc-nc	nc-nc
	0.71	5-6	13-nc	nc-nc	nc-nc	nc-nc	nc-nc
	1.00	5-8	nc-nc	nc-nc	nc-nc	nc-nc	nc-nc
CGS	0.15	24-24	22-26	21-34	25-37	31-48	nc-nc
	0.20	26-25	28-39	32-44	31-42	36-51	nc-nc
	0.33	30-31	34-45	43-51	41-50	43-56	nc-nc
	0.71	31-33	42-45	51-69	57-nc	nc-nc	nc-nc
	1.00	35-32	55-nc	68-nc	82-nc	nc-nc	nc-nc
Bi-CGSTAB	0.15	28-nc	36-nc	43-nc	58-nc	63-nc	nc-nc
	0.20	30-nc	42-nc	51-nc	69-nc	68-nc	nc-nc
	0.33	31-nc	63-nc	86-nc	82-nc	nc-nc	nc-nc
	0.71	37-nc	nc-nc	nc-nc	nc-nc	nc-nc	nc-nc
	1.00	43-nc	nc-nc	nc-nc	nc-nc	nc-nc	nc-nc
QMR	0.15	43-41	48-52	51-68	62-80	72-99	nc-nc
	0.20	45-45	63-69	64-86	73-100	78-132	nc-nc
	0.33	45-47	76-78	76-81	85-95	106-nc	nc-nc
	0.71	49-47	85-88	104-96	128-nc	nc-nc	nc-nc
	1.00	53-51	101-nc	127-nc	nc-nc	nc-nc	nc-nc

In the Table 5.4, the surface autocorrelation function is chosen to be exponential and the relative dielectric constant is still, $\epsilon_r = 15 - j4$. Since the surface is not as smooth as Gaussian correlated rough profile, the convergence rates of all of the algorithms decreases, furthermore as the roughness increases and/or correlation decreases, methods start not to converge. However, it is obvious that, the nonstationary methods still converge for most of the cases, where FBM fails.

If we investigate Tables 5.1-5.4, one can immediately figure out that, all of the iterative methods converge very fast for VV polarization and for any reasonable roughness. However, for large σ/λ and large σ/L_c ratio, especially for exponential

Table 5.3: Average minimum number of iterations n_0 such that $r(n_0) < 10^{-2}$ is satisfied for different values of standard deviation (σ) and correlation length (L_c), and for VV and HH polarization. Angle of incidence=60°. Surface autocorrelation function: Gaussian. Relative Dielectric Constant: $\epsilon_r = 15 - j4$

Iterative Method	σ/λ σ/L_c	0.1 VV-HH	0.3 VV-HH	0.5 VV-HH	0.7 VV-HH	1.0 VV-HH	10.0 VV-HH
FBM	0.15	3-4	3-4	3-4	3-4	3-4	3-4
	0.20	3-4	3-5	3-4	3-4	3-4	3-4
	0.33	3-4	3-5	3-4	3-4	3-4	3-4
	0.71	4-4	6-6	4-5	3-4	4-3	3-4
	1.00	4-4	6-11	4-5	3-4	4-3	3-4
CGS	0.15	9-24	8-25	9-23	9-23	9-24	7-27
	0.20	11-23	11-28	12-25	13-24	11-22	8-21
	0.33	13-21	14-33	16-31	16-27	13-25	8-24
	0.71	15-30	17-36	19-35	19-27	18-25	10-22
	1.00	15-36	24-48	24-38	22-29	19-26	11-22
Bi-CGSTAB	0.15	10-nc	12-nc	12-nc	11-nc	12-nc	10-nc
	0.20	14-nc	21-nc	22-nc	14-nc	16-nc	11-nc
	0.33	17-nc	23-nc	32-nc	18-nc	19-nc	14-nc
	0.71	21-nc	32-nc	48-nc	25-nc	25-nc	17-nc
	1.00	30-nc	46-nc	62-nc	28-nc	31-nc	19-nc
QMR	0.15	19-33	19-35	18-34	17-36	18-34	16-46
	0.20	21-33	24-38	22-39	28-38	24-36	17-41
	0.33	23-35	29-41	27-44	32-41	29-38	18-33
	0.71	29-47	36-48	39-46	38-42	32-39	21-35
	1.00	30-57	47-64	46-59	42-46	36-46	21-34

autocorrelation, FBM may fail to converge. At most of those profiles where FBM fails, QMR and CGS can converge which indicates QMR and CGS may also be useful in rough surface scattering problems. By using nonstationary algorithms, one can easily handle the problem of scattering from most of the rough surface profiles more than FBM does. It is obvious that the number of iterations required for nonstationary algorithms is higher, but if the number of matrix elements increases, i.e., electrically large surfaces, often the nonstationary methods converge in similar number of iterations given in Tables 5.1-5.4.

Table 5.4: Average minimum number of iterations n_0 such that $r(n_0) < 10^{-2}$ is satisfied for different values of standard deviation (σ) and correlation length (L_c), and for VV and HH polarization. Angle of incidence=60°. Surface autocorrelation function: Exponential. Relative Dielectric Constant: $\epsilon_r = 15 - j4$

Iterative Method	σ/λ σ/L_c	0.1 VV-HH	0.3 VV-HH	0.5 VV-HH	0.7 VV-HH	1.0 VV-HH	10.0 VV-HH
FBM	0.15	4-4	4-5	4-5	4-4	6-6	nc-nc
	0.20	4-5	4-5	5-6	10-10	nc-nc	nc-nc
	0.33	4-5	5-5	7-8	nc-nc	nc-nc	nc-nc
	0.71	6-6	nc-nc	nc-nc	nc-nc	nc-nc	nc-nc
	1.00	6-6	nc-nc	nc-nc	nc-nc	nc-nc	nc-nc
CGS	0.15	12-25	13-27	19-28	17-26	19-34	nc-nc
	0.20	13-23	16-30	19-31	17-33	23-43	nc-nc
	0.33	13-22	21-33	22-33	27-45	31-49	nc-nc
	0.71	15-24	23-33	32-45	42-49	41-55	nc-nc
	1.00	14-26	24-36	52-51	nc-nc	nc-nc	nc-nc
Bi-CGSTAB	0.15	17-nc	17-nc	21-nc	20-nc	33-nc	nc-nc
	0.20	18-nc	22-nc	31-nc	26-nc	42-nc	nc-nc
	0.33	21-nc	27-nc	37-nc	47-nc	56-nc	nc-nc
	0.71	23-nc	39-nc	56-nc	102-nc	nc-nc	nc-nc
	1.00	24-nc	56-nc	nc-nc	nc-nc	nc-nc	nc-nc
QMR	0.15	23-33	28-36	32-38	35-56	38-49	nc-nc
	0.20	25-36	28-42	34-44	37-59	43-43	nc-nc
	0.33	25-34	31-48	40-54	41-78	54-65	nc-nc
	0.71	26-38	42-60	54-58	74-88	96-98	nc-nc
	1.00	27-40	45-79	72-78	nc-nc	nc-nc	nc-nc

5.2.1 Superiority of the Nonstationary Algorithms

Although the convergence of FBM is extremely fast for moderately rough dielectric surfaces, it may fail to converge as the roughness increases as we discussed previously and can be seen from Tables 5.1-5.4.

Another surface profile, where FBM cannot converge is re-entrant profiles. For re-entrant profiles, the order of the current elements is being changed, which disturbs the diagonally dominant nature of the matrix in turn, affects the convergence capability of the method. However for these kinds of surfaces, still the

nonstationary algorithms converge.

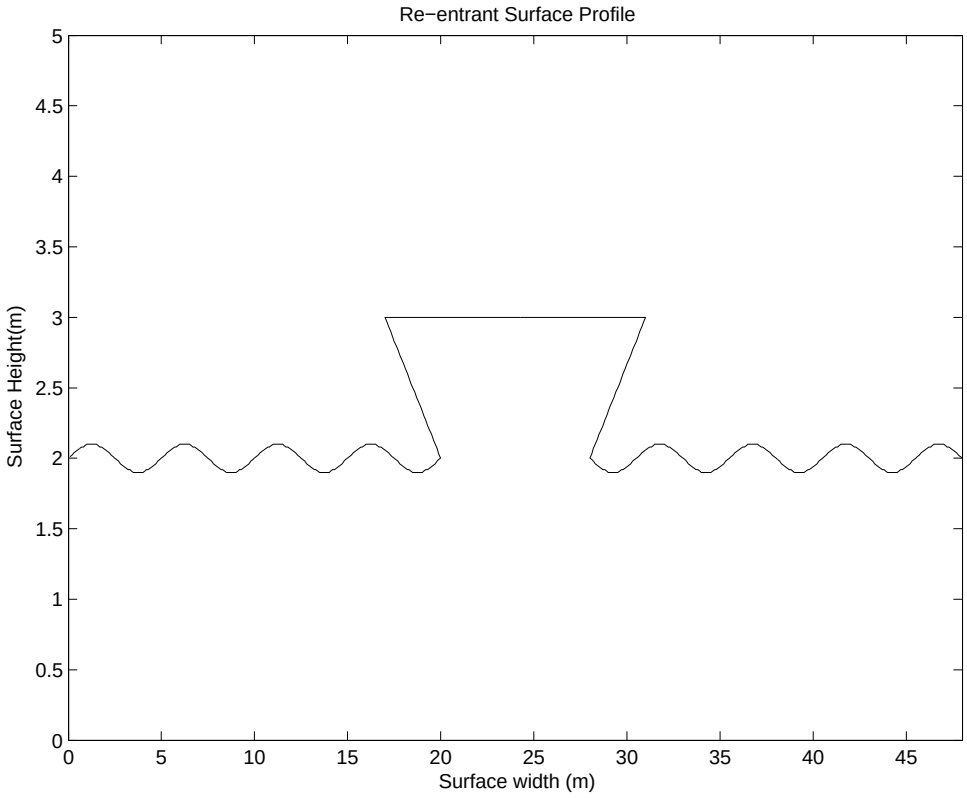

Figure 5.11: Dielectric re-entrant surface profile

In fact for the dielectric boundary, there is no current induced on the surface. However, we can assume that there is a current induced on the surface from the matrix equation derived in Sections 3.1 and 3.2 (the unknown coefficients composed of coefficients of the current elements and total electric field for each matching point) and this current forms the scattered field. In Figure 5.11, there is a symmetrical dielectric re-entrant profile with a relative dielectric constant, $\epsilon_r = 15 - j4$. In Figure 5.12, the current distribution over the re-entrant profile of Figure 5.11, evaluated by MoM, at 300 MHz is given. Such a distribution is reasonable in a sense that the current decreases nearly to zero for the cases where there is almost no illumination. Furthermore the current distribution is also symmetrical with respect to the surface profile.

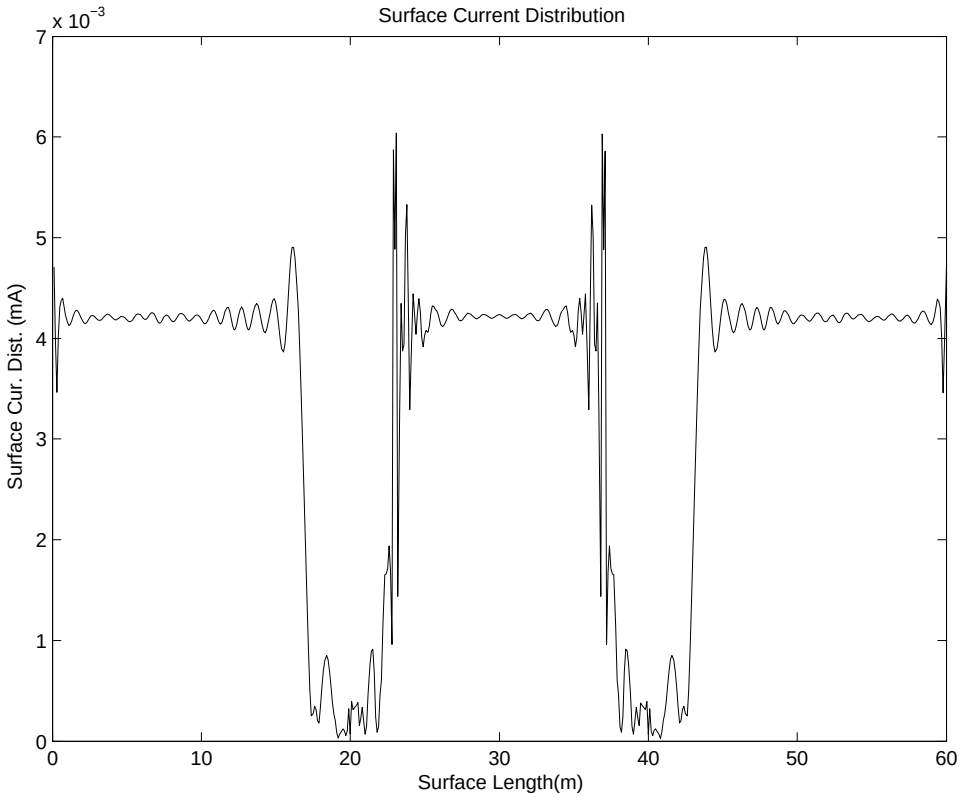

Figure 5.12: Surface current distribution induced on the re-entrant profile given in Figure 5.11 and calculated by direct application of MoM for HH polarization. Frequency is 300MHz. Relative Dielectric Constant, $\epsilon_r = 15 - j4$ (conductivity, $\sigma = 0.0668 S/m$). The width, Δx, of the rectangular basis functions is set to $\lambda/10$.

On the other hand, we investigated the same dielectric re-entrant problem by using the iterative methods. The convergence rate of each considered iterative method in terms of the number of iterations is given in Table 5.5.

From Table 5.5, CGS and QMR converges below a predetermined error criterion for all incident angles, and Bi-CGSTAB converges at only 0°. As the angle of incidence increases, (i.e., incident angle approaches to grazing angle), the diagonal elements get smaller which results the increase in the number of iterations for convergence as expected.

Table 5.5: Number of iterations n_0 such that $r(n_0) < 0.02$ is satisfied for different angles of incidence for dielectric re-entrant surface given in Figure 5.11. Relative Dielectric Constant: $\epsilon_r = 15 - j4$. Frequency is 300 MHz.

Incident Angle (Degrees)	Iterative Method			
	CGS	QMR	Bi-CGSTAB	FBM
0	25	27	76	nc
10	58	73	nc	nc
20	46	65	nc	nc
30	67	66	nc	nc
40	52	72	nc	nc
50	66	96	nc	nc
60	68	89	nc	nc
70	69	106	nc	nc

In Figure 5.13, we see the current distribution for the angle of incidence ranging from 0°-30° and in Figure 5.14, we see the current distribution for angles of incidence ranging from 40°-70°. As shown in the figures, it is impossible to distinguish the current distributions obtained via MoM and the two nonstationary iterative methods (namely CGS and QMR) for all cases.

Furthermore on dielectric re-entrant surfaces, in Figure 5.15, comparison of the monostatic NRCS values of CGS and QMR with the "numerically exact" solution (conventional MoM) is given. For all of the incident angles both QMR and CGS converges accurately and the root mean square difference defined in (5.3) is smaller than 0.1dB for both algorithms.

For the case of dielectric re-entrant surfaces, the superiority of the CGS and QMR is obvious. This important example shows the necessity of these nonstationary algorithms even though their convergence capability is worse when compared to FBM for the cases where FBM converges.

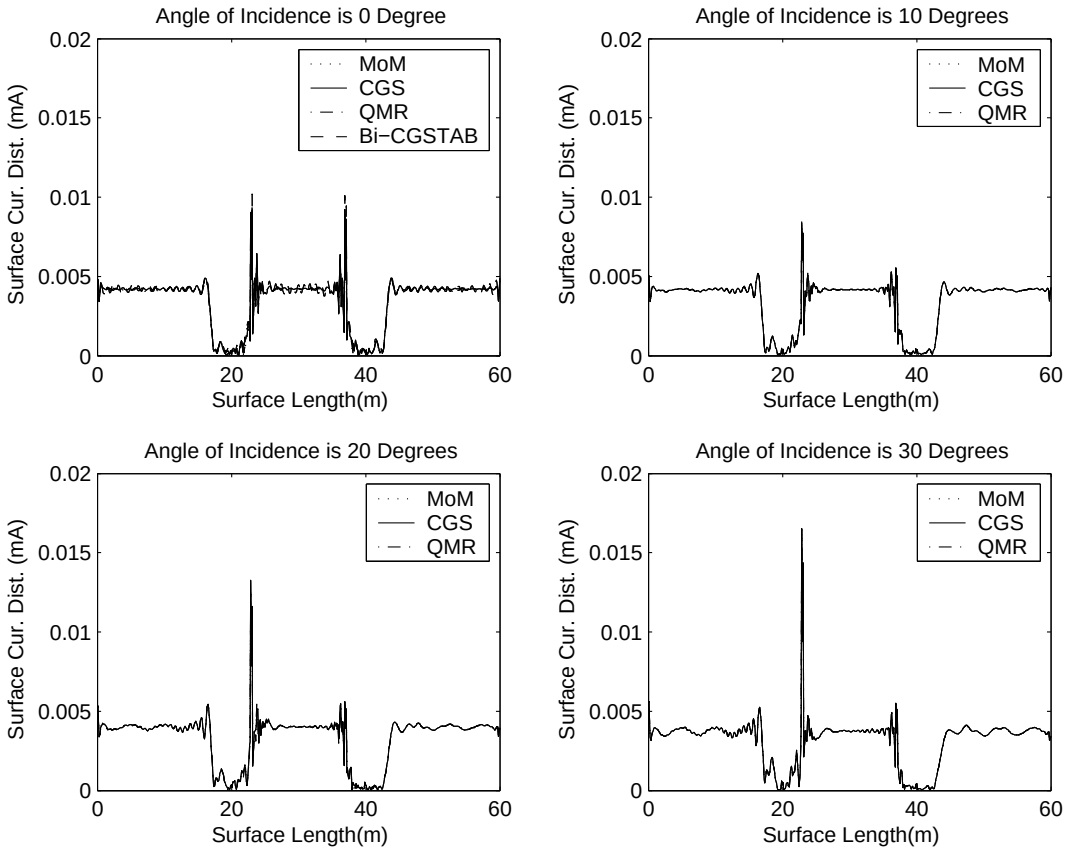

Figure 5.13: Comparison of the magnitude of current distribution for angles of incidence 0°-30° calculated by MoM, CGS and QMR for the re-entrant surface profile given in Figure 5.11. Frequency is 300 MHz. Relative Dielectric Constant, $\epsilon_r = 15 - j4$.

5.2.2 Important Remarks

As seen from tables 5.1-5.4, Bi-CGSTAB method cannot converge for HH polarization for all the cases. This is reasonable in a sense that the matrix equation, which is $2Nx2N$ and nonsymmetrical, is difficult to solve for HH polarization case. Moreover, the diagonal elements are not dominant enough, when compared to the non-diagonal terms. In fact, the method converges for most of the cases for HH polarization, but if it fails to convergence at least one out of ten realizations then it is expressed as "nc" which shows that there is always one profile that

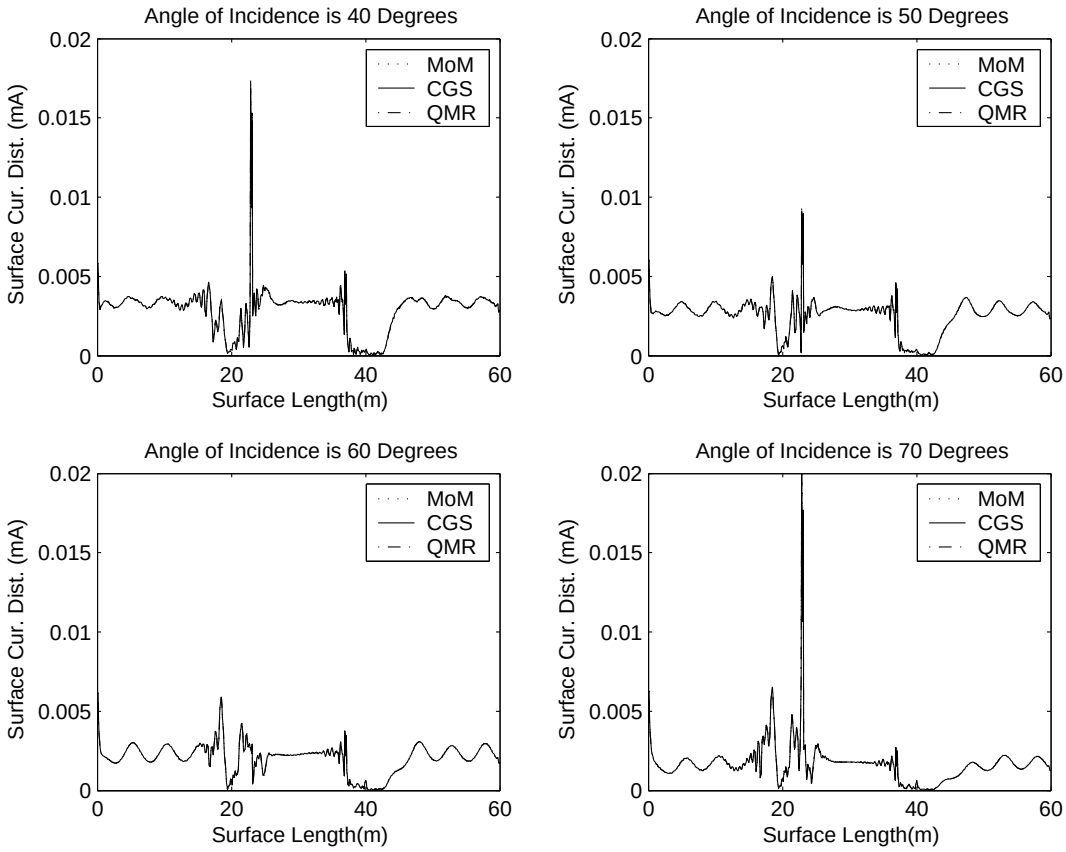

Figure 5.14: Comparison of the magnitude of current distribution for angles of incidence 40°-70° calculated by MoM, CGS and QMR for the re-entrant surface profile given in Figure 5.11. Frequency is 300 MHz. Relative Dielectric Constant, $\epsilon_r = 15 - j4$.

the method fails to converge. However for VV polarization, the diagonal terms dominate. This results in an increase in the convergence rate. Consequently, Bi-CGSTAB converges better, even faster than the other nonstationary methods.

Note that as the conductivity increases, the argument of the Hankel function will never be close to zero. Therefore, the small argument approximation of the Hankel function performed for the evaluation of Z_{1mn} when $m = n$ will not be valid. As a result, the Hankel function itself, even its large argument approximation can safely be used.

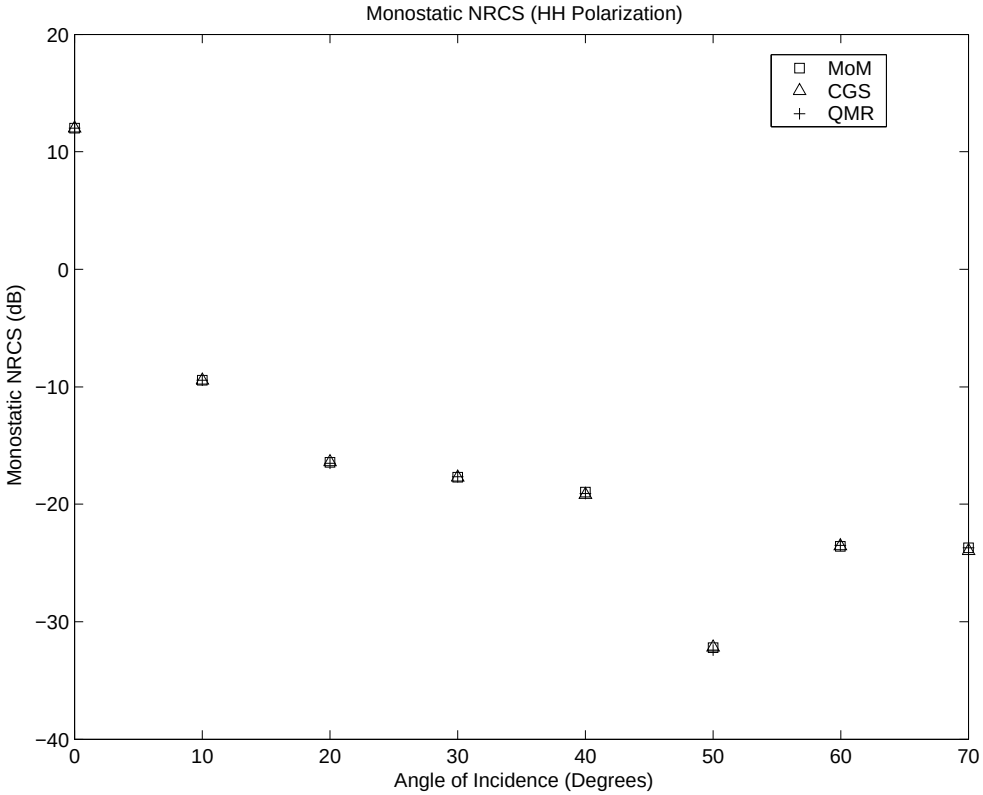

Figure 5.15: Comparison of Monostatic NRCS calculated by MoM, CGS and QMR for the re-entrant surface profile given in Figure 5.11. Frequency is 300 MHz. Relative Dielectric Constant, $\epsilon_r = 15 - j4$.

Finally, as the conductivity increases, special case is required in the selection of the size of the rectangular pulse basis functions for the MoM solution of the integral equation pairs (both HH and VV polarizations). In general (for dielectric cases) $\lambda/10$ as the size of the rectangular pulse basis functions yields fairly accurate results. However, this number should be decreased to $\lambda/20$ ($\lambda/30$) when the conductivity increases. This is, however, not valid for the PEC or impedance boundary condition (IBC) cases, where there is a single surface integral equation for those cases.

Chapter 6

Conclusions

Throughout this thesis, the electromagnetic wave scattering from random rough dielectric surfaces is investigated.

First, the corresponding surface integral equations are derived from the Maxwell's equations by using the surface equivalence theorems. Also Gaussian random rough surfaces with Gaussian and exponential correlation functions are generated. The conventional MoM solution of these integral equations for the generated dielectric random rough surfaces is called the "numerically exact" solution. Then, the same integral equations are solved via stationary (FBM) and nonstationary (CGS, Bi-CGSTAB, QMR) methods, thereby, the $O(N^3)$ computational cost is reduced to $O(N^2)$. Finally, the accuracy and the efficiency, as well as the convergence properties of those iterative methods are investigated for various surface profiles, and discussed in detail via the help of several numerical examples. Below are several important remarks which we concluded:

- FBM is a stationary iterative method and it converges very fast for moderately rough dielectric surfaces. However, it cannot convergence as the roughness and/or the dielectric constant increases. Furthermore, the investigation of re-entrant surfaces (eg; a broken wave in the ocean or a ship in the sea) cannot be achieved by using FBM.

- CGS is a nonstationary iterative method and it converges faster than the other nonstationary algorithms investigated in this thesis for the generated dielectric random rough surfaces. Its convergence is closer to FBM for moderately rough surfaces and it still converges for very rough exponentially correlated surfaces where FBM often cannot. Since this method is applicable to nonsymmetrical and non-diagonally dominant systems, it also converges for re-entrant surfaces.

- QMR is the other nonstationary iterative method and it shows a similar convergence behavior like CGS. However, it is slower for the surface profiles investigated in this thesis. This method is also applicable to re-entrant surfaces, but again the convergence is slower in terms of iteration number compared to CGS.

- Bi-CGSTAB is the last nonstationary iterative technique inspected. It cannot converge for HH polarization case, since the matrix formed for HH polarization is neither diagonally dominant nor symmetrical also has a worse condition number when compared to VV polarization case. This leads to irregular convergence behavior for Bi-CGSTAB that the method sometimes converges sometimes not. This method is more suitable for PEC or impedance surfaces where the matrix formed is symmetrical. On the other hand, the method cannot converge for the dielectric re-entrant surfaces with low dielectric permittivities.

- All of the methods lead to an error of maximum 0.2dB (nominally 0.05dB) compared to the conventional MoM solution when the monostatic and bistatic NRCS values are considered.

- When the surface correlation function is exponential, FBM cannot converge for most of the cases and the nonstationary algorithms cannot convergence for higher σ/λ and/or σ/L_c. This can be explained by recalling that a Gaussian autocorrelation profile looks smoother than an exponential autocorrelation profile with the same σ and L_c parameters. As the smooth behavior of the surface decreases, the convergence probabilities of the iterative methods also decrease.

6.1 Some Interesting Future Directions

Beyond this thesis, there are plenty of further studies that can be done on electromagnetic wave scattering from random rough dielectric surfaces.

- Similar problem can be investigated for three dimensional surfaces, which will give a deeper understanding on scattering. However, the solution process will be slower since the number of unknowns will increase enormously.
- Spectral acceleration (SA) technique can be applied to the forward-backward method, which solves the integral equations in a few iterations for moderately rough surfaces. By this way, electrically large terrain profiles can be simulated, since the computational cost decreases to $O(N)$ after the application of SA.
- Spectral acceleration algorithm can be applied in order to reduce the computational cost to $O(N)$ to the nonstationary algorithms as well, which are also capable of solving more rough exponentially or Gaussian correlated random surfaces, even re-entrant surface profiles.
- Other kinds of dielectric surface profiles can be studied, i.e., fractal surfaces, etc.
- Electromagnetic scattering by partially buried objects (cylinders, spheres, etc.) at the interface of dielectric random rough surfaces can be investigated.

Appendix A

Detailed Derivations of the Matrix Elements

A.1 HH Polarization

•

$$S_{0mn} = \frac{1}{2}\delta_{mn} + \int_{\Delta l_n} (\hat{n}' \cdot \nabla\phi_0) dl'. \quad (A.1)$$

If $m = n$, then

$$S_{0mn} = \frac{1}{2} + \int_{\Delta l_n} (\hat{n}' \cdot \nabla\phi_0) dl'. \quad (A.2)$$

By using the following equalities

$$\phi_{0,1}(\mathbf{r}_m, \mathbf{r}_n) = -\frac{j}{4} H_0^{(2)}(k_{0,1}|\mathbf{r}_m - \mathbf{r}_n|) \quad (A.3)$$

$$\nabla\phi_{0,1}(\mathbf{r}_m, \mathbf{r}_n) = \mathbf{R} \cdot \frac{jk_{0,1}}{4} H_1^{(2)}(k_{0,1}|\mathbf{r}_m - \mathbf{r}_n|) \quad (A.4)$$

where $\mathbf{R}$ is the unit vector in the direction of $(\mathbf{r}_m - \mathbf{r}_n)$, i.e., $\mathbf{R} = (\mathbf{r}_m - \mathbf{r}_n)/|\mathbf{r}_m - \mathbf{r}_n|$, with $\mathbf{r}_m$ and $\mathbf{r}_n$ representing position vectors from the origin to the surface points at x_m, observation point, and x_n, source point, respectively and

$$dl' \approx \sqrt{dz^2 + dx^2} = dx\sqrt{1 + (dz/dx)^2} = \Delta x\sqrt{1 + (dz/dx)^2}. \quad (A.5)$$

Then,

$$S_{0mn} = \frac{1}{2} + (\hat{n}_n \cdot \mathbf{R})\frac{jk_0}{4} H_1^{(2)}(k_0|\mathbf{r}_n - \mathbf{r}_m|)\Delta x\sqrt{1 + (dz/dx)^2}. \quad \text{(A.6)}$$

Furthermore, we know from [27] or [40]

$$H_p^{(2)}(k_{0,1}|\mathbf{r}_m - \mathbf{r}_n|) = J_p^{(2)}(k_{0,1}|\mathbf{r}_m - \mathbf{r}_n|) - jY_p^{(2)}(k_{0,1}|\mathbf{r}_m - \mathbf{r}_n|) \quad \text{(A.7)}$$

where p is the order of the Hankel function and

$$\lim_{|\mathbf{r}_m - \mathbf{r}_n| \to 0} H_1^{(2)}(k_{0,1}|\mathbf{r}_m - \mathbf{r}_n|) \approx \left[\frac{j}{\pi}\left(\frac{2}{k_{0,1}|\mathbf{r}_m - \mathbf{r}_n|}\right)\right]. \quad \text{(A.8)}$$

Also, as seen in Figure A.1, since $m = n$,

$$(\hat{n}_n \cdot \mathbf{R}) = \hat{n}_n \cdot \frac{(\mathbf{r}_m - \mathbf{r}_n)}{|\mathbf{r}_m - \mathbf{r}_n|} = \cos(\frac{\pi}{2} + \frac{\Delta\theta}{2}) = -\sin\frac{\Delta\theta}{2} \approx -\frac{\Delta\theta}{2} \quad \text{(A.9)}$$

and R_c is the radius of curvature and $R_c = |\mathbf{r}_m - \mathbf{r}_n|/\Delta\theta$.

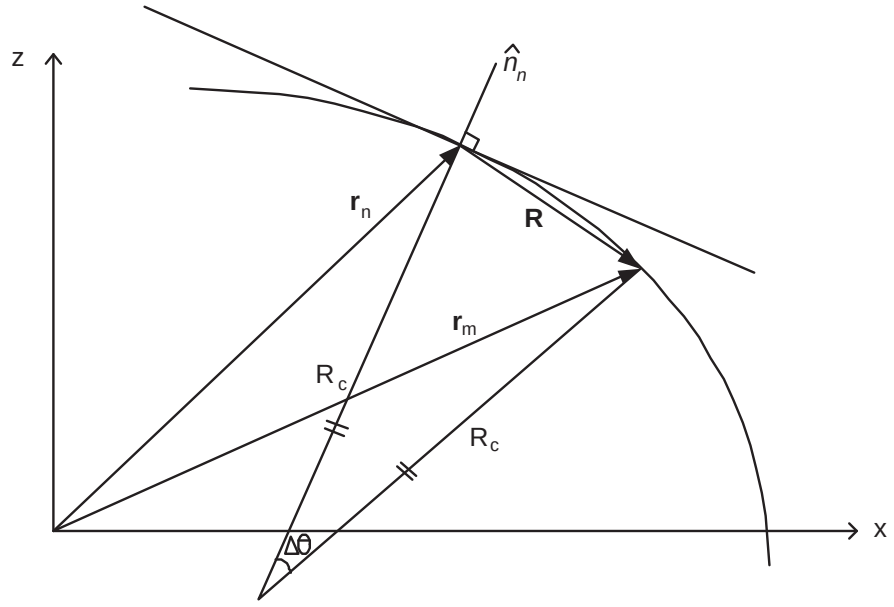

Figure A.1: Visualization of the problem for the case of $m = n$

Finally, by introducing all these modifications to (A.6)

$$S_{0mn} = \frac{1}{2} + \frac{\Delta x\sqrt{1 + (dz/dx)^2}}{4\pi R_c} \quad \text{where } m = n \quad \text{(A.10)}$$

with

$$R_c = -\frac{[1+(dz/dx)^2]^{3/2}}{(dz/dx)}. \tag{A.11}$$

If $m \neq n$, then

$$S_{0mn} = \int_{\Delta l_n} (\hat{n}' \cdot \nabla \phi_0) dl'. \tag{A.12}$$

By inserting the equations (A.4) and (A.5) into (A.12), we get

$$S_{0mn} = \frac{jk_0}{4}(\hat{n}_n \cdot \mathbf{R}) H_1^{(2)}(k_0|\mathbf{r}_m - \mathbf{r}_n|)\sqrt{1+(dz/dx)_n^2}\Delta x \quad \text{where } m \neq n. \tag{A.13}$$

- $$Z_{0mn} = j\omega\mu_0 \int_{\Delta l_n} \phi_0 dl'. \tag{A.14}$$

If $m = n$, by using (A.3)

$$Z_{0mn} = j\omega\mu_0 \int_{\Delta l_n} -\frac{j}{4} H_0^{(2)}(k_0|\mathbf{r}_m - \mathbf{r}_n|) dl'. \tag{A.15}$$

From [27] or [40]

$$\lim_{|\mathbf{r}_m - \mathbf{r}_n| \to 0} H_0^{(2)}(k_{0,1}|\mathbf{r}_m - \mathbf{r}_n|) \approx 1 - \left[\frac{2j}{\pi}\ln\left(\frac{\gamma k_{0,1}|\mathbf{r}_m - \mathbf{r}_n|}{2}\right)\right] \tag{A.16}$$

where $\gamma = \exp(0.5772...)$,i.e., the exponential of Euler's constant, we get

$$Z_{0mn} = j\omega\mu_0 \int_{\Delta l_n} -\frac{j}{4}\left[1 - \frac{2j}{\pi}\ln\left(\frac{\gamma k_0|\mathbf{r}_m - \mathbf{r}_n|}{2}\right)\right] dl' \tag{A.17}$$

and by considering Figure A.1 again,

$$|\mathbf{r}_m - \mathbf{r}_n| \approx \frac{\Delta x}{2}\sqrt{[1+(dz/dx)^2]} \tag{A.18}$$

together with the following simplification

$$\int \ln x' dx' = x'\ln x' - x' \tag{A.19}$$

$$\int \ln\left(\frac{kx'}{2}\right) dx' = x'\ln\left(\frac{kx'}{2}\right) - x' = x'\left[\ln\left(\frac{kx'}{2e}\right)\right], \tag{A.20}$$

equation (A.17) turns out to be

$$Z_{0mn} = j\omega\mu_0\Bigg[-\frac{j}{4}\Bigg(1-\frac{2j}{\pi}\ln\frac{\gamma k_0\sqrt{1+(dz/dx)_n^2}\Delta x}{4e}\Bigg) \sqrt{1+(dz/dx)_n^2}\Delta x\Bigg] \quad \text{where } m=n. \tag{A.21}$$

If $m \neq n$, by inserting (A.5) and (A.3) into (A.14), we simply get

$$Z_{0mn} = j\omega\mu_0\Bigg[-\frac{j}{4}H_0^{(2)}(k_0|\mathbf{r}_m-\mathbf{r}_n|)\sqrt{1+(dz/dx)_n^2}\Delta x\Bigg] \quad \text{where } m\neq n. \tag{A.22}$$

- $$S_{1mn} = \frac{1}{2}\delta_{mn} - \int_{\Delta l_n}(\hat{n}'\cdot\nabla\phi_1)dl'. \tag{A.23}$$

If $m = n$,

$$S_{1mn} = \frac{1}{2} - \int_{\Delta l_n}(\hat{n}'\cdot\nabla\phi_1)dl'. \tag{A.24}$$

Using (A.3) and (A.5), (A.24) is written as

$$S_{1mn} = \frac{1}{2} - (\hat{n}_n\cdot\mathbf{R})\frac{jk_1}{4}H_1^{(2)}(k_1|\mathbf{r}_n-\mathbf{r}_m|)\Delta x\sqrt{1+(dz/dx)^2}. \tag{A.25}$$

Since we are considering the second region now, the unit vector for this region will be opposite of the previous case, i.e., $\hat{n}'_n = -\hat{n}_n$, so

$$(\hat{n}_n\cdot\mathbf{R}) = \hat{n}'_n\cdot\frac{(\mathbf{r}_m-\mathbf{r}_n)}{|\mathbf{r}_m-\mathbf{r}_n|} = \approx \frac{\Delta\theta}{2}. \tag{A.26}$$

Introducing (A.7), (A.8) and (A.26) into (A.25), we finally get

$$S_{1mn} = \frac{1}{2} - \frac{\Delta x\sqrt{1+(dz/dx)^2}}{4\pi R_c} \quad \text{where } m=n \tag{A.27}$$

with

$$R_c = -\frac{[1+(dz/dx)^2]^{3/2}}{(dz/dx)}. \tag{A.28}$$

If $m \neq n$,

$$S_{1mn} = \int_{\Delta l_n}(\hat{n}'\cdot\nabla\phi_1)dl'. \tag{A.29}$$

By inserting the equations (A.4) and (A.5) into (A.29), we get

$$S_{1mn} = -\frac{jk_1}{4}(\hat{n}_n \cdot \mathbf{R})H_1^{(2)}(k_1|\mathbf{r}_m - \mathbf{r}_n|)\sqrt{1+(dz/dx)_n^2}\Delta x \quad \text{where } m \neq n. \tag{A.30}$$

- $$Z_{1mn} = -j\omega\mu_0 \int_{\Delta l_n} \phi_1 dl'. \tag{A.31}$$

If $m = n$, using (A.3), (A.31) is written as

$$Z_{1mn} = j\omega\mu_0 \int_{\Delta l_n} -\frac{j}{4}H_0^{(2)}(k_1|\mathbf{r}_m - \mathbf{r}_n|)dl'. \tag{A.32}$$

Then by inserting (A.16) into (A.32), we get

$$Z_{1mn} = -j\omega\mu_0 \int_{\Delta l_n} -\frac{j}{4}\left[1 - \frac{2j}{\pi}\ln\left(\frac{\gamma k_1|\mathbf{r}_m - \mathbf{r}_n|}{2}\right)\right]dl'. \tag{A.33}$$

Finally substituting (A.18)into (A.33) and doing the simplification given in (A.20), we get

$$Z_{0mn} = -j\omega\mu_0\left[-\frac{j}{4}\left(1 - \frac{2j}{\pi}\ln\frac{\gamma k_1\sqrt{1+(dz/dx)_n^2}\Delta x}{4e}\right)\sqrt{1+(dz/dx)_n^2}\Delta x\right] \quad \text{where } m = n. \tag{A.34}$$

If $m \neq n$, by inserting (A.5) and (A.3) into (A.31), we simply get

$$Z_{1mn} = j\omega\mu_0\left[\frac{j}{4}H_0^{(2)}(k_1|\mathbf{r}_m - \mathbf{r}_n|)\sqrt{1+(dz/dx)_n^2}\Delta x\right] \quad \text{where } m \neq n. \tag{A.35}$$

A.2 VV Polarization

For the VV polarization case, derivations of the matrix elements are very similar. All of the equations for HH polarization case, in view of the duality theorem, should be modified in a sense that electric fields and current densities must be replaced by magnetic ones; in addition μ_0 must be replaced by ϵ_0 through Z_{0mn} calculation and μ_0 must be replaced by ϵ_1 through Z_{1mn} calculation.

Bibliography

[1] P. Beckmann and A. Spizzichino, *The Scattering of Electromagnetic Waves From Rough Surfaces*, Norwood, Artech House, MA 1987.

[2] A. K. Fung, *Microwave Scattering and Emission. Models and Their Applications*, Norwood, Artech House, MA 1994.

[3] R. M. Axline and A. K. Fung, "Numerical Computation of scattering from a perfectly conducting random surface," *IEEE Trans. Antennas Propagat.*, vol. AP-26, pp. 482-488, May 1978.

[4] A. K. Fung and M. F. Chen, "Numerical simulation of scattering from simple and composite random surfaces," *J. Opt. Soc. Am.*, vol. 2, pp. 2274-2284, 1985.

[5] M. F. Chen and S. Y. Bai, "Computer simulation of wave scattering from a dielectric random surface in two dimensions-cylindrical case," *J. Electron. Waves Appl.*, vol. 4, no. 10, pp. 963-982, 1990.

[6] D. Holliday, L. L. DeRaad, and G. C. St-Cyr, "Forward-backward: A new method for computing low-grazing angle scattering," *IEEE Trans. Antennas Propagat.*, vol.44, pp. 722-729, May 1996.

[7] D. A. Kapp and G. S. Brown, "A new numerical method for rough surface scattering calculations," *IEEE Trans. Antennas Propagat.*, vol.44, pp. 711-721, May 1996.

[8] P. Tran, "Calculation of the scattering electromagnetic waves from a two-dimesional perfectly conducting surface using the method of ordered multiple interactions,"" *Waves Random Media*, vol. 7, no.3, pp. 295-302, Jul. 1997.

[9] C. F. Smith, A. F. Peterson and R. Mittra,"The biconjugate gradient method for electromagnetic scattering," *IEEE Trans. Antennas Propagat.*, vol.38, pp. 938-940, Jun. 1990.

[10] D. J. Donohue, H. C. Ku and D. R. Thompson, "Application of iterative moment-method solutions to ocean surface radar scattering",*IEEE Trans. Antennas Propagat.*, vol.46, pp. 121-132, Jan. 1998.

[11] F. Chen, "The numerical calculation of two-dimensional rough surface scattering by the conjugate gradient method", *Int. J. Remote Sensing*, vol. 17, no. 4, pp. 801-808, 1996.

[12] J. C. West and J. M. Sturm, "On iterative approaches for electromagnetic rough-surface scattering problems," *IEEE Trans. Antennas Propagat.*, vol.47, pp. 1281-1288, Aug. 1999.

[13] M. R. Pino, L. Landesa, J. L. Rodrigues, F. Obellerio and R. J. Burkholder, "The generalized forward-backward method for analyzing the scattering targets on ocean-like surfaces," *IEEE Trans. Antennas Propagat.*, vol.47, pp. 961-969, Aug. 1999.

[14] H. T. Chou and J. T. Johnson, "A novel acceleration algorithm for the computation of scattering from rough surfaces with the forward-backward method," *Radio Sci.*, vol.33, pp. 1277-1287, Sept./Oct. 1998.

[15] D. Torrungrueng and J. T. Johnson, "Numerical studies of back-scattering enhancement of electromagnetic waves from two-dimensional random rough surfaces using the FB/NSA method", *J. Opt. Soc. Am. A Opt. Image Sci.*, vol. 18, pp. 2518-2526, 2001

[16] A. Benali, J. Chandezon and J. Fontaine, "A new theory for scattering of electromagnetic waves from conducting or dielectric rough surfaces",*IEEE Trans. Antennas Propagat.*, vol.40, pp. 141-148, Feb. 1992.

[17] K. Sarabandi, Y. Oh, F. T. Ulaby, "A numerical simulation of scattering from one-dimesional inhomogeneous dielectric random surfaces," *IEEE Trans. Geosci. Remote Sensing*, vol.34, pp. 425-432, Mar. 1996.

[18] Q. Li, C. H. Chan, L. Tsang, "Monte Carlo simulations of wave scattering from lossy dielectric random rough surfaces using the physics-based two-grid method and the canonical-grid method," *IEEE Trans. Antennas Propagat.*, vol.47, pp. 752-763, Apr. 1999.

[19] J. C. West, "Integral equation formulation for iterative calculation of scattering from lossy rough surfaces," *IEEE Trans. Geosci. Remote Sensing*, vol.38, pp. 1609-1615, Jul. 2000.

[20] "Special issue on low-grazing-angle backscattering from rough surfaces", *IEEE Trans. Antennas and Propagat.*, vol. 46, Jan. 1998.

[21] A. K. Fung, Z. Li and K. S. Chen, "Backscattering from a randomly rough dielectric surface",*IEEE Trans. Geosci. Remote Sensing*, vol.30, pp.356-369, Mar. 1992.

[22] D. Holliday, L. L. DeRaad, and G. C. St-Cyr, "Forward-backward method for scattering from imperfect conductors," *IEEE Trans. Antennas Propagat.*, vol.46, pp. 101-107, Jan. 1998.

[23] G. Franceschetti, A. Iodice, and D. Riccio, "Scattering from dielectric random fractal surfaces via method of moments," *IEEE Trans. Geosci. Remote Sensing*, vol.38, pp. 1644-1655, Sept. 2000.

[24] A. Iodice, "Forward-backward method for scattering from dielectric rough surfaces," *IEEE Trans. Antennas Propagat.*, vol.50, pp. 901-911, Jul. 2002.

[25] A. Iodice, "Scattering from natural soils modeled by dielectric fractal profiles: The forward-backward approach",*IEEE Trans. Geosci. Remote Sensing*, vol.42, pp.77-85, Jan. 2004.

[26] X. Wang, Y. Gan, L. Li, "Electromagnetic scattering by partially buried PEC cylinder at the dielectric rough surface interface: TM case", *IEEE Antennas and Wireless Propagat. Letters*, vol.2, 2003.

[27] C. A. Balanis, *Advanced Engineering Electromagnetics*, John Wiley & Sons, 1989.

[28] R. F. Harrington, *Field Computation by Moment Method*, New York: IEEE Press, 1993.

[29] L. Tsang, J. A. Kong, K. H. Ding and C. O. Ao, *Scattering of Electromagnetic Waves - Numerical Simulations*, John Wiley & Sons, 2001.

[30] L. Tsang, J. A. Kong, andK-.H. Ding, *Scattering of Electromagnetic Waves: Theories and Applications*, Wiley-Interscience, New York, 2000.

[31] J. A. Kong, *Electromagnetic Wave Theory*, MW Publishing, Cambridge, MA, 2000.

[32] A. Papoulis,*Probability, Random Variables, and Stochastic Processes*, Mc-Gram Hill, New York, 1984.

[33] R. Bancroft, *Understanding Electromagnetic Scattering Using the Moment Method*, Artech House, Norwood, MA, 1996.

[34] M.F. Chen and A. K. Fung, "A numerical study of the regions of validity of the Kirchoff and small perturbation rough surface scattering models," *Radio Science*, vol. 23, no. 2, pp. 163-170, 1988.

[35] R. Mittra and A. Peterson, *Numerical techniques for RCS computation and scattering center approach to RCS modeling*, Lecture Note, vol. 2

[36] R. Barrett, M. Berry, T. F. Chan, J. Demmel, J. M. Donato, J. Dongarra, V. Eijkhout, R. Pozo, C. Romine, H. Vorst,"Templates for the Solution of Linear Sytems: Building Blocks for Iterative Methods" *Philadelphia: Siam (Society for Industrial and Applied Mathematics)*, 1994

[37] C.A.Tunç, "Application of spectral acceleration forward-backward method for propagation over terrain",*M.S. Thesis in Electrical and Electronics Engineering*, Bilkent University, Sept. 2003.

[38] B. Babaoğlu, "Application of biconjugate gradient stabilized method with spectral acceleration for propagation over terrain profiles",*M.S. Thesis in Electrical and Electronics Engineering*, Bilkent University, Oct. 2003.

[39] R. Freund and N. Nachtigal, "An implementation of the QMR method based on coupled two term recurrences", SIAM J. Sci. Statist. Comput., vol.15, pp.313-337, 1994.

[40] M. Abramowitz and I. A. Stegun, Eds., *Handbook of Mathematical Functions with Formulas, Graphs, and Mathematical Tables*, Dover Publications, New York, 1972.

[41] J. T. Johnson, R. T. Shin, J. A. Kong, L. Tsang, and K. Pak, "A numerical study of the composite surface model for ocean backscattering", *IEEE Trans. Geosci. Remote Sensing*, vol. 36, pp. 7283, Jan. 1998.

[42] J. W. Crispin and K. M. Siegel, *Methods of Radar Cross-Section Analysis*, Academic Press, New York and London, 1968.